

Summer 2017

Full simulation for the Qweak experiment at 1.16 and 0.877 GeV and their impact on extracting the PV asymmetry in the $N \rightarrow \Delta$ a transition

Hend Abdullah Nuhait
Louisiana Tech University

Follow this and additional works at: <https://digitalcommons.latech.edu/dissertations>



Part of the [Computer Sciences Commons](#), and the [Other Engineering Commons](#)

Recommended Citation

Nuhait, Hend Abdullah, "" (2017). *Dissertation*. 56.
<https://digitalcommons.latech.edu/dissertations/56>

This Dissertation is brought to you for free and open access by the Graduate School at Louisiana Tech Digital Commons. It has been accepted for inclusion in Doctoral Dissertations by an authorized administrator of Louisiana Tech Digital Commons. For more information, please contact digitalcommons@latech.edu.

FULL SIMULATION FOR THE QWEAK EXPERIMENT AT 1.16 AND 0.877
GeV AND THEIR IMPACT ON EXTRACTING THE PV ASYMMETRY IN THE
 $N \rightarrow \Delta$ TRANSITION

by

Hend Abdullah Nuhait, B.S., M.S.

A Dissertation Presented in Partial Fulfillment
of the Requirements for the Degree
Doctor of Philosophy

COLLEGE OF ENGINEERING AND SCIENCE
LOUISIANA TECH UNIVERSITY

August 2017

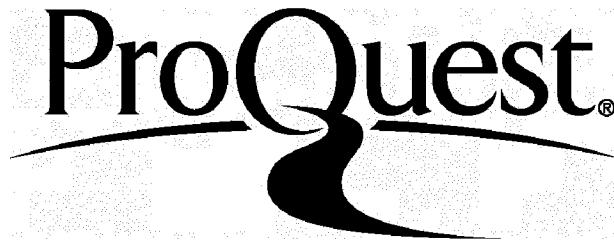
ProQuest Number: 10753663

All rights reserved

INFORMATION TO ALL USERS

The quality of this reproduction is dependent upon the quality of the copy submitted.

In the unlikely event that the author did not send a complete manuscript and there are missing pages, these will be noted. Also, if material had to be removed, a note will indicate the deletion.



ProQuest 10753663

Published by ProQuest LLC(2018). Copyright of the Dissertation is held by the Author.

All rights reserved.

This work is protected against unauthorized copying under Title 17, United States Code.
Microform Edition © ProQuest LLC.

ProQuest LLC
789 East Eisenhower Parkway
P.O. Box 1346
Ann Arbor, MI 48106-1346

LOUISIANA TECH UNIVERSITY

THE GRADUATE SCHOOL

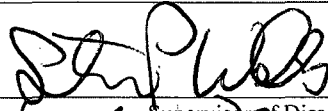
June 26 2017

Date

We hereby recommend that the dissertation prepared under our supervision
by Hend Abdullah Nuhait

entitled Full Simulation for the Qweak Experiment at 1.16 and 0.877 GeV and their
Impact on Extracting the PV Asymmetry in the N to Delta Transition.

be accepted in partial fulfillment of the requirements for the Degree of
Doctorate of Philosophy - Computational Analysis and Modeling


Wahyuni Dhi

Supervisor of Dissertation Research

Head of Department

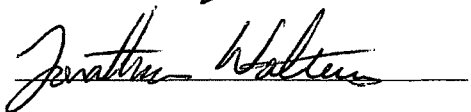
Computational Analysis and Modeling

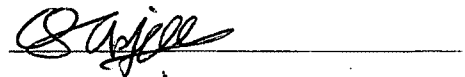
Department

Recommendation concurred in:



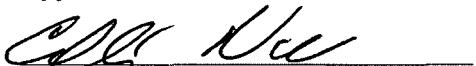






Advisory Committee

Approved:


Director of Graduate Studies

Approved:


Dean of the Graduate School


Dean of the College

ABSTRACT

The Qweak project is seeking to find new physics beyond the Standard Model. It is aimed to measure the weak charge of the proton, which has never been measured, at 4% precision at low momentum transfer. The experiment is performed by scattering electrons from protons and exploiting parity violation in the weak interaction at low four-momentum transfer.

In this experiment, two measurements were considered: which are elastic and inelastic. The elastic is to measure the proton's weak charge. In addition, the inelastic asymmetry measurement, which will extract the low energy constant d_Δ . That measurement works in the neutral current sector of the weak interaction.

Qweak measures the asymmetry in the $N \rightarrow \Delta$ transition. Because the elastic radiative tail gives a dominant contribution to the uncertainty to the $N \rightarrow \Delta$ asymmetries, this thesis will discuss the radiative correction. In addition, this thesis will describe in details the extensive simulations performed to determine the impact of all simulated background processes on extracting the PV $N \rightarrow \Delta$ asymmetries. In the process of verifying the validity of these background fractions, we determined the best value of a quantity measured during the Qweak experiment: the beam normal single spin asymmetry, B_n , in the $N \rightarrow \Delta$ transition.

APPROVAL FOR SCHOLARLY DISSEMINATION

The author grants to the Prescott Memorial Library of Louisiana Tech University the right to reproduce, by appropriate methods, upon request, any or all portions of this Dissertation. It is understood that "proper request" consists of the agreement, on the part of the requesting party, that said reproduction is for his personal use and that subsequent reproduction will not occur without written approval of the author of this Dissertation. Further, any portions of the Dissertation used in books, papers, and other works must be appropriately referenced to this Dissertation.

Finally, the author of this Dissertation reserves the right to publish freely, in the literature, at any time, any or all portions of this Dissertation.

Author Mend Nuhan

Date July 26 2017

TABLE OF CONTENTS

ABSTRACT	iii
LIST OF TABLES.....	vii
LIST OF FIGURES.....	viii
ACKNOWLEDGEMENT.....	xiv
CHAPTER 1 INTRODUCTION.....	1
1.1 Motivation.....	1
1.2 Introduction of the Qweak Experiment	2
CHAPTER 2 RADIATIVE CORRECTION	6
2.1 Radiative Tails Calculation.....	6
2.2 Peaking Approximation	10
2.3 Straggling Effect	12
2.4 Perturbation Theory	15
2.4.1 Radiative Correction to the Elastic Peak	15
2.5 Elastic Radiative Tail.....	21
2.6 Radiative Correction to Continous Spectra	22
2.7 Conclusion.....	25
CHAPTER 3 SIMULATION.....	27
3.1 Simulation Parameters.....	28

3.1.1	Incident Beam Energy, Spectrometer Current, and Electron Prime Window	28
3.1.2	Angles	32
3.1.3	Four Momentum Q^2	34
3.1.4	Invariant Mass of the Experiment W	36
3.1.5	Main Detectors	38
3.2	Random Number	39
3.3	Photoelectrons	39
3.4	Reaction Types	40
3.4.1	Electron Proton Radiative Scattering.....	40
3.5	Electron Proton Elastic Scattering	41
3.5.1	Schwinger Correction Included	41
3.5.2	Δ Resonance Generator.....	43
3.5.3	Electron Aluminum Generator	43
3.5.4	Pions.....	44
3.6	Rate	44
3.7	Yield.....	45
3.8	One Detector Simulation.....	48
3.8.1	1.16 GeV.....	48
3.8.2	0.877 GeV.....	72
3.9	All Detector Simulation for 1.16 GeV	77
3.10	All Octant Simulation for 0.877 GeV.....	85
3.10.1	Inelastic Fraction.....	89

3.11 Bn Model	97
3.12 Summary	101
CHAPTER 4 IMPACT OF SIMULATION ON EXTRACTION OF $N \rightarrow \Delta$ ASYMMETRIES	106
CHAPTER 5 SUMMARY	108
APPENDIX	110
BIBLIOGRAPHY	122

LIST OF TABLES

Table 3.1	Dilution factor around delta peak for Geant3 and Geant4	53
Table 3.2	Aluminum, elastic, and pion fractions for elastic and Δ peaks.	72
Table 3.3	Aluminum, elastic, and pion fractions at $Q_{\text{tor}} = 4650$ A.	77
Table 4.1	Aluminum, Elastic, and Pion fractions at $Q_{\text{tor}} = 6700$ A.	107
Table 4.2	Aluminum, Elastic, and Pion fractions at $Q_{\text{tor}} = 4650$ A.	107

LIST OF FIGURES

Figure 1.1	A sketch of the accelerator in Jefferson Lab.	3
Figure 1.2	A sketch of the Qweak apparatus.	4
Figure 1.3	The Qweak equipment during installation.	4
Figure 2.1	Integrand of Equation 2.12 to show peaking	11
Figure 2.2	Feynman diagram for electron-proton elastic scattering	16
Figure 2.3	Feynman diagram of the δ Vertex	17
Figure 2.4	Feynman diagram of the δ Vacuum	17
Figure 2.5	Radiative tails examples	26
Figure 3.1	QTor magnet spectrometer.	28
Figure 3.2	Electron prime window for QTor = 3000 A.	29
Figure 3.3	Electron prime window for QTor = 6700 A.	30
Figure 3.4	Electron prime window for QTor = 9000 A.	30
Figure 3.5	Open electron prime window for QTor = 3000 A.	31
Figure 3.6	Open electron prime window for QTor = 6700 A.	31
Figure 3.7	Open electron prime window for QTor = 9000 A.	32
Figure 3.8	Theta angle for electron proton scattering.	33
Figure 3.9	Four momentum energy Q^2	35
Figure 3.10	Invariant mass of the experiment W	37
Figure 3.11	Sketch of the eight detectors.	38
Figure 3.12	The eight detectors as part of the experiment	39
Figure 3.13	Variation of rate (in kHz/uA) as a function of QTor current (A) from generator 7 simulations, compared with data.	41

Figure 3.14 Generator 1 rate (in kHz/uA) with and without the Schwinger Correction compared to the data.	42
Figure 3.15 Testing the cut of the photoelectrons from greater than 0 to greater than 4 on rate (in kHz/uA), the simulation is lower than the data because there was a normalization problem between the data and simulation in the early part of this study. The normalization was corrected later in the study.	45
Figure 3.16 Physical experiment yield is normalized by 1 million in attempt to match the data since the physical data yield is in arbitrary units, however it didn't match it. Later both the experiment and simulation data were normalized at one point to match each other.	46
Figure 3.17 The simulation yield is weighted by left and right PEs > 0.	47
Figure 3.18 The simulation yield is weighted by total PEs > 0.	48
Figure 3.19 Elastic (the blue "lower" part) vs inelastic (the red "upper" part) events in the detector.	49
Figure 3.20 Variation of rate (in kHz/uA) as a function of QTor current (A) from generator 1 and generator 7 simulations, compared with data.	49
Figure 3.21 Variation of rate (in kHz/uA) as a function of QTor current (A) from event 1 Rate vs event 7 elastic peak simulations, compared with data.	50
Figure 3.22 Variation of rate (in kHz/uA) as a function of QTor current (A) from generator 1 without Schwinger correction, generator 5, and generator 7 total simulations, compared with data.	51
Figure 3.23 Variation of yield as a function of QTor current (A) from event 1 Rate vs event 7 yield simulations, compared with data.	51
Figure 3.24 Event generator 7 yield relative residual.	54
Figure 3.25 Event generator 7 rate relative residual.	55
Figure 3.26 Event generators 1 and 5 yield relative residual.	55
Figure 3.27 Event generators 1 and 5 rate relative residual.	56

Figure 3.28 Variation of rate (in kHz/uA) as a function of QTor current (A) from generator 1 with and without the Schwinger correction using the Mo and Tsai formalism simulations, compared with data.	57
Figure 3.29 Variation of rate (in kHz/uA) as a function of QTor current (A) from generator 1 with and without the Schwinger correction using the Lightbody and O'Connel formalism simulations, compared with data. . .	58
Figure 3.30 The correlation between vertex energy and theta with cut on left and right PEs >0.	59
Figure 3.31 The correlation between local vertex energy and global theta with cut on left and right PEs >0 and elastic energy < 15 MeV.	59
Figure 3.32 Variation of rate (in kHz/uA) as a function of QTor current (A) from generator 1 rate with the cut on elastic energy<15 MeV, generator 7 EL and DIS simulations, compared with data.	60
Figure 3.33 Variation of yield as a function of QTor current (A) from generator 1 rate with the cut on elastic energy<15 MeV, generator 7 EL and DIS simulations, compared with data.	61
Figure 3.34 Rate relative residual.	61
Figure 3.35 Yield relative residual.	62
Figure 3.36 Variation of rate (in kHz/uA) as a function of QTor current (A) from generator 1 rate with the cut on elastic energy<15 MeV, generator 2, generator 7 EL and DIS simulations, compared with data.	63
Figure 3.37 Variation of rate (in kHz/uA) as a function of QTor current (A) from generator 1 rate with the cut on elastic energy<15 MeV, generator 2, generator 7 EL and DIS simulations, compared with data. The low QTor discrepancy is due to the Möller scattered electrons. This study didn't include a Möller generator.	64

Figure 3.38 Variation of yield as a function of QTor current (A) from generator 1 rate with the cut on elastic energy < 15 MeV, generator 2, generator 7 EL and DIS simulations, compared with data.	65
Figure 3.39 Rate relative residual.	66
Figure 3.40 Yield relative residual.	66
Figure 3.41 Rate (in kHz/uA) at 8921 A in data and simulation.	67
Figure 3.42 Yield dilution factor around the Δ peak.	68
Figure 3.43 Variation of rate (in kHz/uA) as a function of QTor current (A) from simulations, compared with data	69
Figure 3.44 Variation of yield as a function of QTor current (A) from simulations, compared with data in log scale.	70
Figure 3.45 Rate relative residual.	71
Figure 3.46 Yield relative residual.	71
Figure 3.47 Variation of rate (in kHz/uA) as a function of QTor current (A) from simulations, compared with data.	73
Figure 3.48 Variation of rate (in kHz/uA) as a function of QTor current (A) from simulations, compared with data in log scale.	74
Figure 3.49 Variation of yield as a function of QTor current (A) from simulations, compared with data.	75
Figure 3.50 Variation of yield as a function of QTor current (A) from simulations, compared with data on a log scale.	76
Figure 3.51 Yield dilution factor near the Δ peak.	77
Figure 3.52 Variation of rate (in kHz/uA) as a function of QTor current (A) from all octants simulations, compared with data.	78
Figure 3.53 Difference between octants rate (in kHz/uA) at QTor = 6700 A.	79
Figure 3.54 Difference between octants rate (in kHz/uA) at QTor = 8921 A.	80
Figure 3.55 Rate relative residual.	80
Figure 3.56 Rate simulation for all octants using event 5.	81

Figure 3.57 Rate relative residual when using event 5.	82
Figure 3.58 Variation of yield as a function of QTor current (A) from all octants simulations, compared with data.	83
Figure 3.59 Yield average for all octants.	84
Figure 3.60 Yield relative residual.	84
Figure 3.61 Variation of rate (in kHz/uA) as a function of QTor current (A) from all octants simulations, compared with data.	85
Figure 3.62 0.877 comparison between rates (in kHz/uA) in different octants.	86
Figure 3.63 Variation of yield (in kHz/uA) as a function of QTor current (A) from all octants simulations.	87
Figure 3.64 Variation of yield as a function of QTor current (A) from all octants simulations, compared with data.	88
Figure 3.65 All octant 0.877 GeV yield relative residual, octant 1 and octant 5 have odd shape because the physical experimental data don't include these two octants.	88
Figure 3.66 One octant rate and yield inelastic fraction for 1.16 GeV.	90
Figure 3.67 All octants rate and yield inelastic fraction for 1.16 GeV.	90
Figure 3.68 All octants rate and yield inelastic fraction for 0.877 GeV.	91
Figure 3.69 Event 1 vertex energy vs number of PEs for octant 7 with cut on PEs > 0 at Qtor 6700.	92
Figure 3.70 Event 7 vertex energy vs number of PEs for octant 7 with cut on PEs > 0 at Qtor 6700.	92
Figure 3.71 Event 1 PE's for Qtor = 6700 A, with PEs > 0	93
Figure 3.72 Event 7 PE's for Qtor = 6700 A, with PEs > 0.	93
Figure 3.73 Rate and yield inelastic fraction with photoelectron cut.	94
Figure 3.74 Yield elastic fraction at Δ peak.	95
Figure 3.75 Aluminum elastic fraction at Δ peak.	96
Figure 3.76 Pion elastic fraction at Δ peak.	96

Figure 3.77 The inelastic fraction in B_n model.	99
Figure 3.78 $\chi^2/d.o.f.$ vs. B_n around the B_n value which minimized χ^2	99
Figure 3.79 The inelastic fraction in B_n model for all Qtor.	100
Figure 3.80 1.16 GeV all actant rate.	102
Figure 3.81 0.877 GeV all octant rate.	103
Figure 3.82 1.16 GeV all octant yield.	104
Figure 3.83 0.877 GeV all octant yield.	105

ACKNOWLEDGEMENT

First and foremost, I thank God for giving me the strength and providing me with opportunities to complete this thesis.

I would like to express my sincere gratitude toward my advisor, Dr. Steven P Wells, for his guidance throughout my research, and his patience even when my brain shut down. He never lost his patience with me even when I committed vital mistakes. He understood my lifestyle as a mother and was flexible with my schedule. He is always reachable to answer any question and to help with any problem.

I am grateful to my parents, Abdullah Nuhait and Hessah Almedlej, who have been supporting me in every possible way throughout my journey. They are my role models. I learned from them how to be independent, hard working and ambitious.

I would like to thank my husband, Hamad Aldawi, for his unfailing support and continuous encouragement throughout my graduate life. I am thankful to my siblings: Norah, Mohammad, Moath, Anas, Arwa, and Maha for always being there for me when I needed them, for including me in all family celebrations even when I'm thousands of miles away, for showering me with gifts all the time, and for spoiling my kids and buying them stuff that I couldn't afford. I would like to acknowledge my kids, Abdulaziz and Monirah, for their patience when I'm busy, for forgiving me when I forget to spend time with them. I also would like to thank my family in-law for believing in me and supporting me.

I would like to thank all Qweak collaborators, without them I would not be able to complete this research. Special thanks to Dr. Wouter Deconinck, Jim Dowd, and Kurtis Bartlett for providing me the material and walking me through the simulation

package step by step. Dr. Mark Pitt, Dr. David Armstrong, and Dr. Mark Dalton for their helpful feedback and suggestions.

I would like to thank my committee, Dr. Ben Choi, Dr. Neven Simicevic, Dr. Rakitha Beminiwattha, and Dr. Jonathan Walters for their hard questions that expanded my thinking. Also, I would like to thank Dr. Weizhong Dai for doing every possible thing to enhance my Ph.D. experience. I would like to thank Mr. Daniel Erickson for his wise comforting words during my breaking down moments.

A very special gratitude goes out to my cousin and best friend, Nada, for being there for me through my tough times, for knowing exactly what I needed to hear, and for the zillions of conversations that never fail to cheer me up.

Lastly, I would like to thank all my family members, my friends back in Saudi Arabia, and my Ruston friends for keeping me encouraged, and filling my life with joy.

Chapter 1

INTRODUCTION

For all of recorded human history, scientists have been discovering and establishing new physics theories and phenomena. With the prediction of the quark structure of hadrons, the Standard Model of particles and interactions was formed. The Standard Model was developed in 1970. It explains the relationship between the particles and three of the main forces. The four fundamental forces are the strong force, the weak force, the electromagnetic force, and the gravitational force. The gravitational force is the weakest among the forces, and the Standard Model doesn't include it.

The strong force is the strongest force among them, while the weak force is only stronger than the gravitational force. The weak force and electromagnetic force are very similar, however the electromagnetic force conserves parity while the weak force violates parity. "Parity is a transformation of spatial coordinates such that all coordinates are reversed" [5]. These forces are mediated by the interaction of their force carrier particles. The force carrier particles are called bosons. The strong force is mediated by the interaction of gluons, the boson for the electromagnetic force is the photon, and, the weak force's bosons are Z and W^\pm bosons[9].

1.1 Motivation

Although the Standard Model is the best physics model so far, it is not complete. It doesn't answer all questions. The Standard Model continues to be tested experimentally. The prediction of The Standard Model for the weak charge of the proton is

$$Q_p^W = 1 - 4\sin^2\theta_W \quad (1.1)$$

where θ_W is the weak mixing angle which relates the electromagnetic and weak interactions. The value of $\sin^2\theta_W$ is approximately 1/4 making θ_p^W a small quantity and therefore difficult to measure. While this is the Standard Model prediction, it has never been measured.

1.2 Introduction of the Qweak Experiment

The Qweak project is seeking to find new physics beyond the Standard Model. It is aimed to measure the weak charge of the proton, which has never been measured, at 4% precision at low momentum transfer.

The experiment was performed at Jefferson Laboratory in Newport News, Virginia. Many universities, professors, and students are involved. To make the experiment happen, an accelerator was built under the ground of Jefferson Lab. The accelerator's job is to make the electron beam at a given energy. Figure 1.1 shows a sketch of the accelerator. The final electron beam is steered into three halls. These halls are divided such that each of them receives a portion of the electron beam with a unique energy. Moreover, each hall has its own staff and researchers, who are focusing on special criteria. The Qweak experiment was located in hall C. The physical experiment was scheduled for 2200 hours.

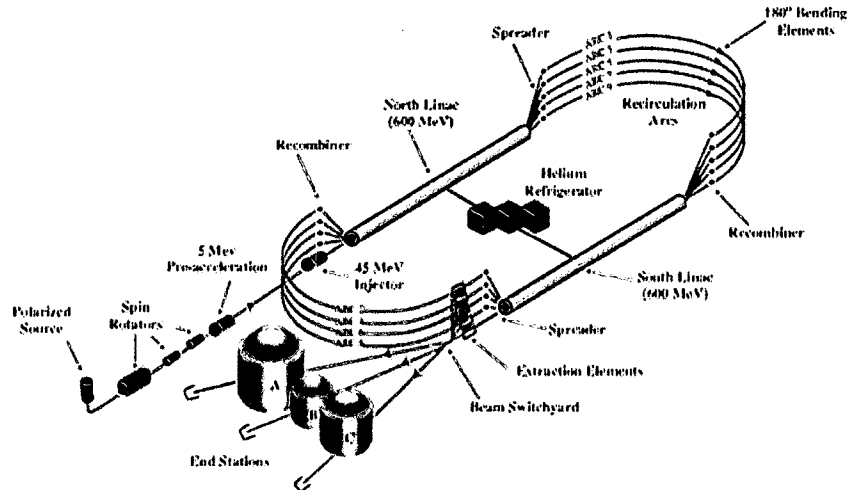


Figure 1.1: A sketch of the accelerator in Jefferson Lab.

The experiment was performed by scattering electrons from protons and exploiting parity violation in the weak interaction at low four-momentum transfer. Electron scattering is usually used in many physics experiments because electrons don't have internal structure, and all electron interactions with the other particles are well known.

In this experiment, two measurements were considered. The measurements are elastic and inelastic scattering. The elastic measurement is the primary measurement to measure the proton's weak charge. In addition, the inelastic asymmetry measurement is the secondary measurement, which will extract the low energy constant d_{Δ} . That measurement works in the neutral current sector of the weak interaction.

In the Qweak target, electrons are scattered from protons in a liquid hydrogen target. Moreover, there are eight main detectors in the Qweak apparatus positioned symmetrically around the beam. The scattered electron beam hits the eight detectors. The scattered electrons generate Čerenkov radiation in the detectors. The photomultiplier tubes (PMTs), which are attached to the detectors, collect the Čerenkov light and convert it into a current pulse, which is digitalized and read out by computer and analyzed. Figure 1.2 shows a sketch of the Qweak apparatus. Figure 1.3 shows the actual equipment during the installation phase.

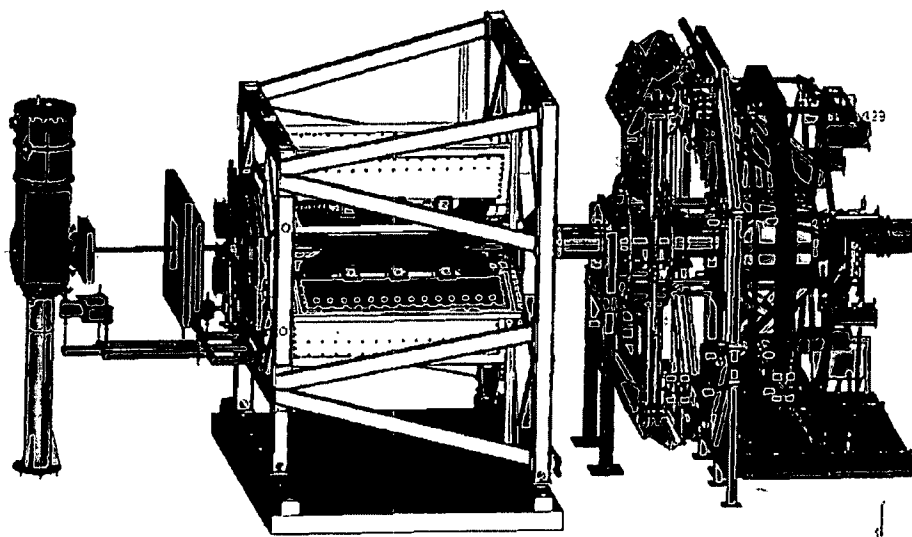


Figure 1.2: A sketch of the Qweak apparatus.

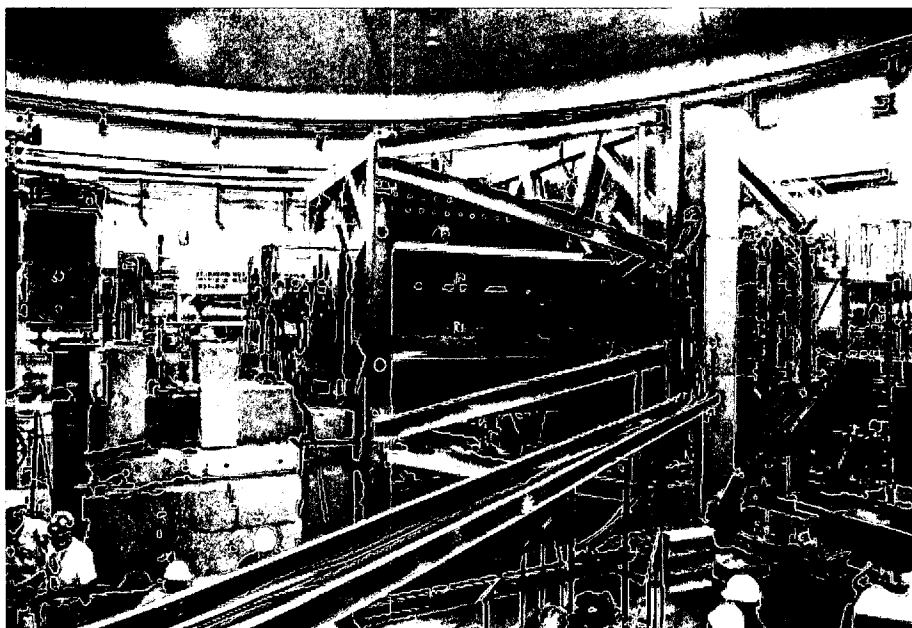


Figure 1.3: The Qweak equipment during installation.

Two measurements are extracted from the experiment. The important measurement is the weak charge of the proton. That is extracted from the elastic scattering between electrons and protons due to parity violation. Parity is that the transformation of the coordinates of space will be inverted. The other measurement is inelastic electron proton scattering. The purpose of it is to extract the low energy constant d_{Δ} . This

constant is part of the weak interaction between the quarks in the protons and the electrons. The quantity d_Δ is a low energy constant in the weak Lagrangian.

Q_{weak} measures the asymmetry in the $N \rightarrow \Delta$ transition. Because the elastic radiative tail gives a dominant contribution to the uncertainty to the $N \rightarrow \Delta$ asymmetries, this research will discuss the radiative correction, while the bulk of this work will describe in detail the extensive simulations performed to determine the impact of all simulated background processes on extracting the PV $N \rightarrow \Delta$ asymmetries.

Chapter 2

RADIATIVE CORRECTION

What are radiative corrections, and why are they important? Radiative corrections are an important part of physics in general. They are dominated by electrons radiating photons. They are calculated to acquire the nucleon form factors, among other observables. It is critical to apply those to electron-proton scattering. In addition, they acquire the contribution of the two-photon exchange diagrams. The radiative correction results in a change in the cross section for electron scattering from any nuclear target. In any experiment, especially in the electron-proton scattering, if the radiative correction is not calculated correctly, any extracted information may not be reliable.

2.1 Radiative Tails Calculation

Tsai [1] proved that the unpolarized target system radiated tail can be calculated correctly in the lowest order of α , where α is a fine structure constant that can be calculated via

$$\alpha = \frac{e^2}{4\pi\hbar c} \quad (2.1)$$

where e is the electron charge, c is the speed of light and \hbar is Planck's constant[2]. That is only if the system is assumed to have only a one photon exchange contribution, and if the electron and hadron bremsstrahlung's interference terms are neglected. Finally, it is a crucial correction if the system detects only scattered electrons. The

radiative tail is calculated because the one photon exchange model for non-radiative cross section relies on the same two factors as the radiative cross section. The non radiative cross section formula can be written as

$$\frac{d\sigma}{d\Omega dp} = \left(\frac{2\alpha^2 E_p^2 M}{q^4} \right) \cos^2 \frac{1}{2} \theta \left[F(q^2, M_{f^2}) \right] + \left(\frac{2}{M^2} \right) \tan^2 \frac{1}{2} \theta G(q^2, M_{f^2}) \quad (2.2)$$

$$q^2 = -4E_s E_p \sin^2 \left(\frac{\theta}{2} \right) \quad (2.3)$$

$$M_j^2 = M^2 + 2M(E_s - E_p) + q^2, \quad (2.4)$$

where E_s is the energy of the incident electrons, E_p is the energy of the scattered electrons, M is the mass of the initial hadronic system, M_f is the mass of final hadronic system, and θ is the scattering angle. The two factors have to be normalized by the non-radiative cross section

$$F(q^2, M_f^2) = F_i(q^2) \delta(M_f^2 - M_j^2) \quad (2.5)$$

$$G(q^2, M_f^2) = G_i(q^2) \delta(M_f^2 - M_j^2) \quad (2.6)$$

M_f^2 and M_i^2 are equal if the final hadronic system is discrete, and j correspond to the j th discrete level. For elastic scattering j is equal to 0. Applying the normalized form factors to the non-radiated cross section formula gives

$$\frac{d\sigma_j}{d\Omega} = \frac{\alpha^2 E_p^2 M}{q^4} [1 + E_s M^{-1} (1 - \cos\theta)]^{-1} \cos^2 \frac{1}{2} \theta \left[F_j(q^2) + \frac{2}{M^2} \tan^2 \frac{1}{2} \theta G_j(q^2) \right] \quad (2.7)$$

The discrete final hadronic state radiative tail is calculated via,

$$\frac{d^2\sigma_{jr}}{d\Omega dp} = \frac{\alpha^3 E_p}{(2\pi)^2 M E_s} \int_{-1}^1 \frac{\omega d(\cos\theta_k)}{2q^2(u_0 - |\mathbf{u}| \cos\theta_k)} \int_0^{2\pi} B_{\mu r} T_{\mu r} d\phi_k \quad (2.8)$$

where

$$\begin{aligned}
B_{\mu r} T_{\mu r} = & M 2F_j(q^2) \left\{ \frac{-m^2}{(pk)^2} \left[2E_s(E_p + \omega) + \frac{1}{2}q^2 \right] - \frac{-m^2}{(sk)^2} \left[2E_p(E_s + \omega) + \frac{1}{2}q^2 \right] - 2 \right. \\
& + \frac{2}{(sk)(pk)} \{ m^2(sp - \omega^2) + (ps)[2E_s E_p - (ps) + \omega(E_s - E_p)] \} \\
& + (pk)^{-1} [2(E_s E_p + E_s \omega + E_p^2) + \frac{1}{2}q^2 - (sp) - m^2] - (sk)^{-1} \\
& \left. [2(E_s E_p + E_p \omega + E_s^2) + \frac{1}{2}q^2 - (sp) - m^2] \right\} \\
& + G_j(q^2) \left(m^2(2m^2 q^2) \left\{ \left[\frac{1}{(pk)^2} \right] \left[\frac{1}{(sk)^2} \right] \right\} + 4 + \frac{4(ps)(ps - 2m^2)}{(pk)(sk)} \right. \\
& \left. + (2ps + 2m^2 - q^2)[(pk)^{-1} - (sk)^{-1}] \right), \quad (2.9)
\end{aligned}$$

where q^2 is the four momentum transfer to the proton target squared

$$q^2 = 2m^2 - 2E_s E_p + 2|s||\mathbf{p}|\cos\theta + 2M^2 - 2\omega(E_s - E_p) - 2\omega|\mathbf{u}|\cos\theta \quad (2.10)$$

and ω is the photon energy

$$\omega = \frac{1}{2} \frac{u^2 - M_j^2}{u_0 - |\mathbf{u}|\cos\theta}. \quad (2.11)$$

Equation 2.8 is easily integrated over ϕ by applying some integration formulas giving,

$$\begin{aligned}
\frac{d^2\sigma_{jr}}{d\Omega dp} &= \frac{\alpha^3}{(2\pi)} \left(\frac{E_p}{E_s}\right) M^{-1} \int_{-1}^1 \frac{\omega d(\cos\theta_k)}{2q^2(u_0 - |\mathbf{u}| \cos\theta_k)} \\
&\times \left(M^2 F_j(q^2) \left\{ \frac{-2\pi a m^2}{(a^2 - b^2)^{3/2}} \left[2E_s(E_p + \omega) + \frac{q^2}{2} \right] - \frac{2\pi a' m^2}{(a'^2 - b'^2)^{3/2}} \left[2E_p(E_s + \omega) + \frac{q^2}{2} \right] - 4\pi \right. \right. \\
&+ 4\pi \left(\frac{v}{(a^2 - b^2)^{1/2}} - \frac{v'}{(a'^2 - b'^2)^{1/2}} \right) \left\{ m^2(sp - \omega^2) + (sp) \left[2E_s E_p - (sp) + \omega(E_s - E_p) \right] \right\} \\
&\quad + \frac{2\pi}{(a^2 - b^2)^{1/2}} \left[2(E_s E_p + E_s \omega + E_p^2) + \frac{q^2}{2} - (sp) + m^2 \right] \\
&\quad + \frac{2\pi}{(a'^2 - b'^2)^{1/2}} \left[2(E_s E_p + E_p \omega + E_s^2) + \frac{q^2}{2} - (sp) + m^2 \right] \left. \right\} \\
&\quad + G_j(q^2) \left[\left(\frac{2\pi\alpha}{(a^2 - b^2)^{3/2}} + \frac{2\pi\alpha'}{(a'^2 - b'^2)^{3/2}} \right) \right] \\
&\quad + 8\pi \left(\frac{v}{(a^2 - b^2)^{1/2}} - \frac{v'}{(a'^2 - b'^2)^{1/2}} \right) (sp)(sp - 2m^2) \\
&\quad + e\pi[(a^2 - b^2)^{-1/2} - (a'^2 - b'^2)^{-1/2}](2sp + 2m^2 - q^2) \quad (2.12)
\end{aligned}$$

After that, the radiative correction to the continuum state needs to be calculated. It will be derived from a series of Equations. First the radiative cross section, regardless of straggling effects, is calculated via,

$$\left(\frac{d\sigma_r}{d\Omega dp} \right) (E_s, E_p) = \left(\frac{d\sigma}{d\Omega dp} \right) (E_s, E_p) [1 + \delta_r(\Delta)] + \left(\frac{d\sigma_r}{d\Omega dp} \right) (\omega > \Delta) \quad (2.13)$$

where

$$\begin{aligned}
\delta_r(\Delta) &= \frac{-2.0\alpha}{\pi} \left[\frac{28}{9} - \frac{13}{6} \ln \frac{2(sp)}{m^2} \left(\ln \frac{E_s}{\Delta E} + \ln \frac{E_p}{\Delta E} - \right) \left(\ln \frac{2(sp)}{m^2} - 1 \right) \right. \\
&\quad \left. - \Phi \left(-\frac{E_s - E_p}{E_p} \right) - \Phi \left(-\frac{E_s - E_p}{E_s} \right) \right] \quad (2.14)
\end{aligned}$$

$$\left(\frac{d\sigma_r}{d\Omega dp}\right)(\omega > \Delta) = \frac{\alpha^3 E_p}{2\pi M E_s} \int_{-1}^1 d(\cos\theta_k) \int_{\Delta}^{\omega_{max}(\cos\theta_k)} \frac{\omega d\omega}{q^4} \int_0^{2\pi} B_{\mu r}^c T_{\mu r} d\phi_k \quad (2.15)$$

and $(\frac{d\sigma}{d\Omega dp})(E_s, E_p)$ is the continuum non radiative cross section, $\Phi(x)$ is the Spence function which is defined in Equation 2.40 below. Then, the peaking approximations method is used to integrate the cross section formula.

2.2 Peaking Approximation

Mo and Tsai[1] used their cross section formula to achieve the peaking approximation formula. They integrated Equation 2.12 to show examples of peaking. Figure 2.1 (a)-(c) show radiative tails from the elastic peak in electron-proton scattering. The Equation took the following parameters, the incident electrons have energy of 20 GeV, the angle of scattering is 5° , and the energy of the scattered electrons is 18 GeV for (a), 12 GeV for (b), and 6 GeV for (c).

These plots can be interpreted in the following way. When θ_k is equal to θ_s or θ_p , then the integrand peaks strongly, which means that most of the photons are emitted in those directions. There are two peaks in the plot: the s peak, which refers to the direction of the incident electron, and the p peak, which refers to the direction of scattered electrons. The width of those peaks is calculated by $(m/E_s)^{\frac{1}{2}}$ and $(m/E_p)^{\frac{1}{2}}$, respectively, due to increasing and decreasing of some parameters, and E_s is higher than E_p . It is noted in (b) and (c) that when E_p is small, a third peak near $\cos\theta = 1$ is appears. This peak is not considered, therefore the peaking approximation at low energy is not considered trustworthy.

Figure 2.1 (d),(e), and (f) represent radiative tails from the elastic peak in muon-proton scattering. The parameters that were used to make the plots were: the incident muons have energy of 20 GeV, the angle of scattering is 5° , and the energy of the scattered muons have energy of 18.3 GeV for (d), 12.5 GeV for (e), and 6 GeV for (f). These

plots show that muon-proton scattering doesn't have nearly as prominent peaks as shown in electron-proton scattering, but they are present nonetheless.

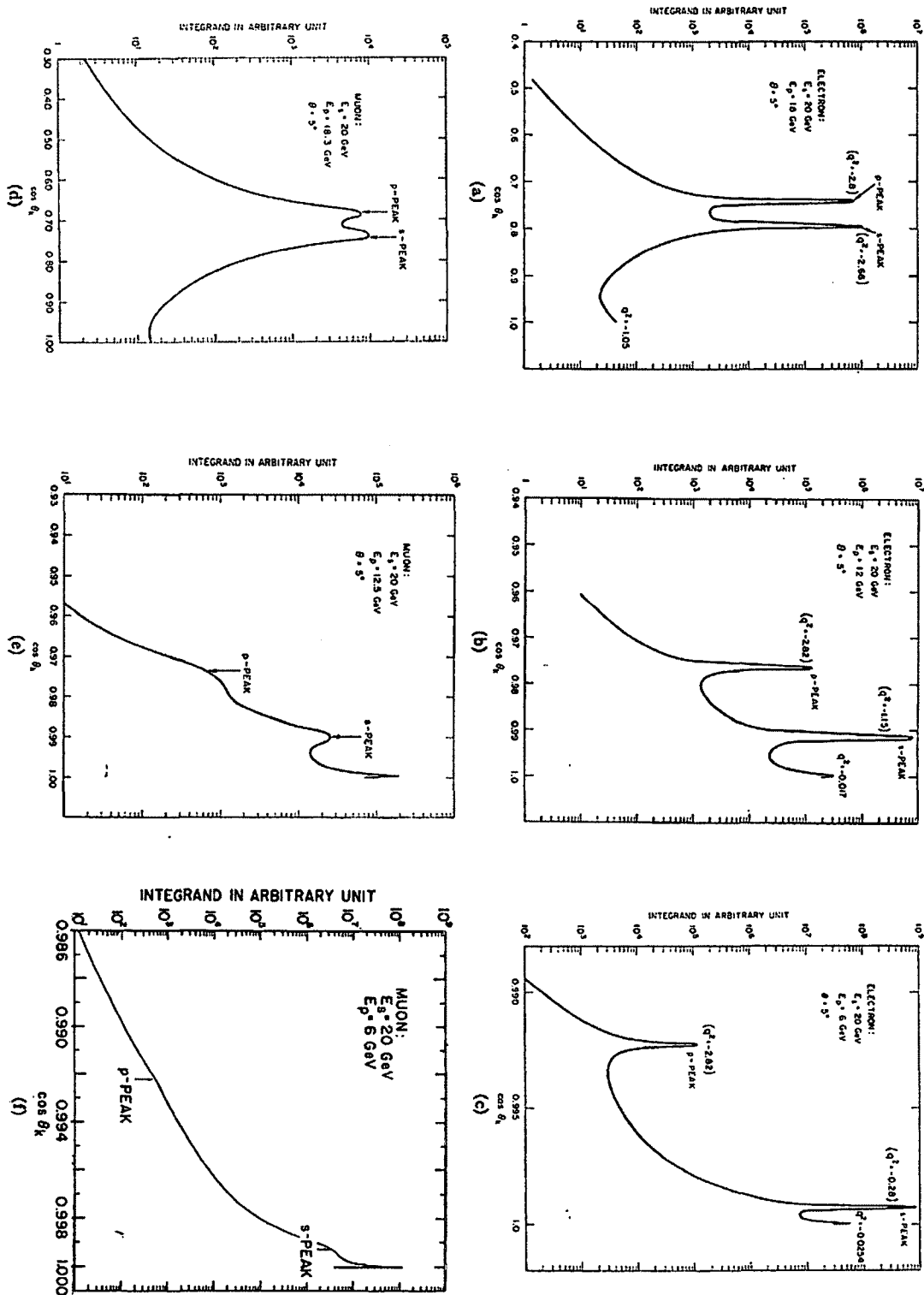


Figure 2.1: Integrand of Equation 2.12 to show peaking

To obtain the peaking approximating Mo and Tsai [1] started from radiative formula Equation 2.8. They assumed that the parts that contain $(sk)^{-2}$ and $(sk)^{-1}$ in the Equation only add value to the s peak, while the p peaks are only affected by the Equation parts that contain $(pk)^{-2}$ and $(pk)^{-1}$. Moreover, they assumed that the terms that do not contain (sk) or (pk) are adding an equal amount of value to the s peak and p peak. The terms that contain (sk) or (pk) in the denominator are the crucial part of the Equation. Therefore, these terms are integrated. The variables that associate with these terms are calculated with regards to their associated peak. Finally, the approximation peak was expressed as

$$\frac{d\sigma}{d\Omega dp}(E_s, E_p) = w_s^{-1} t_s \frac{M + (E_s - w_s)(1 - \cos\theta)}{M - E_p(1 - \cos\theta)} X \frac{d\sigma_j}{d\Omega}(E_s - w_s) + w_p^{-1} t_p d\sigma_j d\Omega(E_s) \quad (2.16)$$

where

$$w_s = \frac{1}{2}(u^2 - M_j^2)/[M - E_p(1 - \cos\theta)] \quad (2.17)$$

and

$$w_p = \frac{1}{2}(u^2 - M_j^2)/[M - E_s(1 - \cos\theta)]. \quad (2.18)$$

2.3 Straggling Effect

The effect of electron straggling in the target has to be taken into account. That is due to the effect that the internal bremsstrahlung effect is equal to the effect of two external radiators. The radiators are placed before and after the scattering with thickness

$$t_{i,f} = \frac{3\alpha}{4\pi} \left[\ln \left(-\frac{q^2}{m^2} \right) - 1 \right], \quad (2.19)$$

where q is the four-momentum transfer, and m is the electron mass. Bethe and Heitler [10], came up with a formula to calculate the straggling effects,

$$I(E_0, E, t) = E_0^{-1} \frac{\ln(E_0/E)^{(t/\ln 2)-1}}{\Gamma(t/\ln 2)} \quad (2.20)$$

$I(E_0, E, t)dE$ is a function that calculates the probability of finding an electron that has initial energy of E_0 and travelled a distance t in the target in the energy interval dE . This formula has some flaws; such as that it does not provide an acceptable accuracy. Therefore, Mo and Tsia [1] modified it to get more accurate straggling

$$I(E_0, E, t) = bt(E_0 - E)^{-1} + \left[\frac{E}{E_0} + \frac{3}{4} \left(\frac{E_0 - E}{E_0} \right)^2 \right] \left(\ln \frac{E_0}{E} \right)^{(bt)} \quad (2.21)$$

where

$$b = \frac{4}{3} \left[\frac{1}{9} \frac{Z + 1}{Z + \xi} (\ln(183Z^{1/3}))^{-1} \right] \quad (2.22)$$

and

$$\xi = \frac{\ln(1440Z)^{-2/3}}{\ln(183Z)^{-1/3}}. \quad (2.23)$$

Mo and Tsia [1] claimed that this Equation is "accurate to within 1% in the range $(0.5E_0 < EE_0)$ and within 2% in the range $0.05E_0 < E < E_0$ ". It was proven by Bethe and Heitler[10] that if the bremsstrahlung cross section was calculated by

$$\frac{d\sigma}{dE} = \left(\frac{bA}{X_0N} \right) \left[E_0 \ln \left(\frac{E_0}{E} \right) \right]^{-1} \quad (2.24)$$

then,

$$I(E_0, E, t) = E_0^{-1} \frac{\ln(E_0/E)^{(bt-1)}}{\Gamma(bt)}, \quad (2.25)$$

where A is atomic weight, N is Avogadro's number, and X_0 is the radiation length. Furthermore, when bt is small then,

$$I(E_0, E, t) = \left(\frac{N}{A} X_0 \frac{d\sigma}{dE} \right) \left(\ln \frac{E_0}{E} \right)^{bt}. \quad (2.26)$$

If the electron interacts with the atoms in the target only one time, then $I(E_0, E, t)$ will only equal the first part of the Equation. Therefore, an accurate method of calculation of $d\sigma/dE$ needs to be used:

$$\frac{d\sigma}{dE} = X_0^{-1} \frac{A}{N} \frac{4}{3} (E_0 - E)^{-1} \left[\frac{E}{E_0} + \frac{3}{4} \left(\frac{E_0 - E}{E_0} \right)^2 \right] \left(1 + \frac{E}{9E_0} \frac{Z + 1}{Z + \xi} [\ln(183Z^{-1/3})]^{-1} \right) \quad (2.27)$$

where X_0 is a unit radiation length that was defined by Bethe and Ashkin[11],

$$\frac{1}{X_0} = \left(\frac{4N}{A} \right) \alpha r_0^2 Z(Z + \xi) \ln(183Z^{-1/3}). \quad (2.28)$$

If b is calculated from Equation 2.22, then $d\sigma/dE$ will agree for both the Mo and Tsai and Bethe and Heitler Equation within 10% when $E = .35E_0$. However, they will disagree if $E < 0.35E_0$. $(\ln E_0/E)^{bt}$ is a correction factor that applies when the electron hit the atoms several times. It should be correct within the energy range $0.35E_0 < E < E_0$. It should be less than one when $E > 0.37E_0$, and larger than one when $E < 0.37E_0$. From Equation 2.21 came an equation to calculate the fraction of electrons. The electrons will be with initial energy E_0 , and energy range $E_\Delta \leq E \leq E_0$ after scattering from a target with thickness t ,

$$\begin{aligned} \int_{E_0-\Delta}^{E_0} I_e(E_0, E, t) dE &= \left(\frac{\Delta}{E_0} \right)^{bt} \quad \text{for} \quad \left(\frac{\Delta}{E_0} \right) \ll 1 \\ &= \exp \left[-bt \ln \left(\frac{E_0}{\Delta} \right) \right] \\ &= 1 - bt \ln \left(\frac{E_0}{\Delta} \right) + \dots \end{aligned} \quad (2.29)$$

If an electron scattered through a large angle $\theta \gg m/E_0$, target of thickness T , and a cross section $(d\sigma/d\Omega dE'_p)(E'_s, E'_p, \theta) = \sigma(E'_s, E'_p)$; then, the measured cross section

due to straggling is

$$\begin{aligned}
\sigma_t(E_s, E_p, T) &= d\sigma_t/d\Omega dE(E_s, E_p, T) \\
&= \int_0^T \frac{dt}{T} \int_{E_s \min(E_p)}^{E_0} dT'_s \int_{E_p}^{E_p \max(E'_s)} dE'_p I_s(E_s, E'_s, t) \sigma(E'_s, E'_p) I_e(E'_p, E_p, T-t)
\end{aligned} \tag{2.30}$$

where $E_s \min(E_p)$ is the minimum allowed value of E_s when $E'_p = E_p$. $E_p \max(E'_s)$ is the maximum value of E'_p . This Equation calculates the elastic peak radiative correction straggling effects. Also, it calculates the elastic peak radiative tail straggling effect. It differs from the previous point by only measuring E_p not equal to $E_{p \max}$. Finally, it calculates the radiative correction to the continuum state straggling effects.

2.4 Perturbation Theory

Perturbation theory is used to find the solutions that will help calculate the radiative correction. Perturbation theory is a systematic correction scheme to find an approximate solution, order by order in a small parameter relevant to the problem being solved.

2.4.1 Radiative Correction to the Elastic Peak

Schwinger [1] was involved in calculating the radiated correction to elastic peak due to this correction. Figure 2.2 shows the Feynman diagram representing electron proton elastic scattering. At first he calculated it for potential scattering. Then, he concluded that the measured cross section and lowest order of cross section, which is known as Born approximation, are related to each other by a special factor. The factor was $1+\delta$.

$$\left. \frac{d\sigma}{d\Omega} \right|_{meas} = (1 + \delta) \left(\frac{d\sigma}{d\Omega} \right) \Big|_{Born}, \tag{2.31}$$

where,

$$\delta = \frac{-2.0\alpha}{\pi} \left\{ \left(\ln \frac{E_i n}{\Delta E} - \frac{13.0}{12.0} \right) \left(\ln \frac{-q^2}{m^2} - 1.0 \right) + \frac{17.0}{36.0} + \frac{1}{2} f(\theta) \right\}, \quad (2.32)$$

$$f(\theta) = \ln \left(\sin^2 \frac{1}{2} \theta \right) \ln \left(\cos^2 \frac{1}{2} \theta \right) + \Phi \left(-\sin^2 \frac{1}{2} \theta \right), \quad (2.33)$$

and $\frac{d\sigma}{d\Omega}|_{meas}$ is the measured cross section, $\frac{d\sigma}{d\Omega}|_{Born}$ is the lowest order cross section, q is the four-momentum transfer, E is the energy of scattered electrons, and ΔE is the energy range over which the approximation is considered valid.

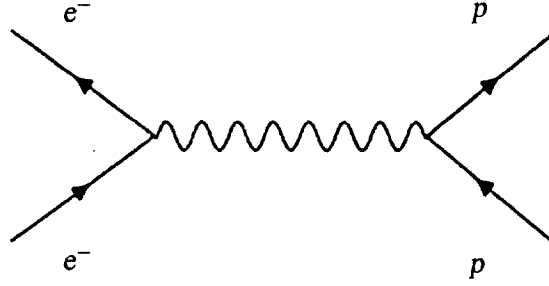


Figure 2.2: Feynman diagram for electron-proton elastic scattering

The Schwinger method works well for potential scattering. However in his Equation, as ΔE approaches zero, δ will approach negative infinity. Then, $\frac{d\sigma}{d\Omega}|_{meas}$ will approach negative infinity as well. That is a non-physical result. In the physical world, if ΔE goes to zero, δ should be also zero. This problem arises due to the ignored photon emission. Mo and Tsai suggested that if the system needs a higher order radiative correction, then δ is changed to e^δ .

After that other scholars worked on modifying Schwinger's Equations to fit any system. In Yennie and Suura's work[12] and Yennie, Frautschi, and Suura's work[13], they verified that a part of the δ , which is the infrared divergent δ_{inf} in Equation 2.32 must be exponential, such as $\delta_{inf} \rightarrow e^{\delta_{inf}}$,

$$\delta_{inf} = \frac{-2.0\alpha}{\pi} \left(\ln \frac{-q^2}{m^2} - 1 \right) \ln \frac{E_i n}{\Delta E}. \quad (2.34)$$

The δ term consists of mainly three parts: infrared, vertex (Figure 2.3 shows its Feynman diagram) and vacuum (Figure 2.4 shows its Feynman diagram), which is "the vacuum polarization due to the electron pair in the bubble". δ_{inf} was defined in Equation 2.34. The other parts are defined as follows:

$$\delta_{vac} = \left(\frac{2.0\alpha}{\pi}\right) \left[\left(\frac{-5}{9}\right) + \frac{1}{3} \ln\left(\frac{-q^2}{m^2}\right) \right] \quad (2.35)$$

$$\delta_{vertex} = \left(\frac{2.0\alpha}{\pi}\right) \left[-1 + \frac{3}{4} \ln\left(\frac{-q^2}{m^2}\right) \right]. \quad (2.36)$$

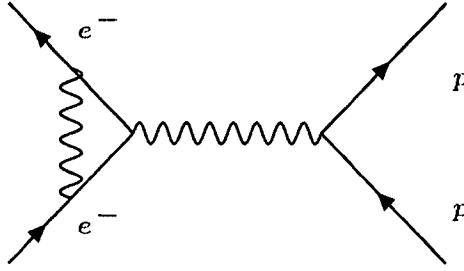


Figure 2.3: Feynman diagram of the δ Vertex

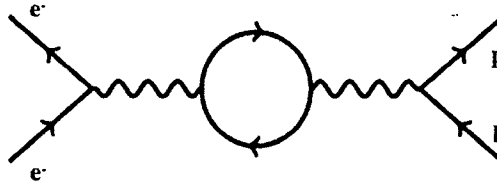


Figure 2.4: Feynman diagram of the δ Vacuum

However, $(\delta_{vertex} + \delta_{vac})^2$ only gives 0.7 % of the energy. While e_{inf}^δ is an important part because ΔE is usually kept small due to the omission of the pion threshold. Another problem with the Schwinger Equations is that the momentum transfer $|-q^2|$ was not checked. If the moment transfer is larger than or equal to the target particle mass, then a new calculation is required. In that case, target recoil kinematical effects and photon emission dynamical effects are must be considered in the δ value.

Tsai modified Schwinger's Equation to include those effects to δ . He expresses it as follows:

$$\begin{aligned}
\delta = & \frac{-\alpha}{\pi} \left(\frac{28}{9} - \frac{13}{6} \left(\ln \frac{-q^2}{m^2} \right) + \left(\ln \frac{-q^2}{m^2} - 1 + 2Z \ln \eta \right) + \left(2 \ln \frac{E_1}{\Delta E} - 3 \ln \eta \right) - \Phi \left(\frac{E_3 - E_1}{E_3} \right) \right. \\
& - Z^2 \ln \frac{E_4}{M} + Z^2 \ln \frac{M}{\eta \Delta E} \left(\frac{1}{\beta_4} \ln \frac{1 + \beta_4}{1 - \beta_4} - 2 \right) + \frac{Z^2}{\beta_4} \left\{ \frac{1}{2} \ln \frac{1 + \beta_4}{1 - \beta_4} \ln \frac{E_4 + M}{2M} \right. \\
& \left. \left. - \Phi \left[- \left(\frac{E_4 - M}{E_4 + M} \right)^{\frac{1}{2}} \left(\frac{1 + \beta_4}{1 - \beta_4} \right)^{\frac{1}{2}} \right] \right\} \right. \\
& + Z \left[\Phi \left(- \frac{M - E_3}{E_1} \right) - \Phi \left(\frac{M(M - E_3)}{2E_3E_4 - ME_1} \right) + \Phi \left(\frac{2E_3(M - E_3)}{2E_3E_4 - ME_1} \right) + \ln \left| \frac{2E_3E_4 - ME_1}{E_1(M - E_2)} \right| \ln \frac{M}{2E_3} \right] \\
& - Z \left[\Phi \left(- \frac{E_4 - E_3}{E_3} \right) - \Phi \left(\frac{M(E_4 - E_3)}{2E_1E_4 - ME_3} \right) + \Phi \left(\frac{2E_1(E_4 - E_3)}{2E_1E_4 - ME_3} \right) + \ln \left| \frac{2E_1E_4 - ME_3}{E_3(M - E_1)} \right| \ln \frac{M}{2E_1} \right] \\
& - Z \left[\Phi \left(- \frac{M - E_1}{E_1} \right) - \Phi \left(\frac{M - E_1}{E_1} \right) + \Phi \left(\frac{2(M - E_1)}{M} \right) + \ln \left| \frac{M}{2E_1 - M} \right| \ln \frac{M}{2E_1} \right] \\
& + Z \left[\Phi \left(- \frac{M - E_3}{E_3} \right) - \Phi \left(\frac{M - E_3}{E_3} \right) + \Phi \left(\frac{2(M - E_3)}{M} \right) + \ln \left| \frac{M}{2E_3 - M} \right| \ln \frac{M}{2E_3} \right] \\
& - \frac{\alpha}{\pi} \left(- \Phi \left(\frac{E_1 - E_3}{E_1} \right) + \frac{Z^2}{\beta_4} \left\{ \Phi \left[\left(\frac{E_4 - M}{E_4 + M} \right)^{\frac{1}{2}} \left(\frac{1 + \beta_4}{1 - \beta_4} \right)^{\frac{1}{2}} \right] - \Phi \left[\left(\frac{E_4 - M}{E_4 + M} \right)^{\frac{1}{2}} \right] \right. \right. \\
& \left. \left. + \Phi \left[- \left(\frac{E_4 - M}{E_4 + M} \right)^{\frac{1}{2}} \right] \right\} \right). \quad (2.37)
\end{aligned}$$

Meister and Yenni[14] also edited Schwinger's Equation to take into account the effects. Their contribution is as follows:

$$\begin{aligned}
\delta = & \frac{\alpha}{\pi} \left\{ \left[\ln \frac{2p_1p_2}{m^2} - 1 \right] \ln \left[\eta \left(\frac{\Delta E_3}{E_3} \right)^2 \right] + \frac{13}{6} \ln \left(\frac{2p_1p_2}{m^2} \right) - \frac{1}{2} \ln^2 \eta - \frac{28}{9} \right\} \\
& + \frac{Z\alpha}{\pi} \left\{ \ln \eta \ln \left[\eta \left(\frac{E_1}{E_4} \right)^2 \left(\frac{\Delta E_3}{E_3} \right)^4 \right] - \beta \left(\frac{2E_1}{M} \right) + \beta \left(\frac{2E_3}{M} \right) \right\} \\
& + \frac{Z^2\alpha}{\pi} \left\{ \left[\frac{E_4}{p_4} \ln \left(\frac{E_4 + p_4}{M} \right) - 1 \right] \ln \left[\frac{E_1^2}{ME_4} \left(\frac{\Delta E_3}{E_3} \right)^2 \right] + \frac{3}{2} \ln \left(\frac{2E_4}{M} \right) - \frac{1}{2} \ln^2 \left(\frac{E_4}{M} \right) \right\}. \quad (2.38)
\end{aligned}$$

Here E_1 is the energy of the incident electron, E_3 is the energy of the scattered electron, and E_4 is the energy of the recoil nucleus, m is the mass of the electron, M is the mass of the target particle, and Z is the target particle atomic number. The

sign of Z is changed based on the incident particle e . When the incident particle is an electron e^- , then Z is positive, whereas Z is negative if the incident particle is positron e^+ . $\eta = \frac{E_1}{E_3}$. ΔE is equal to ΔE_3 , and they are equal if $E_{peak} - E_{min}$. β_4 is the target particle velocity. β is a step function that was defined in Meister and Yenni's paper[14] as

$$\beta(x) = (\ln^2 x)\theta(1 - x) \quad (2.39)$$

Φ is the Spence function which is defined as

$$\Phi(x) = \int_0^x \frac{-\ln|1 - y|}{y} dy. \quad (2.40)$$

Mo and Tsia[1] have compared the numerical values of Equations 2.37 and 2.38. Both Equations give the exact results for electron proton scattering. If Z becomes larger, Equation 2.37 is better than Equation 2.38, and Equation 2.37 gives an acceptable answer. The source of the difference in the results of these Equations is the Spence function. Meister and Yenni[14] used approximation methods to calculate the Spence function as the following

$$\begin{aligned} \Phi(x) &= x + \frac{1}{4}x^2 + \frac{1}{9}x^3 + \dots + \frac{x^2}{n^2} \quad \text{if } |x| \leq 1; \\ \Phi(1) &= \frac{1}{6}\pi \quad \text{and} \quad \Phi(-1) = \frac{1}{12}\pi^2; \\ \Phi(x) &= -\frac{1}{2}\ln^2|x| + \frac{1}{3}\pi^2 - \Phi\left(\frac{1}{x}\right) \quad \text{if } x > 1; \\ \Phi(x) &= -\frac{1}{2}\ln^2|x| + \frac{1}{6}\pi^2 - \Phi\left(\frac{1}{x}\right) \quad \text{if } x < -1; \end{aligned} \quad (2.41)$$

Beyond those limits, the results get more approximate: if $|x| < 1$, then $\Phi(x) = 0$, and if $|x| > 1$, then $\Phi(x) = -\frac{1}{2}\ln^2|x|$. This approximation is not useful because it causes an increase in the error by 1%. Since the Equation is using many Spence functions, the error is hard to calculate. Furthermore, this approximation gives an incorrect δ when Z is large.

Another reason to calculate δ is to understand the contributions to the real part of the two-photon exchange diagram. Both Tsai and Meister and Yenni[14] did not fully manage the two-photon exchange diagrams. They ignored the effects of the two-photon exchange diagrams' strong interactions. They only used the diagrams to find terms that can be substituted in the infrared divergence in real photon emission. Tsai only extracted the infrared terms. To achieve that, he used a well defined function:

$$k(p_i, p_j) = (p_i, p_j) \int_0^{-1} \frac{dy}{P_y^2} - \ln \frac{P_y^2}{\lambda} \quad (2.42)$$

$$P_y = P_i y + (1 - y)P_i$$

After the infrared term $k(p_i, p_j)$ is extracted from each diagram and is subtracted from the cross section, the remainder contributes only 0.1%, which is a small contribution to the cross section. On the other hand, Meister and Yenni[14] extracted spin-convection terms in addition to the infrared terms. They used complicated procedures to extract their terms.

Since both methods achieve their results via different paths, it is not clear which one represented the two-photon exchange accurately. These methods can be chosen and used based on the researcher's convenience. Also, before choosing the preferable method, the diagram must be assembled and add back the subtracted terms.

Another scholar, Erickson[15], computed the two-photon exchange contribution to electron-muon scattering. He also computed the diagrams' contributions to the cross section without the infrared contributions. Erickson's work is significant because it allows the comparison between the difference in electron-proton scattering and a model of the strong interaction in the two-photon exchange interaction.

Furthermore, the radiative correction may be combined with the effects of straggling in the target by

$$\left. \frac{d\sigma}{d\Omega} \right|_{meas} = \left(\left. \frac{d\sigma}{d\Omega} \right|_{Rosenbluth} \right) \exp(\delta + \delta_t) \quad (2.43)$$

$$\delta_t = - \left\{ \left[b_w t_{iw} + \frac{1}{2} b T \right] \ln \left(\frac{E_1}{\eta^2 \Delta E} \right) + \left[b_w t_{fw} + \frac{1}{2} b T \right] \ln \left(\frac{E_3}{\Delta E} \right) \right\}, \quad (2.44)$$

where T is target thickness, t_{iw} is the initial window thickness, t_{fw} is the final window thickness, and b_w and b are approximately $\frac{3}{4}$, however they can be calculated using Equation 2.22.

The term δ_t in muon elastic scattering can be approximated to zero. That is due to the fact that muon bremsstrahlung in the target is very small in comparison with electron bremsstrahlung. Furthermore, if the muon has small mass compared to its energy and momentum transfer, then Equations 2.37 and 2.38 can be updated. Each m may be changed to m_μ . Additionally, δ_{vac} (Equation 2.35) may be added to δ . The order of magnitude of the ratio between muon radiative correction and electron radiated correction cross sections is given by:

$$\frac{\delta_e}{\delta_\mu} = \left(\ln \frac{-q^2}{m_\mu^2} - 1 \right) \times \left(\ln \frac{-q^2}{m^2} - 1 \right)^{-1}. \quad (2.45)$$

2.5 Elastic Radiative Tail

The elastic peak radiative tail is calculated directly after collecting the elastic form factor from the experiment. The radiative tail in the deep inelastic region is calculated by adding the straggling effects in the target and the internal bremsstrahlung. The final formula is

$$\frac{d\sigma_{0,t+r}}{d\Omega dE_p}(E_s, E_p, T) = \frac{d\sigma_{0,t}(E_s, E_p, T)}{d\Omega dE_p} + \frac{d\sigma_{0,t}(E_s, E_p)}{d\Omega dE_p}. \quad (2.46)$$

On the other hand, it is more complex to calculate the radiative correction to the spectrum. That is due to the fact that its form factors need to be filtered before they can be applied into the Equation. The proton's elastic form factors are calculated via

$$F_0(q^2) = \frac{4(G_e^2 + \gamma G_m^2)}{(1 + \gamma)}, \quad (2.47)$$

$$G_0(q^2) = -q^2 G_m^2, \quad (2.48)$$

$$\gamma = \frac{-q^2}{4M_p^2}, \quad (2.49)$$

and

$$G_s = \frac{G_m}{2.793} = [1 - (\frac{q^2}{-0.71} GeV^2)]^{-2}. \quad (2.50)$$

2.6 Radiative Correction to Continuous Spectra

The next step, after subtracting the elastic radiative tail from the inelastic spectra, is to calculate the radiative correction for the spectrum's continuous part. The 3-3 or Δ resonance is used to calculate the radiative correction. A resonance is a compound state that forms in the low energy region. First, the 3-3 resonance non-radiative cross section is calculated by Equation 2.2 where the form factors are

$$F(q^2, M_j^2) = (\frac{2}{M_p}) G_2(q^2, M_j^2), \quad (2.51)$$

$$G(q^2, M_j^2) = 2M_p G_1(q^2, M_j^2), \quad (2.52)$$

where,

$$\begin{aligned} G_1(q^2, M_j^2) &= (\frac{Q^2}{-q^2}) G_2(q^2, M_j^2) \\ &= \frac{\Gamma M_3 3M_j^{-1}}{(M_j^2 - M_{33})^2 + \Gamma^2 M_{33}^2} Q^{*2} 2C_3^2(q^2) \frac{E_i^* + M_p}{3M_p}, \end{aligned} \quad (2.53)$$

$$Q^2 = (M_j^2 - q^2 - M_p^2)^2 (2M_p^2)^{-2} - q^2, \quad (2.54)$$

$$Q^{*2} = \frac{M_p^2 Q^2}{M_j^2}, \quad (2.55)$$

$$E_i^* = \frac{(M_j^2 + M_p^2 - q^2)}{(2M_j)}, \quad (2.56)$$

$$M_{33} = 1.236 \text{ GeV}, \quad (2.57)$$

$$\Gamma(M_j^2) = 0.1293 \text{ GeV} \frac{[0.85(p^*/m_\pi)]^3}{1 + [0.85(p^*/m_\pi)]^2}, \quad (2.58)$$

$$p^* = \left[\frac{(M_j^2 - M_p^2 + m_\pi^2)}{(2M_j)} \right]^2 - m_\pi^2, \quad (2.59)$$

$$[C_3(q^2)M_p]^2 = 2.05^2 \exp[-6.3(-q^2)^{\frac{1}{2}}][1 + 9(-q^2)^{\frac{1}{2}}]. \quad (2.60)$$

The spectrum will then be affected by the straggling of the electron in the target. Therefore, it will be calculated by

$$\begin{aligned} \frac{d\sigma_{tr}(E_s, E_p)}{d\Omega dE_p} &= \frac{d\sigma}{d\Omega dE_p}(E_s, E_p) \exp(\delta_t + \delta_r) + \left(\frac{\Delta}{E_p}\right)^{(1/2)f_p} \\ X \int_{E_{s\min}(E_p)}^{E_s - \Delta} \frac{dE'_s}{E'_s - E_s} &\left\{ t_s + \left(b_w t_{iw} + \frac{1}{2}bT\right) \left[x_s + \frac{3}{4}(1 - x_s^2)\right] \right\} (\ln x_s^{-1})^{f_s} \frac{d\sigma}{d\Omega dE_p}(E'_s, E_p) \\ &+ \left(\frac{\Delta}{E_s}\right)^{(1/2)f_s} \\ X \int_{E_p + \Delta}^{E_p \max(E_s)} \frac{dE'_p}{E'_R - E_R} &\left\{ t_p + \left(b_w t_{iw} + \frac{1}{2}bT\right) \left[x_p + \frac{3}{4}(1 - x_p^2)\right] \right\} (\ln x_p^{-1})^{f_s} \\ &\frac{d\sigma}{d\Omega dE'_R}(E_s, E'_p) \quad (2.61) \end{aligned}$$

where,

$$\delta_t = - \left[\left(b_w t_{iw} + \frac{bT}{2}\right) \ln \frac{E_s}{\Delta} + \left[b_w t_{fw} + \frac{1}{2}(bT)\right] \ln \frac{E_p}{\Delta} \right], \quad (2.62)$$

$$x_s = E'_s/E_s,$$

$$x_p = E'_p/E_p,$$

$$t_r = b^{-1} \left(\frac{\alpha}{\pi} \right) \left[\ln \left(\frac{2sp}{m^2} \right) - 1 \right],$$

$$f_s = bt_r + b_w t_{iw} + \frac{1}{2} bT,$$

$$f_p = bt_r + b_w t_{fw} + \frac{1}{2} bT,$$

$$t_{s,p} = \left(\frac{\alpha}{\pi} \right) \left\{ \frac{1}{2} (1 + x_{s,p}^2) \ln \left[\frac{2sp}{m^2} \right] - x_{s,p} \right\},$$

$$E_{s \min}(E_p) = \frac{m_\pi^2 + 2M_p m_\pi + 2M_p E_p}{2M_p - 2E_p(1 - \cos\theta)}$$

$$E_{p \max}(E_s) = \frac{2M_p E_p - 2M_p m_\pi - m_\pi^2}{2M_p - 2E_s(1 - \cos\theta)}.$$

Here $d\sigma/d\Omega E_p(E_s, E_p)$ is the non radiative cross section, T is the target thickness, t_{iw} is the initial window thickness, t_{fw} is the final window thickness and δ_r is obtained via Equation 2.14. The terms t_r and δ_r are used to approximate the photon emission effects in internal bremsstrahlung.

The non radiative cross section can be calculated using Equation 2.61. Equation 2.61 is equivalent to

$$\begin{aligned} \frac{d\sigma}{d\Omega dE_p}(E_s, E_p) &= \frac{d\sigma_{t_r}(E_s, E_p)}{d\Omega dE_p} \exp[-(\delta_t + \delta_r)] \exp(-\delta_t - \delta_r) \\ &+ \left(\frac{\Delta}{E_p} \right)^{(1/2)f_p} \int_{E_{s \min}(E_p)}^{E_s - \Delta} \frac{dE'_s}{E'_s - E_s} \psi(x_s) \frac{d\sigma}{d\Omega dE_p}(E'_s, E_p) \\ &+ \left(\frac{\Delta}{E_s} \right)^{(1/2)f_s} \int_{E_p + \Delta}^{E_{p \max}(E_s)} \frac{dE'_p}{E'_p - E_p} \psi(x_p) \frac{d\sigma}{d\Omega dE'_p}(E_s, E'_p) \quad (2.63) \end{aligned}$$

where

$$\psi(x_s) = \left\{ t_s + (b_w t_{iw} + \frac{1}{2} bT) \left[x_s + \frac{3}{4} (1 - x_s)^2 \right] \right\} \left(\ln \frac{1}{x_s} \right)^{f_s},$$

$$\psi(x_p) = \left\{ t_p + (b_w t_{fw} + \frac{1}{2} bT) \left[x_p + \frac{3}{4} (1 - x_p)^2 \right] \right\} \left(\ln \frac{1}{x_p} \right)^{f_p}.$$

The last Equation suggests that in any region, the non radiative cross section can be obtained from the measured cross section. Furthermore, if the cross section of any area of the spectrum is known, then the cross section of its neighbor can be obtained from it. That is very crucial because cross sections can be calculated without collecting all the data from the experiment.

2.7 Conclusion

Figure 2.5 shows examples of radiative tails from electron-proton and muon-proton elastic scattering. The parameters for these curves are $E_s = 20$ GeV, $\theta = 5^\circ$. The continuous curve is the elastic radiative tail curve from electron-proton scattering, which was calculated by Equation 2.12. The dashed curve also is an elastic radiative tail from electron-proton scattering. However, the curve was generated by using equivalent radiators. Continuous curves that represent the radiative corrected 3-3 resonance radiative tails are also shown. Dashed curve represents a 3-3 resonance radiative tail that is obtained using Equation 2.12. The dot-dashed curve is the radiative tail from muon-proton scattering. These curves represent the nature of the radiative tails from electron-proton and muon-proton scattering. They also represent the accuracy of the used formula. Figure 2.5 shows that the elastic peak radiative tail is larger than the 3-3 resonance radiative tail.

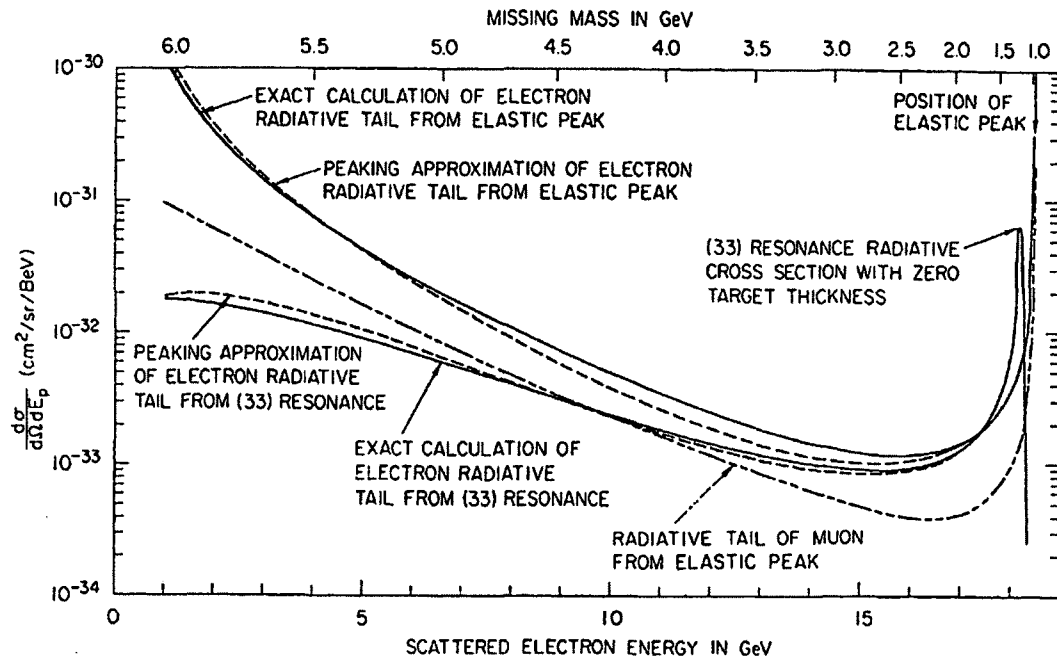


Figure 2.5: Radiative tails examples

There are many methods to calculate the radiative correction; however they have uncertainties for two reasons. First, the multiple photon exchange that is transferred between hadron and electron currents, and the second reason are the photon emission effects.

Radiative corrections can be treated in a few steps. After the experiment is finished and the results are extracted, the various formulae should be tested until it matches the data as closely as possible. Then, using the form factor Equations, the form factors $G_s(q^2)$ and $G_m(q^2)$ can be obtained. After that, the elastic peak radiative tail should be calculated and subtracted from the inelastic spectrum. Then, calculate the inelastic spectra radiative correction. Finally, compare the results with the experimental data.

Chapter 3

SIMULATION

The simulation was performed under the Geant4 platform. Geant4[3] is a physics simulation platform that uses Monte Carlo methods. Since there are a huge amount of data generated from the simulation, the Root framework [4] is used. Root is a data analysis framework that processes, analyzes, visualizes, and stores the data. Root is written in C++, therefore, C++ is mainly used in the simulation and data analysis.

In the simulation kit, the reaction regions represent the electron target in the physical experiment and its surrounding area. Reaction region 1 represents the liquid hydrogen target (LH_2). Reaction regions 2 and 3 represent the front entrance and back exit aluminum windows respectively. These windows correspond to the aluminum that encloses the LH_2 . The other 9 reaction regions are dummy targets for the surrounding area of the target. Their purpose is to count the pure aluminum and carbon that are used in the experiment for other reasons.

Furthermore, the simulation framework consists of 17 reaction types. Reaction types hold the physical models in the experiment. These models describe the particle interactions in the experiment. In this work we only used four reaction types: electron proton elastic scattering, electron aluminum elastic scattering, radiative scattering, and electron pion electro-production.

The simulation of the experiment started with only 10,000 events. At the end of the study, it ended up with 4 million events. During the testing, only a few QTor values were included. QTor is the value of the magnetic spectrometer current.

However, at the end we had 32 QTor values for 1.16 GeV, and 14 QTor values for 0.877 GeV.

The physical experiment has eight main detectors. As for the simulation, all the testing was done for one octant which is octant 7. Later, when we had a successful simulation and data analysis for this octant, we included all the octants.

3.1 Simulation Parameters

3.1.1 Incident Beam Energy, Spectrometer Current, and Electron Prime Window

In this study, there are two beam energies that have been simulated: Incident Beam Energy 1.16 GeV and Incident Beam Energy 0.877 GeV.

The current driving the magnetic spectrometer through which the electrons scattered in the target traverse is called QTor. It is measured by the unit, Amps (A). The simulated QTors range from 2000 to 9000 A. The step size was chosen to match measurements made in the physical experiment. Figure 3.1 shows the implementation of the QTor magnetic spectrometer in the physical experiment.

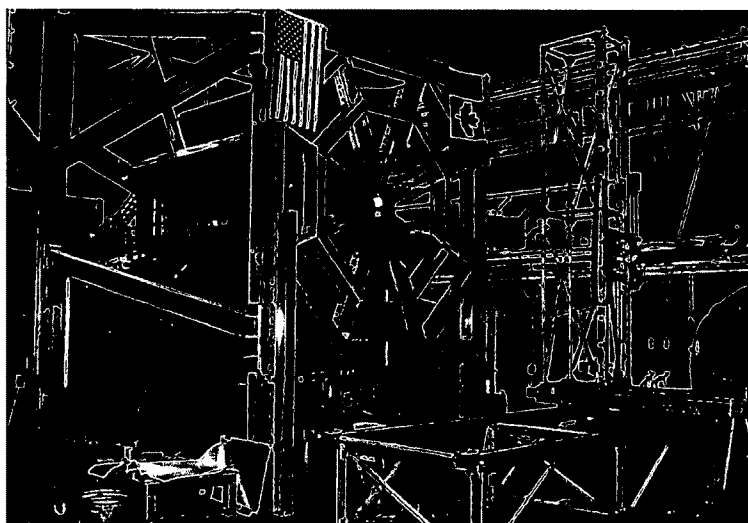


Figure 3.1: QTor magnet spectrometer.

For the purpose of this study, the important QTor points are elastic peak and Delta(Δ) peak. The Δ peak is at QTor = 6700 A which is the point where inelastically scattered electrons creating the Δ are at their maximum yield in this particular experiment. The elastic peak, which is at QTor = 8921A is the highest point in the elastic yield.

The electron prime window is the energy width of the scattered electron beam. At the beginning of this study, the electron window width was changed depending on the QTor current. Figures 3.2, 3.3, and 3.4 show the assigned electron beam energy window for QTor = 3000, 6700, and 9000 A respectively. After some tests, it was concluded that the window should be wide open during all simulations. Figures 3.5, 3.6, and 3.7 show the wide open electron beam energy window for QTor = 3000, 6700, and 9000 A respectively.

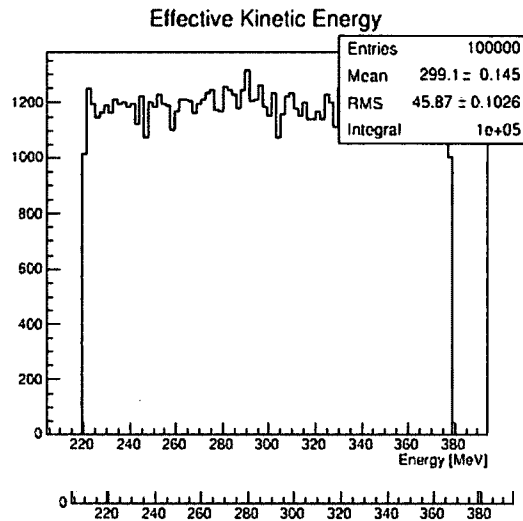


Figure 3.2: Electron prime window for QTor = 3000 A.

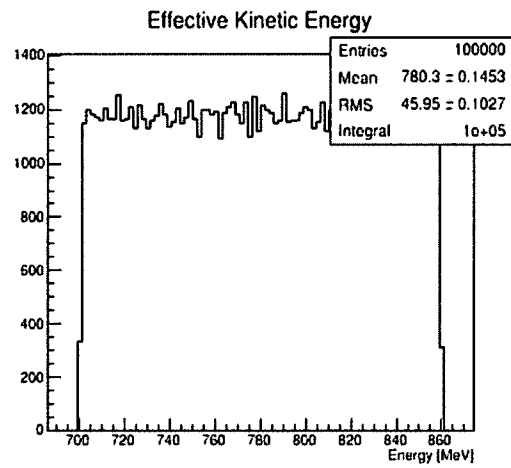


Figure 3.3: Electron prime window for $Q_{\text{Tor}} = 6700$ A.

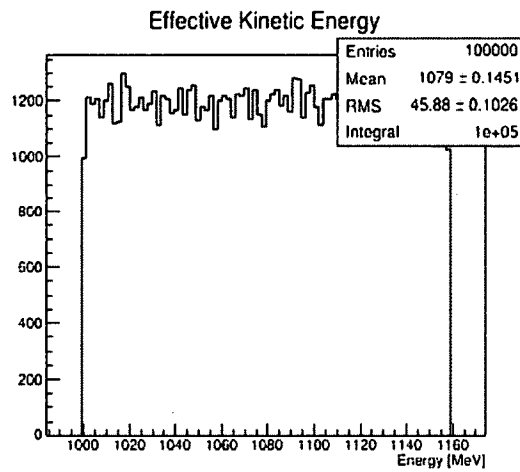


Figure 3.4: Electron prime window for $Q_{\text{Tor}} = 9000$ A.

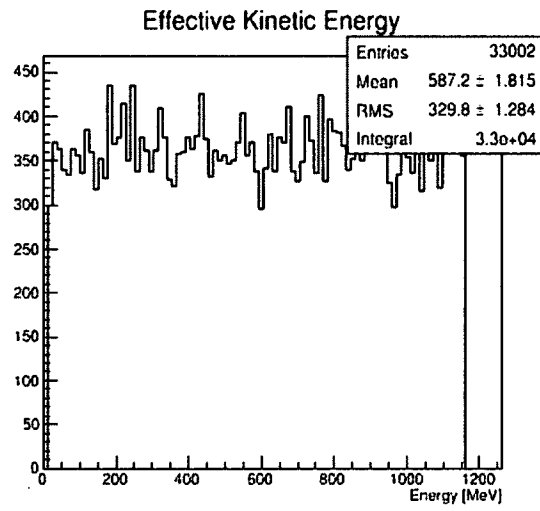


Figure 3.5: Open electron prime window for $Q_{\text{Tor}} = 3000$ A.

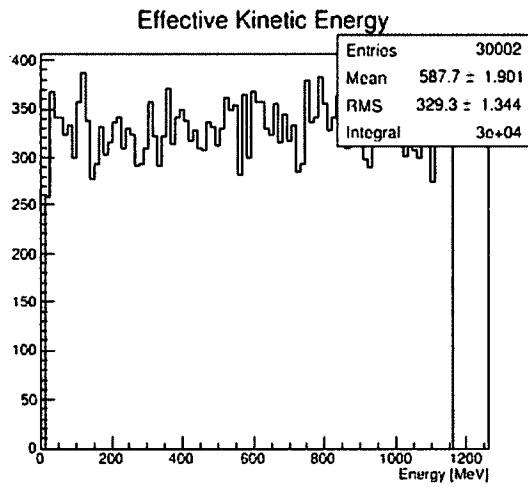


Figure 3.6: Open electron prime window for $Q_{\text{Tor}} = 6700$ A.

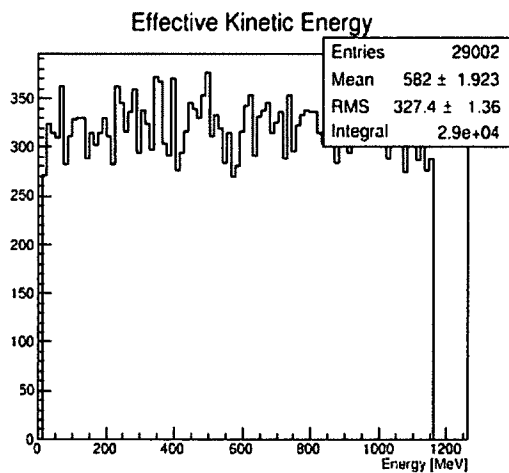


Figure 3.7: Open electron prime window for $Q_{\text{Tor}} = 9000$ A.

3.1.2 Angles

This experiment depends on two angles. Theta angle (θ) which is the angle of the scattered electron beam. It is ranged from 5.5 degrees to 12 degrees. Figure 3.8 shows a plot for θ angle for all Q_{Tor} currents. The Phi angle (ϕ) is ranged from -16 degrees to 16 degrees, and represents the azimuthal angle around the incident beam direction for one octant.

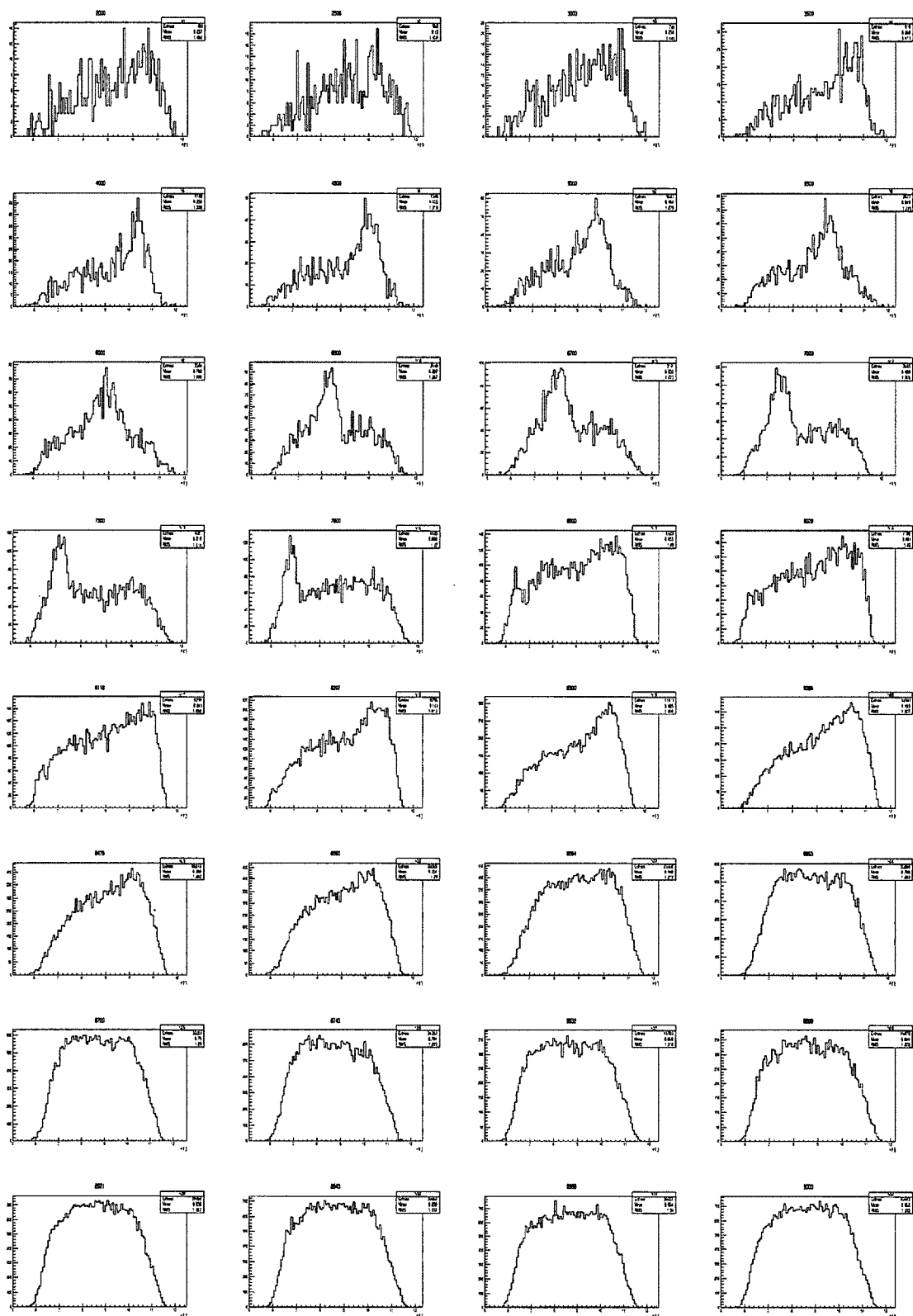


Figure 3.8: Theta angle for electron proton scattering.

3.1.3 Four Momentum Q^2

The four momentum Q^2 in this experiment is plotted in Figure 3.9. It is calculated via this Equation:

$$Q^2 = \frac{4E^2 \sin^2 \frac{\theta}{2}}{1 + 2\frac{E}{M} \sin^2 \frac{\theta}{2}} \quad (3.1)$$

where E is the incident electron energy, θ is the scattering angle and M the proton mass [6].

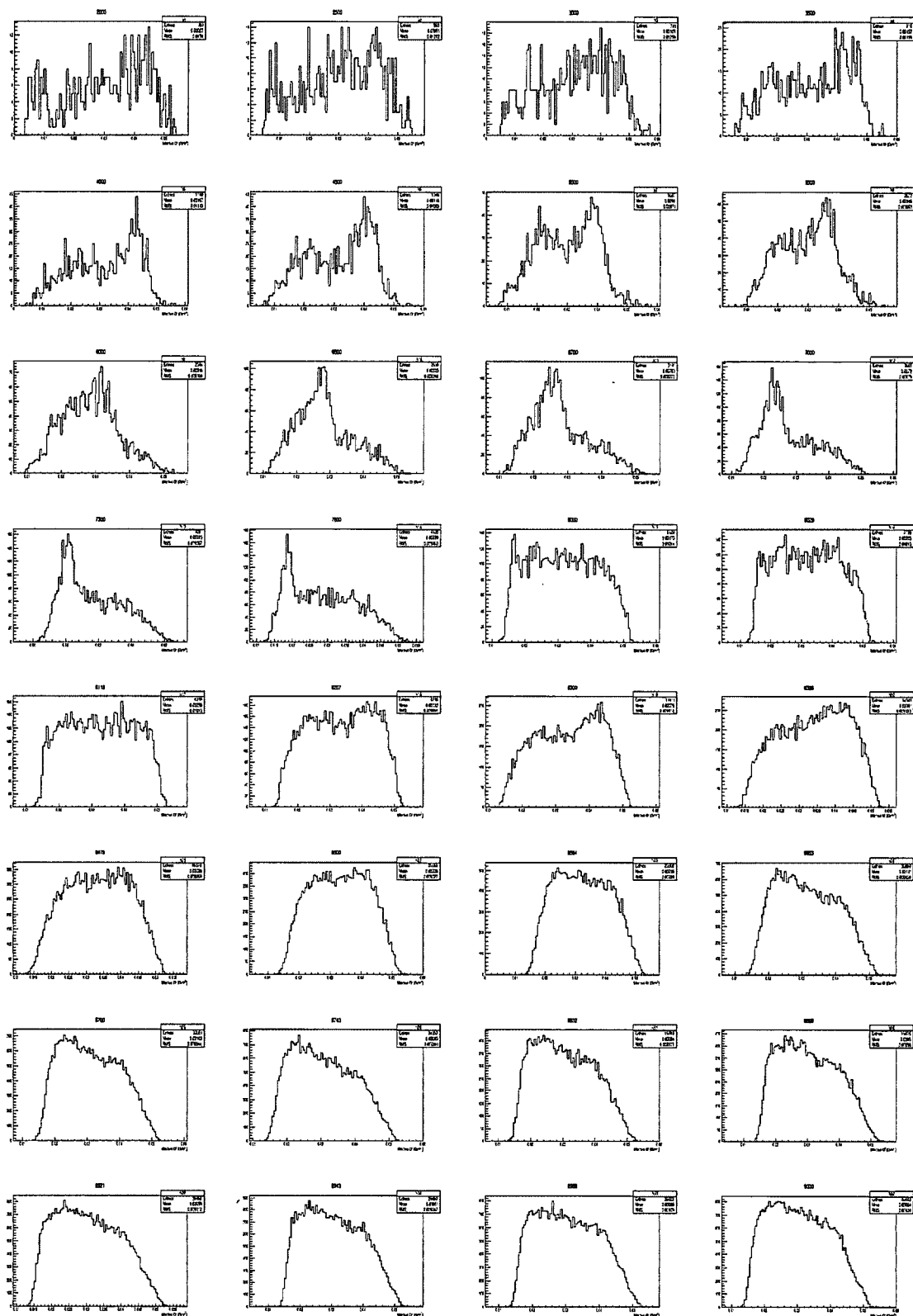


Figure 3.9: Four momentum energy Q^2

3.1.4 Invariant Mass of the Experiment W

The invariant mass of the scattered electrons of the experiment, W , in this experiment is plotted in Figure 3.10. It is calculated as

$$W^2 = E^2 - \vec{p}^2 \quad (3.2)$$

where E is the particle total energy and \vec{p} is its three momentum.

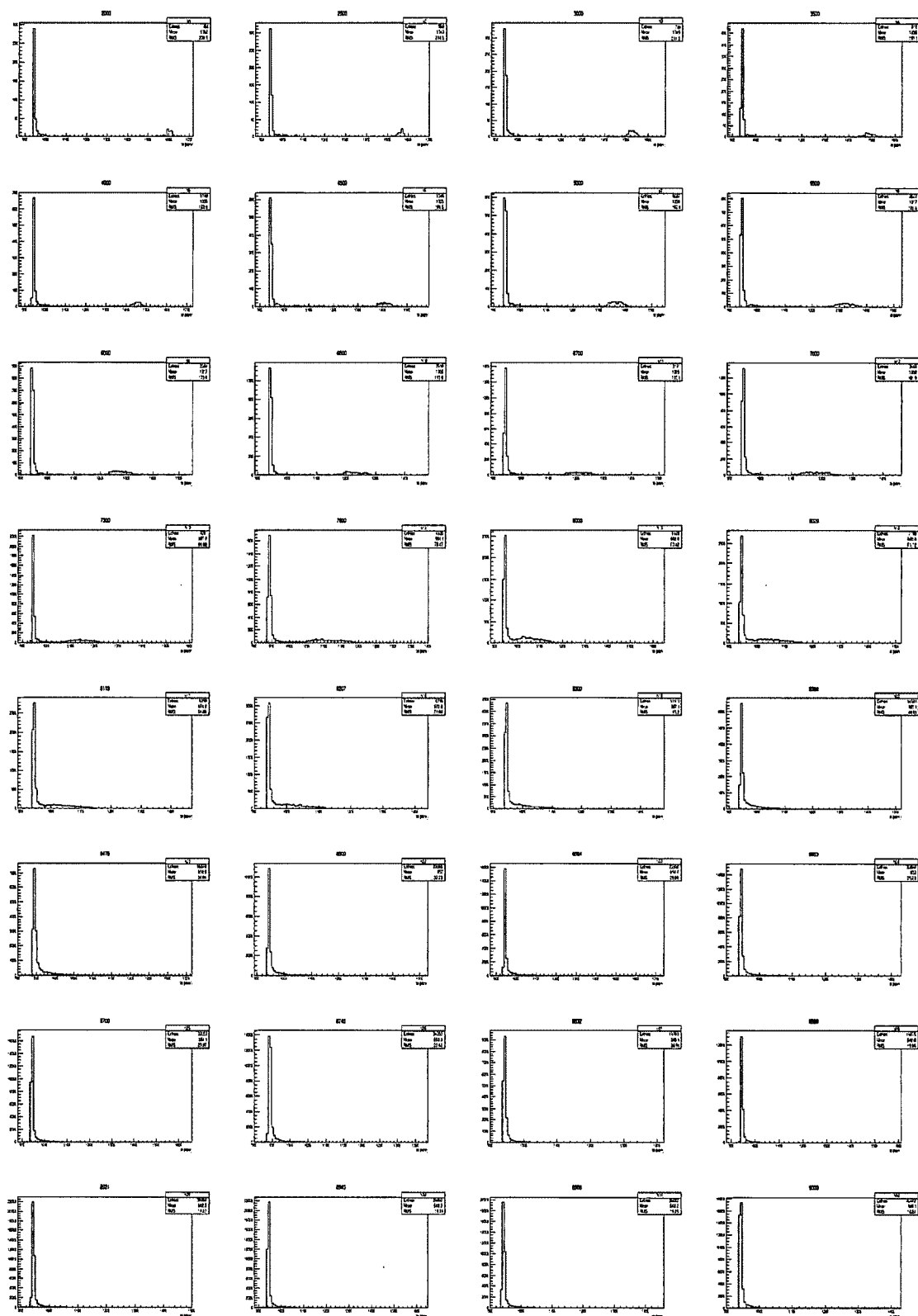


Figure 3.10: Invariant mass of the experiment W

3.1.5 Main Detectors

In the experiment there are eight identical main detectors positioned in eight octants, which are arranged symmetrically around the beam line. Their purpose is to collect the Čerenkov light that was produced by scattered electrons. Each detector is a bar that is made of two thin fused silica detectors with 2 cm lead radiators placed in front to generate an electron shower to amplify the generated Čerenkov light in the quartz. The entire spectrometer/ detector package consists of a detector, B field, and collimator. At the end of each bar, there is a photomultiplier tube (PMT) that collects the Čerenkov photons[5][6]. Figure 3.11 shows a sketch of the detectors, octant, and the way that they organized. Figure 3.12 explains how the detectors are installed and their place in the experiment.

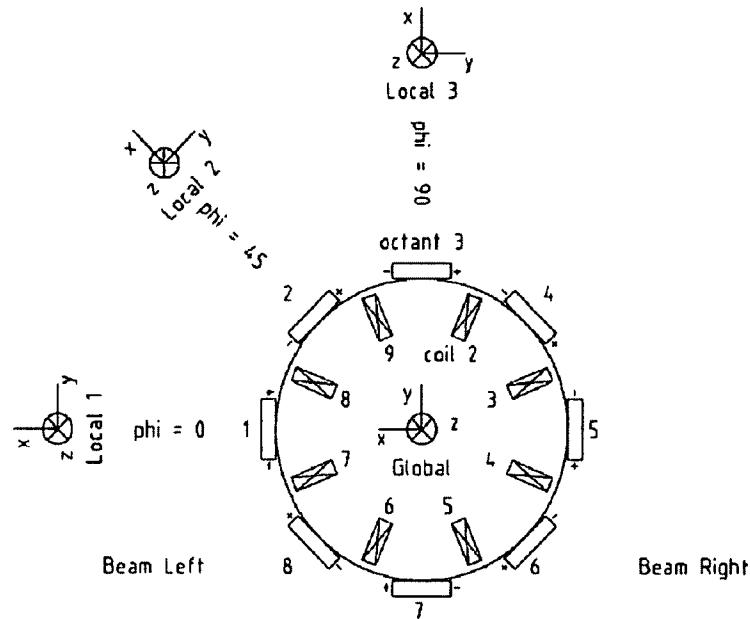


Figure 3.11: Sketch of the eight detectors.

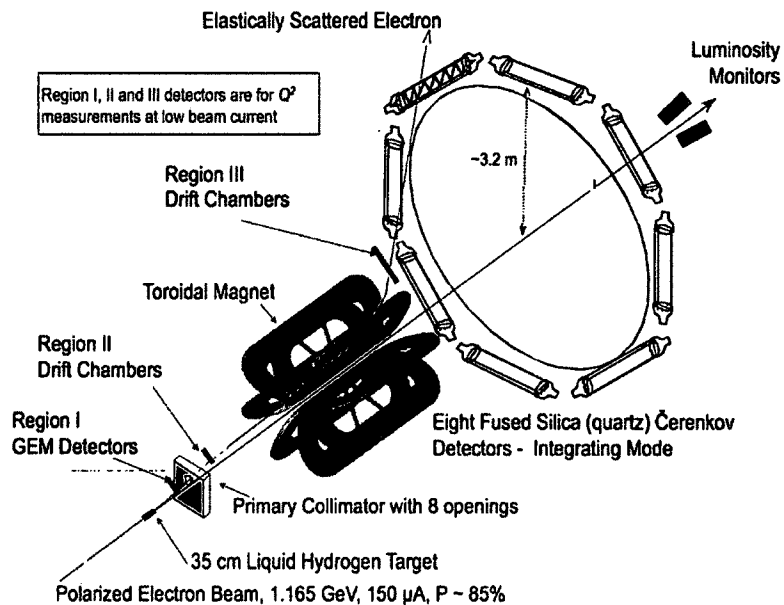


Figure 3.12: The eight detectors as part of the experiment

3.2 Random Number

The simulation was intended to match the physical experiment. Since physical experiments in general have many external influences that intervene with the results, the simulation has to use all aspects of those external factors. To ensure this happens, each simulation was divided into small sub-simulations that ran simultaneously. In the programming world, the sub-simulations copied each other and would be identical. So, to each sub-simulation, there has been assigned a random number. The purpose of it is to force the sub-simulation to not copy each other. The addition of these sub-simulations include all the aspects and noises from the simulation package.

3.3 Photoelectrons

Photoelectrons are an essential part of the simulation. Those are the electrons that are ejected from the face of the PMT by incident Čerenkov photons. They get generated by the PMT after the electron scattered and hit the target. Measuring the yield (Section 3.7) depends on photoelectrons, which makes them an important

part of extracting the $N \rightarrow \Delta$ asymmetry. In the case of yield, the PMTs count the amount of Čerenkov light generated in the detector, whereas for the rate only the number of events that hit the detector are being counted. That results in low photoelectron events to be collected in the rate. Therefore, the rate is not an accurate measure for the extracting the asymmetry. Thus the yield being simulated with the right amount of photoelectrons is the candidate to extract the asymmetry. Due to the PMTs having a hardware mismatch at approximately a 20% level, the experimental and simulation yields must be normalized at the elastic peak $Q_{\text{Tor}} = 8921\text{A}$.

3.4 Reaction Types

3.4.1 Electron Proton Radiative Scattering

Electron proton radiative scattering refers to the simulation by event generator type 7. It is the dominant event generator in this simulation. It simulates the radiated processes. It is divided into three parts: radiated elastic, deep inelastic (simply a label to designate Δ production in $e + p$ inelastic scattering), and elastic peak. Figure 3.13 shows this generator type and its parts in simulation. The radiated elastic part has the most influence in the simulation, while Δ production is important to measure the aspect of the simulation such as the inelastic fraction (Section 3.10.1). The elastic peak part was included in the early stages of this study. However, it failed near the elastic peak, therefore it has been replaced by a built-in function inside the simulation code, which calculated the electron proton elastic cross section. This code is not part of the internal Geant4 framework, but was added in the Qweak application of Geant4 by Qweak collaborators prior to this study.

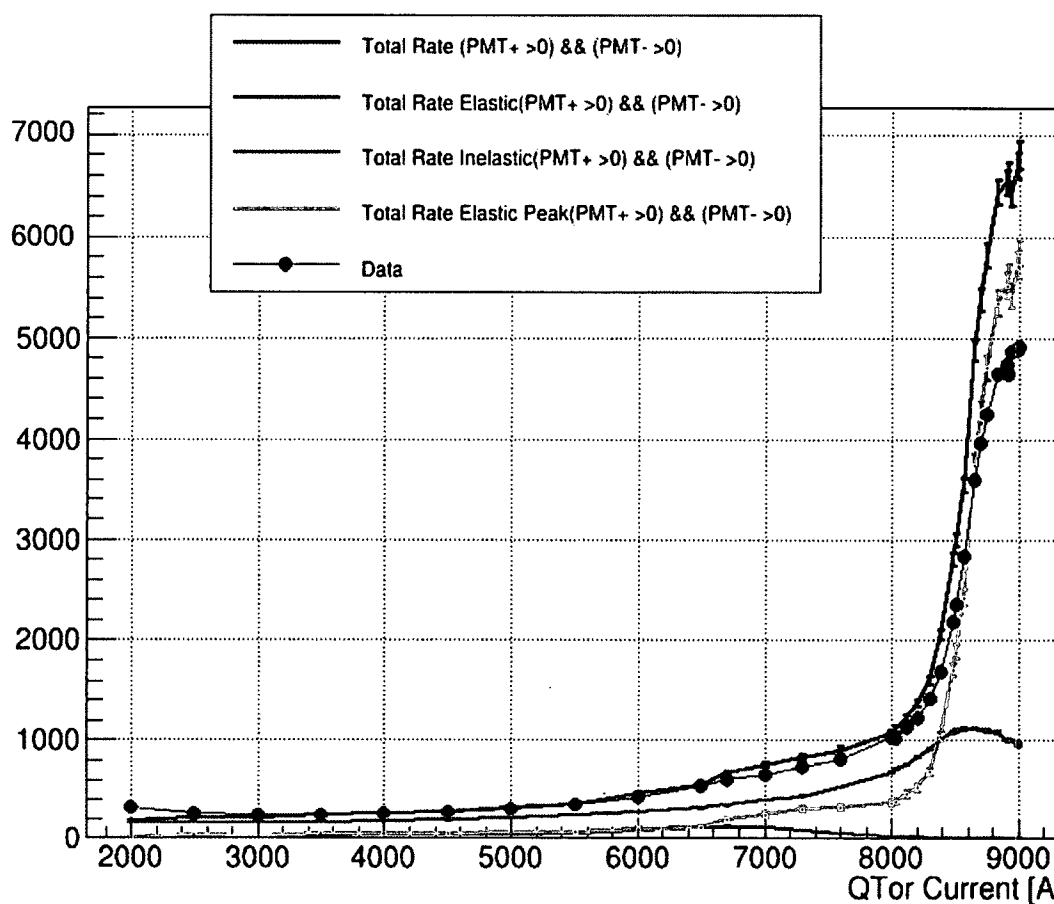


Figure 3.13: Variation of rate (in kHz/uA) as a function of QTor current (A) from generator 7 simulations, compared with data.

3.5 Electron Proton Elastic Scattering

The next step of the simulation was to add the elastic scattering from hydrogen, which was called event 1. It plays a huge part of the simulation, and has a big impact in the results. It is considered to be, along with event 7 radiated elastic, the dominant event seen in the study. The simulation package was modified to include a new radiative effect to event 1.

3.5.1 Schwinger Correction Included

As shown in Figure 3.13, the rate simulation matches the physical data rate shape, however it over predicts the data at the elastic peak. That is due to the fact that as the

electrons scatter from the beam in the hydrogen target, they radiate energy. There are three types of radiation: before vertex, after vertex, and as electrons interact with the protons at the vertex. The first two types of radiation are already built into Geant4. However, an internal radiative correction was needed.

Therefore, the Schwinger correction, adapted from the Mo and Tsai formalism[1], was added to the elastic generator scripts. The Schwinger correction, including a Feynman diagram representing it was described in detail in Chapter 2. Figure 3.14 shows a comparison between generator 1, elastic LH_2 target, before and after Schwinger correction was added. We observe approximately a 15% reduction at the elastic peak, as has been seen experimentally in other electron scattering measurements.

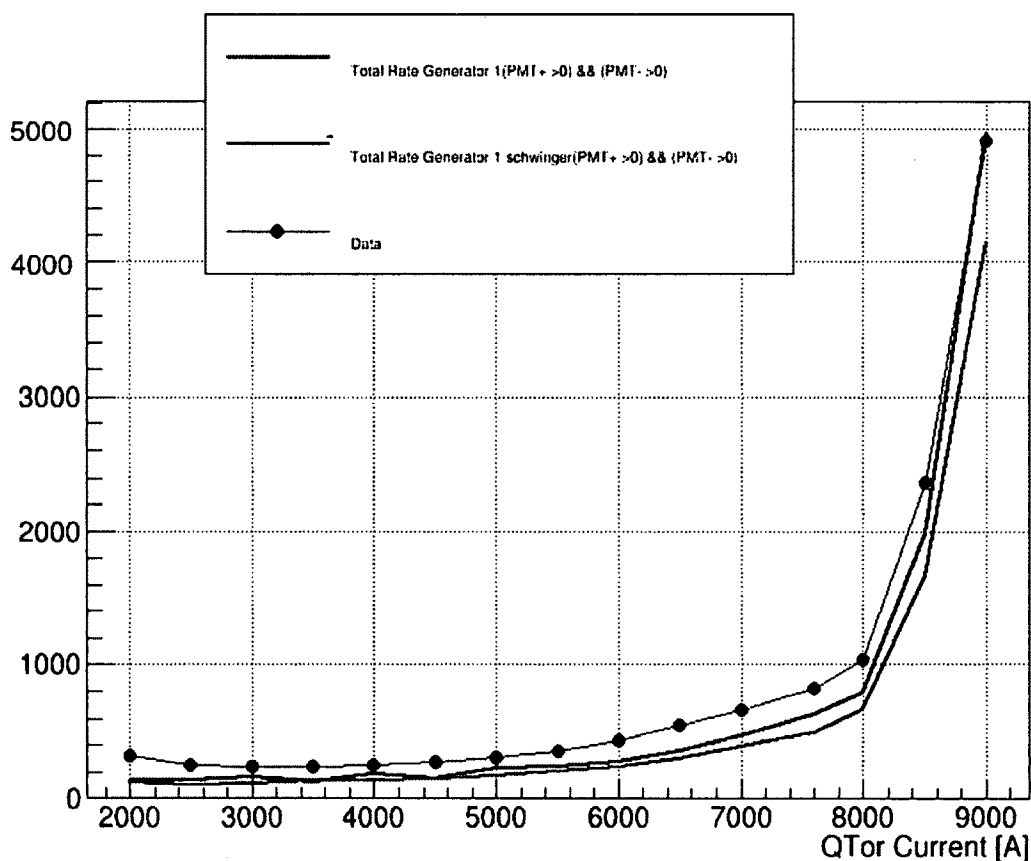


Figure 3.14: Generator 1 rate (in kHz/uA) with and without the Schwinger Correction compared to the data.

The Schwinger correction is represented as a change in the scattering cross section summarized in the correction δ ,

$$\frac{d\sigma}{d\Omega}|_{meas} = (1 + \delta)\left(\frac{d\sigma}{d\Omega}\right)|_{born} \quad (3.3)$$

where

$$\delta = \frac{-2.0 * \alpha}{\pi} \left[\left(\ln \frac{E_i n}{\Delta E} - \frac{13.0}{12.0} \right) \left(\ln \frac{-q^2}{m^2} - 1.0 \right) + \frac{17.0}{36.0} + \frac{1}{2} f(\theta) \right] \quad (3.4)$$

$$f(\theta) = \ln(\sin^2 \frac{1}{2} \theta) \ln(\cos^2 \frac{1}{2} \theta) + \Phi(-\sin^2 \frac{1}{2} \theta), \quad (3.5)$$

where $\frac{d\sigma}{d\Omega}|_{meas}$ is the measured cross section, $\frac{d\sigma}{d\Omega}|_{born}$ is the lowest order cross section, q is the four-momentum transfer, E is the energy of scattered electrons, and ΔE is a parameter which defines the energy range over which the correction is considered to be valid.

3.5.2 Δ Resonance Generator

At the early stages of the simulation, event type 5, which is the Δ resonance generator, was included. It was added to event type 1 and compared to the data. Then, they were compared to event type 7. event 7 radiated elastic and deep inelastic also includes the Δ resonance. Moreover, event 7 more closely matched the data. Therefore, event 5 was not needed from this point further. Figure 3.22 shows this generator combined with generator 1.

3.5.3 Electron Aluminum Generator

Event type 2 is the elastic scattering from aluminum. The simulation package was modified to include the new radiative filter to this event type as well. Event type 2 was added to the simulation two times. One time, it is included with the entrance window of aluminum. The other time, it is included with the exit window of aluminum. It was also modified to include the Schwinger correction(Section 3.5.1).

3.5.4 Pions

The last but not least part of the simulation is to add the pions. Pions were added to the simulation in three different regions. First, they were partnered with the hydrogen reaction region. Second, they were partnered with both the entrance and the exit window of the aluminum. The pion effect is very small.

3.6 Rate

Scattering rate is the measured electron rate in the detector. Its hardware implementation is that when the PMTs (section 3.1.5) detect Čerenkov photons from both the plus and minus sides, the electron rate is measured. Therefore, in the simulation it was required that at least one PE (section 3.3) is seen by both PMTs. Figure 3.15 shows the different weight of photoelectrons for rate ranging from greater than 0 PEs to greater than 4 PEs. Rate can simply be calculated by Equation 3.6

$$\mathcal{R} = \mathcal{L} \int_x \sigma(x) \epsilon(x), \quad (3.6)$$

For the Qweak experiment, the detected rate is measured with respect to the kinematics of the reaction. It is calculated via this Equation

$$\mathcal{R} = \mathcal{L} \int_{\phi, \cos\theta, E'} \frac{d\sigma}{d\phi d\cos\theta dE'} \epsilon(\phi, \cos\theta, E') d\phi d\cos\theta dE', \quad (3.7)$$

where \mathcal{R} is the scattering rate in the detector, σ is the cross section, θ is the effective solid angle of the detector, \mathcal{L} is the luminosity and E is the energy range over the detector acceptance[7].

As was stated in Section 3.2, each simulation was divided into multiple small sub-simulations. Rate is calculated by averaging the rates from the sub-simulations.

Moreover, the error is calculated via the quadric Equation

$$\text{Total Error} = \sqrt{\frac{1}{(\text{1st Simulation Error})^2} + \dots + \frac{1}{(\text{Last Simulation Error})^2}} \quad (3.8)$$

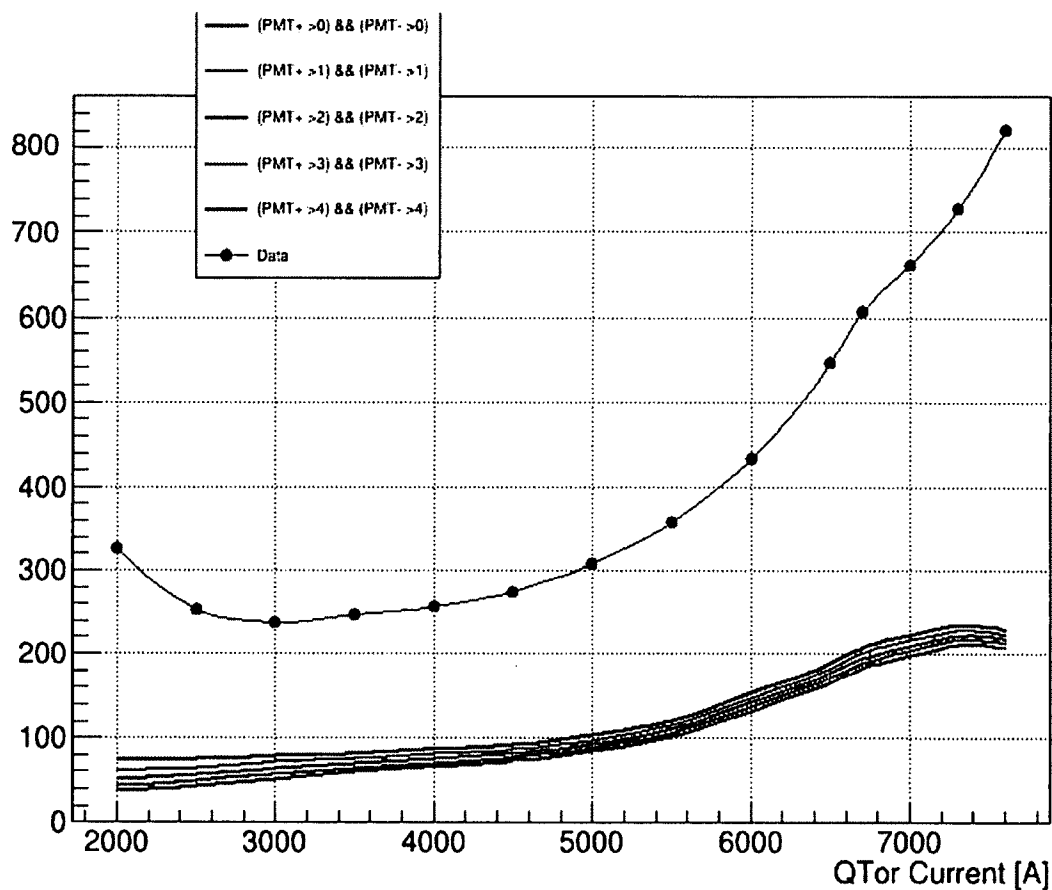


Figure 3.15: Testing the cut of the photoelectrons from greater than 0 to greater than 4 on rate (in kHz/uA), the simulation is lower than the data because there was a normalization problem between the data and simulation in the early part of this study. The normalization was corrected later in the study.

3.7 Yield

The yield is the total number of electrons that are obtained after the electron beam hits the target. Unlike rate, yield is weighted by the total number of photoelectrons. The yield hardware implementation is that the PMT (Section 3.1.5) detects a Čerenkov

photon from either the plus or minus sides. Basically it is equal to the rate multiplied by the photoelectrons. It is calculated via Equation 3.9:

$$\mathcal{Y} = \mathcal{L} \frac{d\sigma}{d\phi d\cos\theta dE'} \epsilon(\phi, \cos\theta, E') \mathcal{P}(\phi, \cos\theta, E'), \quad (3.9)$$

where \mathcal{Y} is the scattering yield in the detector, σ is the cross section, θ is the effective solid angle of the detector, \mathcal{L} is the luminosity, E is the energy range over the detector acceptance, and \mathcal{P} is the distribution photoelectrons [7].

The yields that are extracted from the physical experiment are in arbitrary units, therefore the simulation yields have to be normalized to match them. The simulation yield was normalized by 1 million in Figure 3.16, however, it was not close to the data.

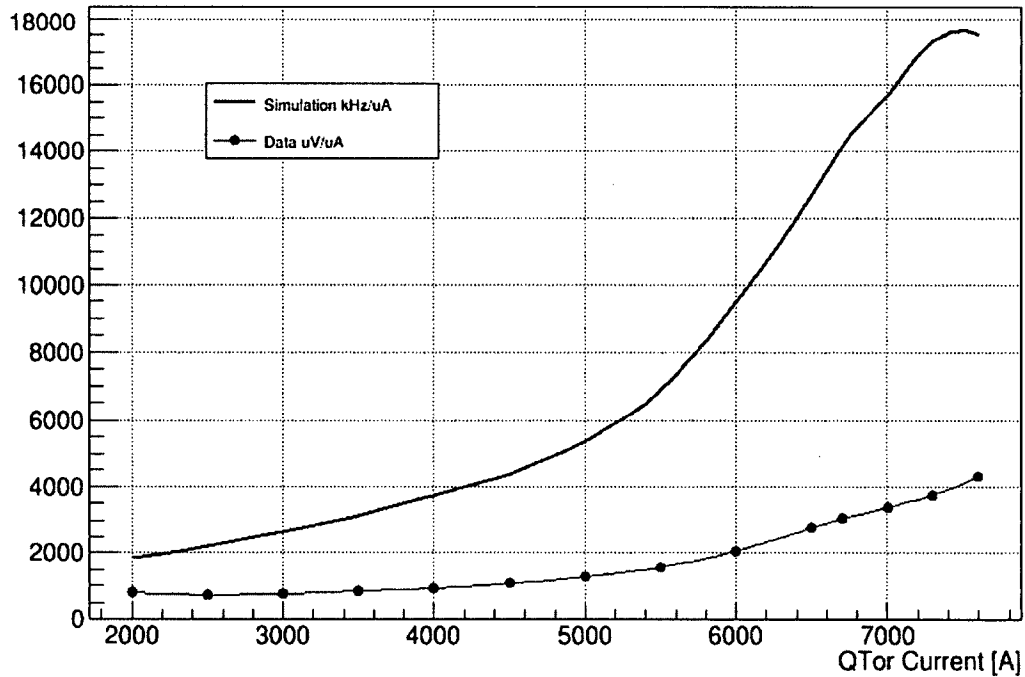


Figure 3.16: Physical experiment yield is normalized by 1 million in attempt to match the data since the physical data yield is in arbitrary units, however it didn't match it. Later both the experiment and simulation data were normalized at one point to match each other.

Figures 3.17 and 3.18 compare weighting with total number of photoelectrons and with left and right photoelectrons. It was concluded that weighting by total the number of photoelectrons is the one we needed. The experimental and simulated yields have been normalized to match for $Q_{\text{Tor}} = 8000$ A. To calculate its error Equation 3.8 is used. After the yield is averaged, it gets normalized to match the data at the Δ peak, $Q_{\text{Tor}} = 6700$ A.

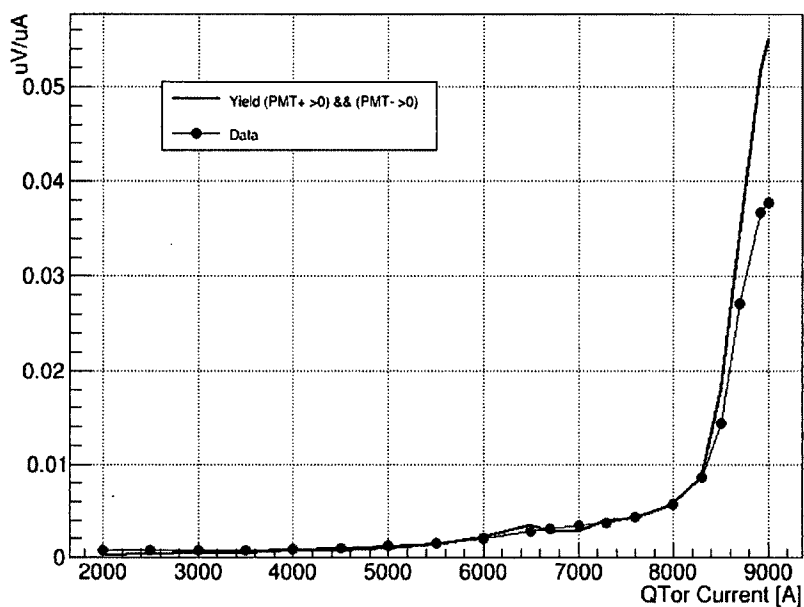


Figure 3.17: The simulation yield is weighted by left and right PEs > 0 .

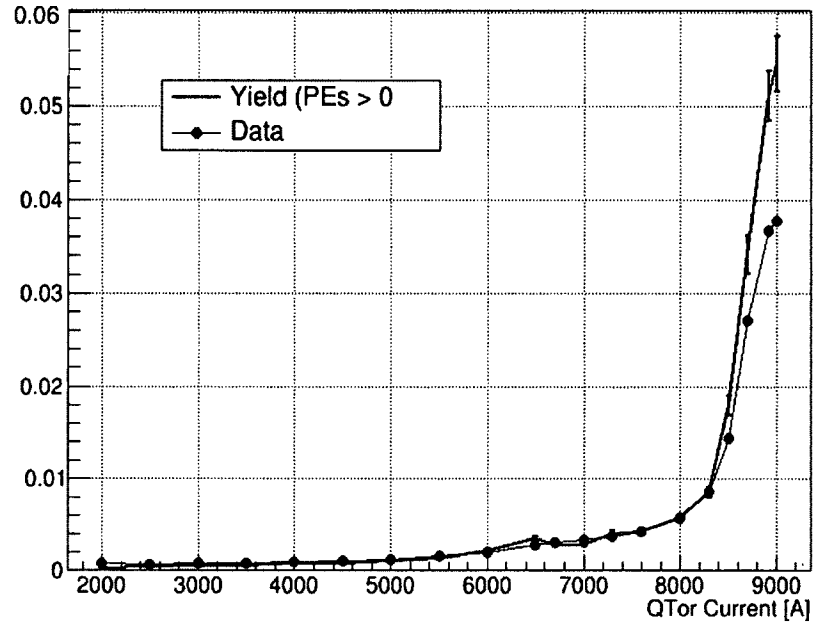


Figure 3.18: The simulation yield is weighted by total PEs > 0.

3.8 One Detector Simulation

The first half of this work was limited to one detector to make the testing faster. Detector 7 was chosen for this part of the study. Therefore, for all the testing and gaining experience, octant 7 was used. In Section 3.9, all 8 octants were introduced. All simulations have been performed for two beam energies: 1.16 GeV and 0.877 GeV.

3.8.1 1.16 GeV

At the beginning the simulation was performed using only event generator 7, Section 3.4.1. Generator 7 includes the radiated process, elastic, and inelastic events. To make it clear, elastic and inelastic event distributions over the detector are shown in Figure 3.19[6]. Elastic events correspond to the lower inside rectangle which represents the profile of the detector.

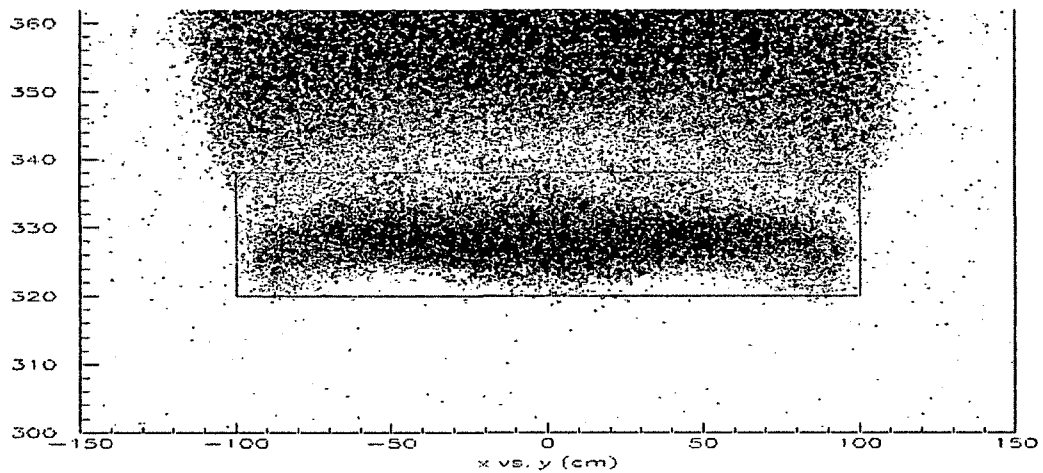


Figure 3.19: Elastic (the blue "lower" part) vs inelastic (the red "upper" part) events in the detector.

Later event generator 1, Section 3.5, was added to the simulation. Figure 3.20 shows the relationship between event generators 1 and 7 at the delta peak, $Q_{Tor} = 6700$ A. In this Figure both simulations were not performed for all Q_{Tor} currents. That was due to event generator 7 didn't work well near the elastic peak. Event generator 1 produces elastic events, as does the generator 7 elastic peak. Therefore, these two event types were compared in Figure 3.21. Event generator 1 was used with an energy cut to fix the event generator 7 elastic peak problem. It is clear that elastic peak from generator 7 is too high and needs to be edited.

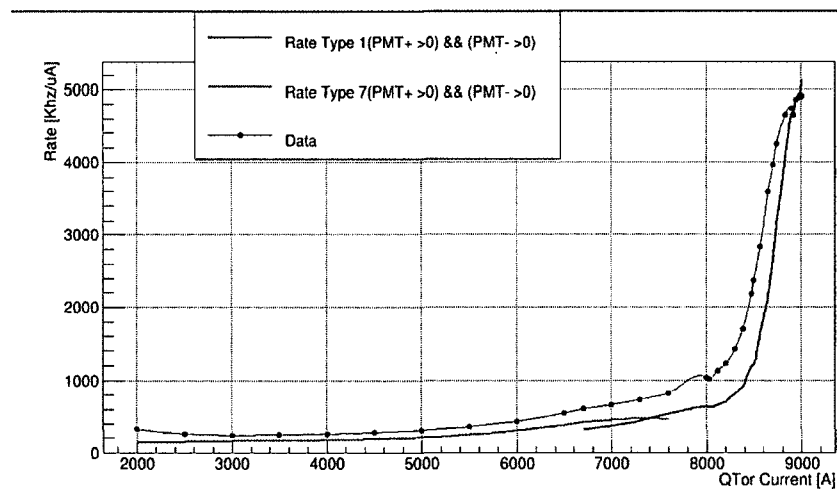


Figure 3.20: Variation of rate (in kHz/uA) as a function of Q_{Tor} current (A) from generator 1 and generator 7 simulations, compared with data.

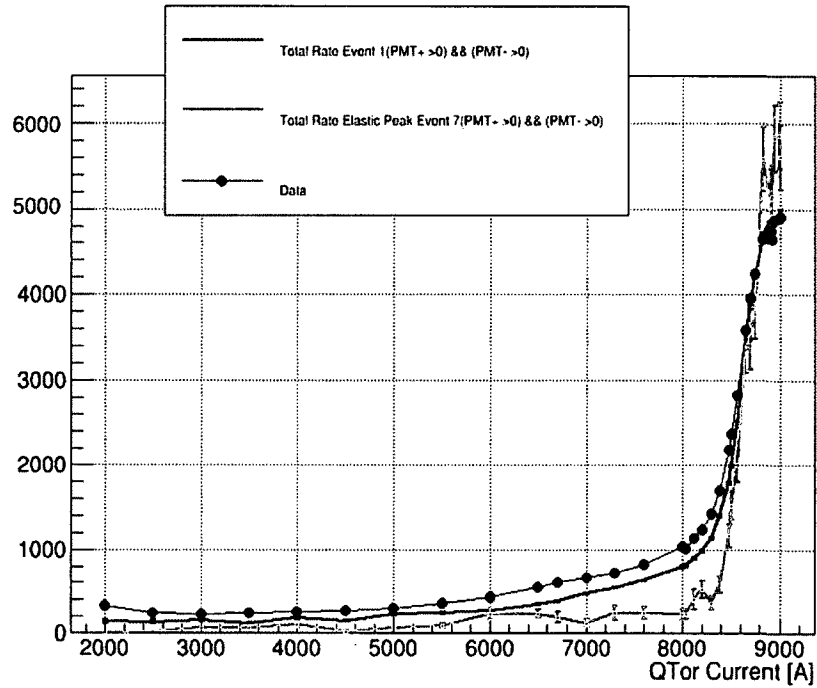


Figure 3.21: Variation of rate (in kHz/uA) as a function of QTor current (A) from event 1 Rate vs event 7 elastic peak simulations, compared with data.

Figure 3.22 shows that simulation total rate is higher than the experimental rate. Therefore, multiple event generators were compared with each other. Event generator 5 (Section 3.5.2), was added to the simulation. Its results were added to event generator 1. Figure 3.22 and Figure 3.23 show that simulation rate and yield respectively.

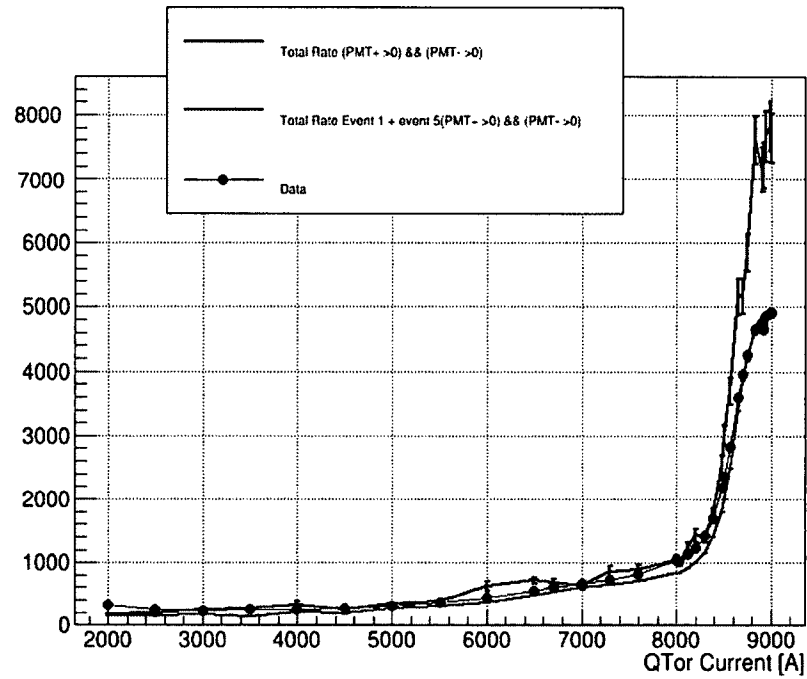


Figure 3.22: Variation of rate (in kHz/uA) as a function of QTor current (A) from generator 1 without Schwinger correction, generator 5, and generator 7 total simulations, compared with data.

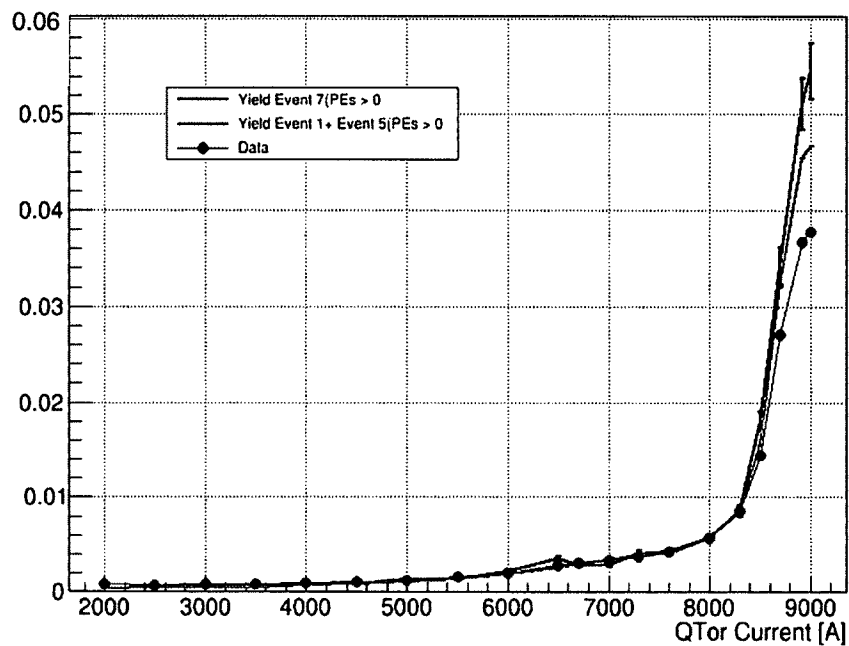


Figure 3.23: Variation of yield as a function of QTor current (A) from event 1 Rate vs event 7 yield simulations, compared with data.

The rate plot shows that generator 1 and 5 approximately match the data, whereas event generator 7 is much higher than the data. Event generator 7 data contains the Δ peak, which means that it is an important part of the simulation and cannot be replaced.

Dilution factors, which are the same as inelastic fraction (Section 3.10.1) near the Δ peak were extracted from Figure 3.23 and are shown in Table 3.1. The purpose of the dilution factor is to compare the Geant4 simulation with its old version Geant 3. Geant 3 and Geant 4 results are almost the same which suggests that this simulation is going in the right direction.

Table 3.1: Dilution factor around delta peak for Geant3 and Geant4

QTor	Dilution factor E7	error df	Dilution Factor E(1+5)	error df	Dilution Factor G3	error df
6000	0.78772723	0.011844537	0.73482721	0.00855707	0.754758212	0.003707161
6500	0.753033438	0.01273325	0.666455803	0.009040178	0.704982678	0.003693066
6700	0.776163881	0.01195666	0.702516397	0.007980869	0.721098887	0.003379102
7000	0.820226077	0.011307943	0.736711902	0.006403923	0.7621193	0.002825841
7300	0.873964749	0.008812918	0.80950975	0.004846763	0.824766982	0.002054539
7600	0.937904244	0.007915564	0.884284867	0.002988025	0.890378676	0.001327144

Additionally, one of the ways to compare the simulation to the data is to calculate the relative residual. It is calculated by Equation 3.10. Figures 3.24 and 3.25 represent the yield and rate relative residuals for event generator 7. The data and simulation mostly disagree with each other around the elastic peak. In Figures 3.26 and 3.27 it is the relative residual for yield and rate respectively, for event 1 and event 5.

$$\text{Relative Residual} = \frac{\text{Simulation} - \text{Data}}{\text{Data}} \quad (3.10)$$

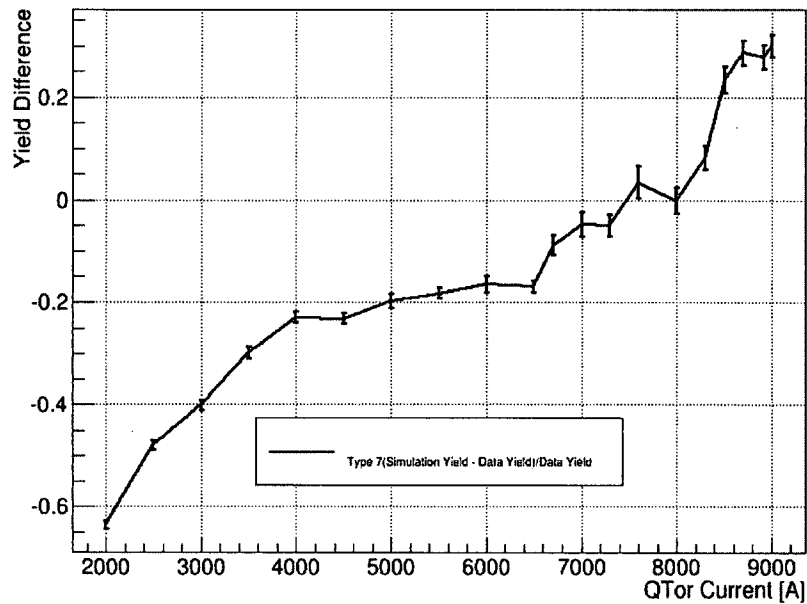


Figure 3.24: Event generator 7 yield relative residual.

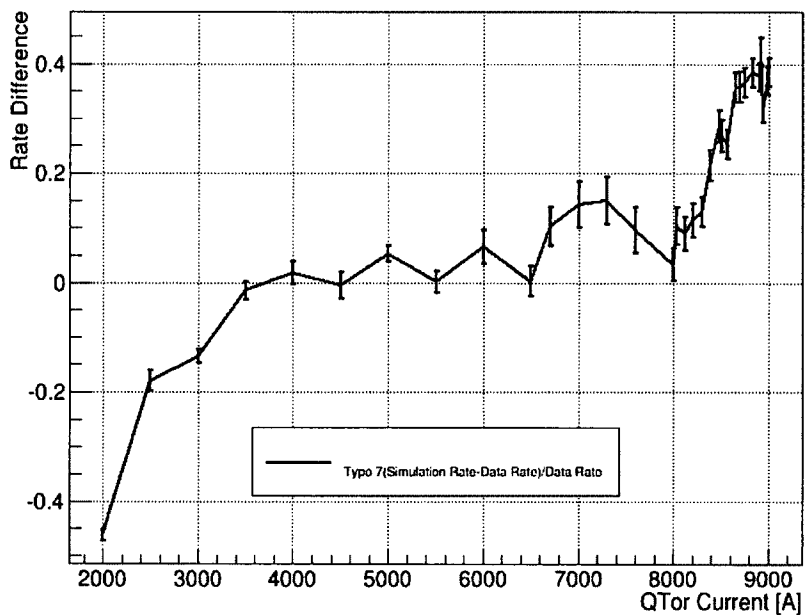


Figure 3.25: Event generator 7 rate relative residual.

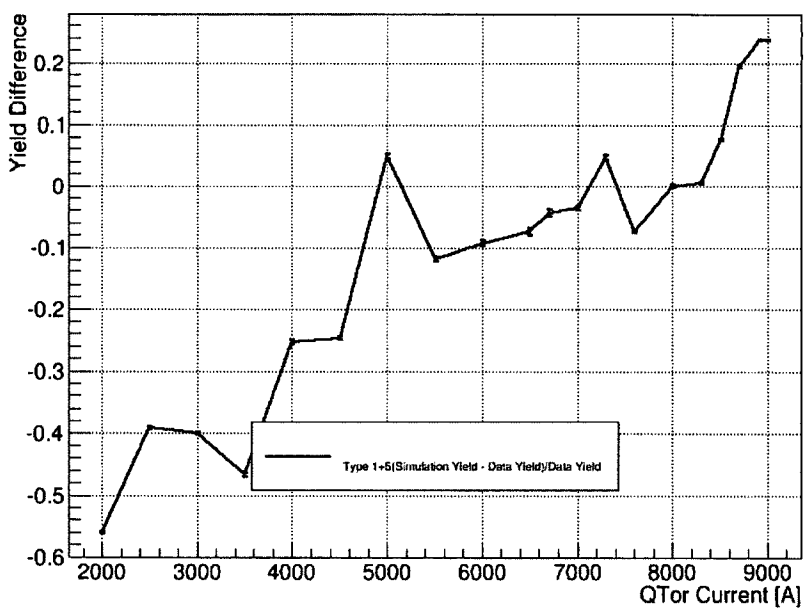


Figure 3.26: Event generators 1 and 5 yield relative residual.

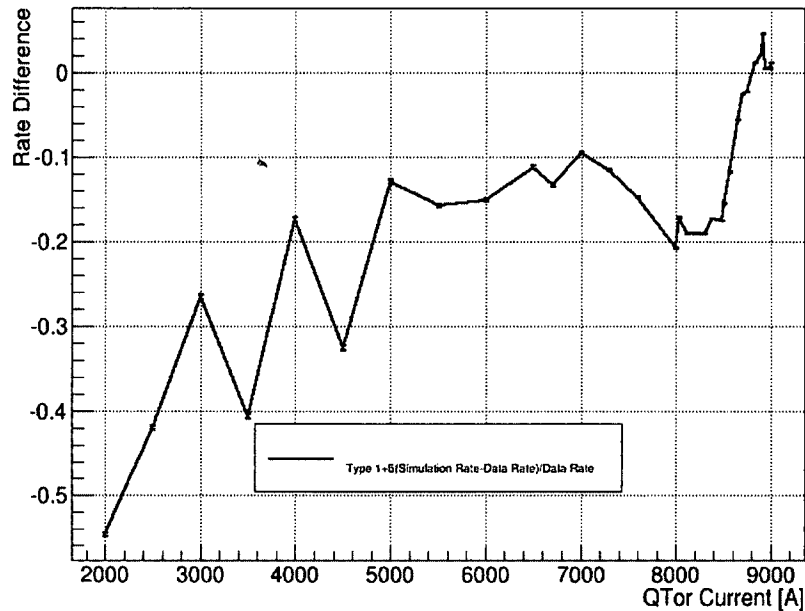


Figure 3.27: Event generators 1 and 5 rate relative residual.

Event generator 7 is important due to its inelastic events that are not contained in any other event generator. Also, event generator 1 is equally important. That is due to event generator 7 is designed for radiative and inelastic events, however it is not accurate at predicting the elastic events. Therefore, in the simulation we combined event generator 1 with 7. A solution was needed to make the best in both event generators. Event generator 5 was soon eliminated from this study because event generator 7 has most of its characteristics, and event generator 5 has no radiative effects included. As for event generator 7, the elastic peak part was replaced with a built in function that is valid near the elastic region up to 15 MeV below the elastic peak. Finally with the most impact, event generator 1 was modified and a radiative correction was added to it. The details can be found in the Schwinger correction (Section 3.5.1). There were two formulas to add the radiative correction: Mo and Tsai formula[1] or Lightbody and O'Connel formula[16]. Both formulas were tested and plotted in Figures 3.28 and 3.29. The Figures conclude that the Mo and Tsai formula results in an approximately 15% correction to the radiated events, while the

Lightbody and O'Connel formula only added a small correction. Therefore, the Mo and Tsai formula was chosen to be added to event generator 1.

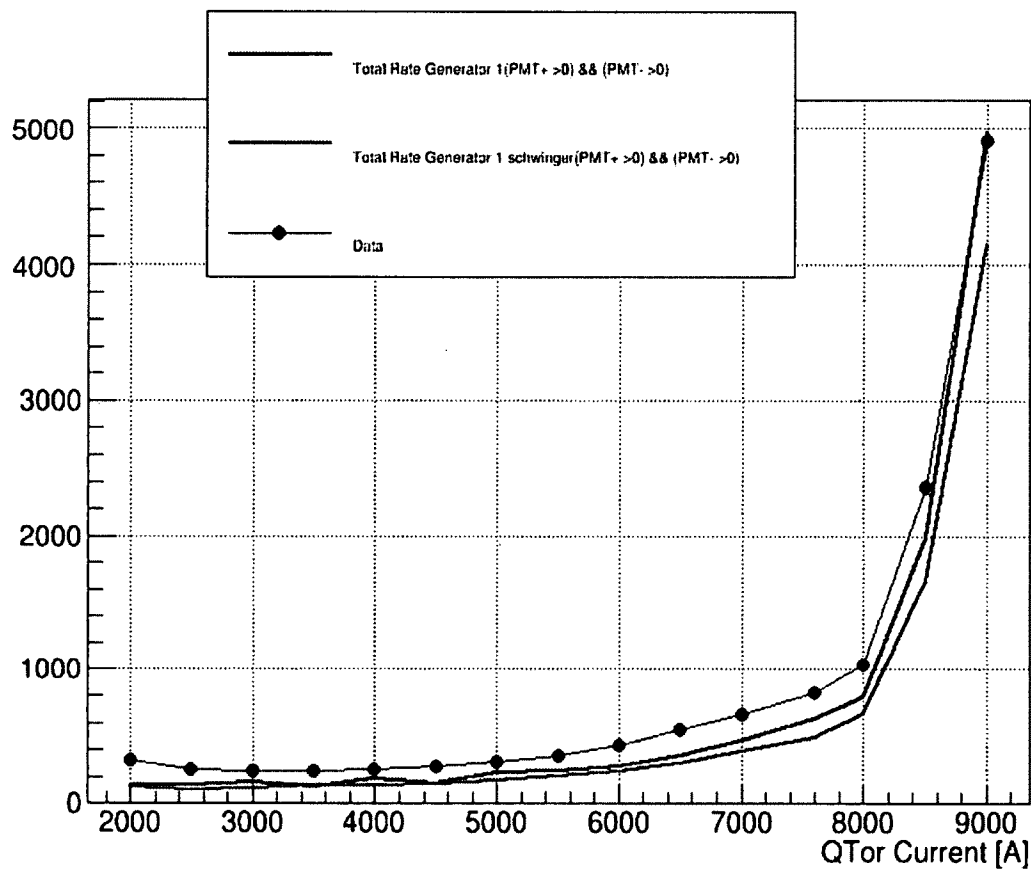


Figure 3.28: Variation of rate (in kHz/uA) as a function of QTor current (A) from generator 1 with and without the Schwinger correction using the Mo and Tsai formalism simulations, compared with data.

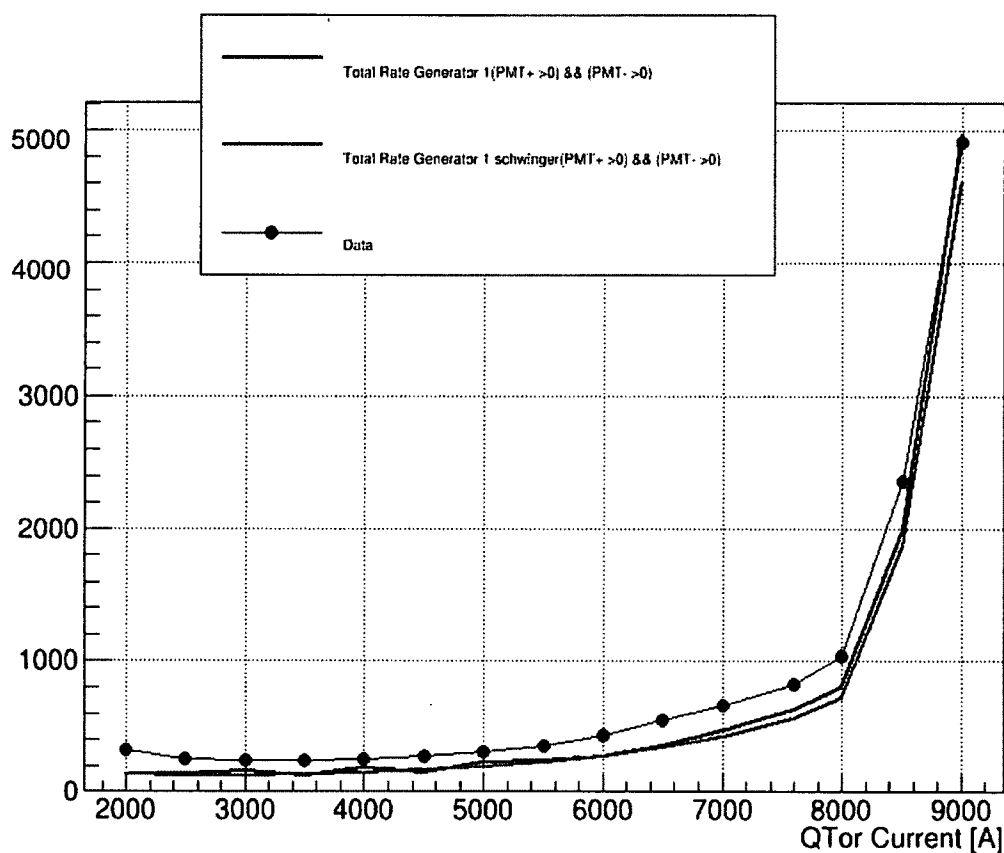


Figure 3.29: Variation of rate (in kHz/uA) as a function of QTor current (A) from generator 1 with and without the Schwinger correction using the Lightbody and O'Connel formalism simulations, compared with data.

More tests were done on event generator 1 that suggested that a cut on the energy is needed. It was proposed that only events generated by higher energy will be used in the simulation. Figure 3.30 represents E prime "Vertex Energy" and Theta "Vertex Theta" and all the events that are generated with only a cut on the left and right photoelectrons. Then, Figure 3.31 shows the events when the difference between the elastic scattered energy and total energy is less than 15 MeV. From the last plot it was concluded that a 15 MeV window is wide enough to include all of the elastic peak events in generator 1 with the Schwinger correction.

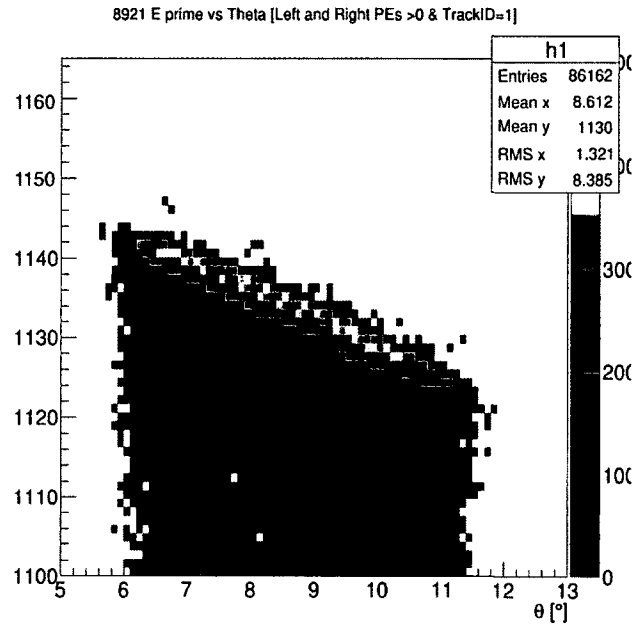


Figure 3.30: The correlation between vertex energy and theta with cut on left and right PEs >0.

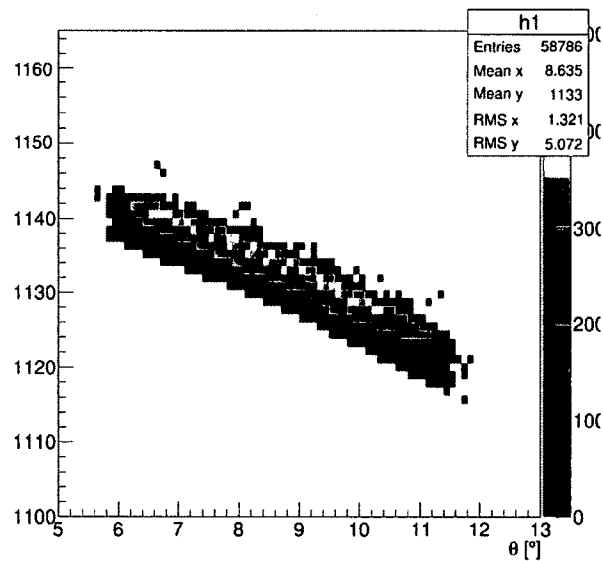


Figure 3.31: The correlation between local vertex energy and global theta with cut on left and right PEs >0 and elastic energy < 15 MeV.

The final version of event generator 1 is that it contains a radiative correction formula and its rate and yield are cut on by energy in addition to the number of PEs. The rate for event generator 1 and 7 elastic and Δ production compared to the data is

shown in Figure 3.32. In addition, Figure 3.33 shows a comparison between the yield data and simulation for the modified event generator 1 and elastic and deep inelastic event generator 7. Relative residuals are important to show the difference between data and simulation results. Figures 3.34 and 3.35 represent the relative residual for rate and yield, respectively. Relative residual is calculated by Equation 3.10.

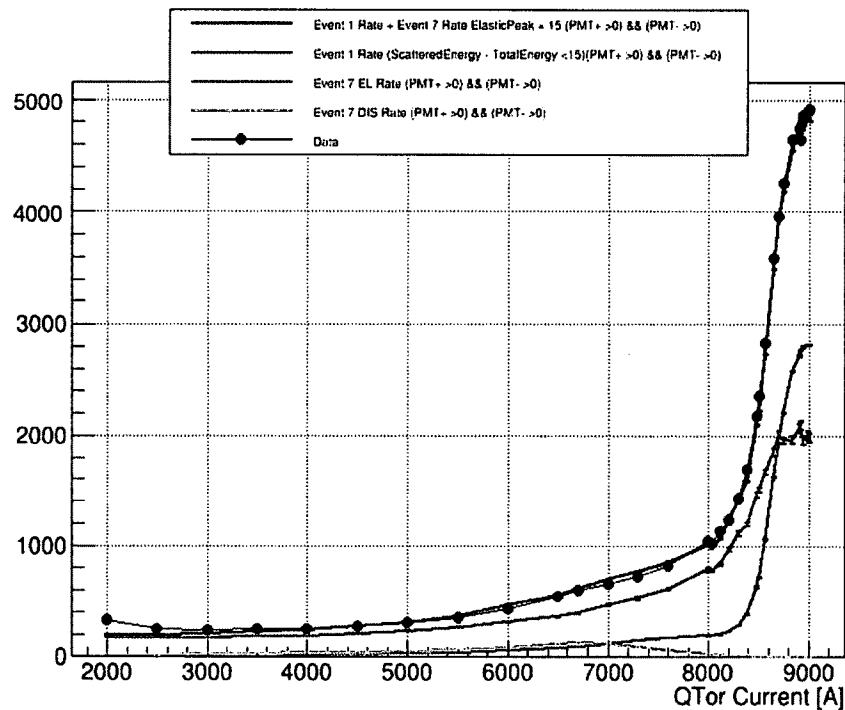


Figure 3.32: Variation of rate (in kHz/uA) as a function of QTor current (A) from generator 1 rate with the cut on elastic energy < 15 MeV, generator 7 EL and DIS simulations, compared with data.

Simulation Yield Normalized at 8921 A to match data

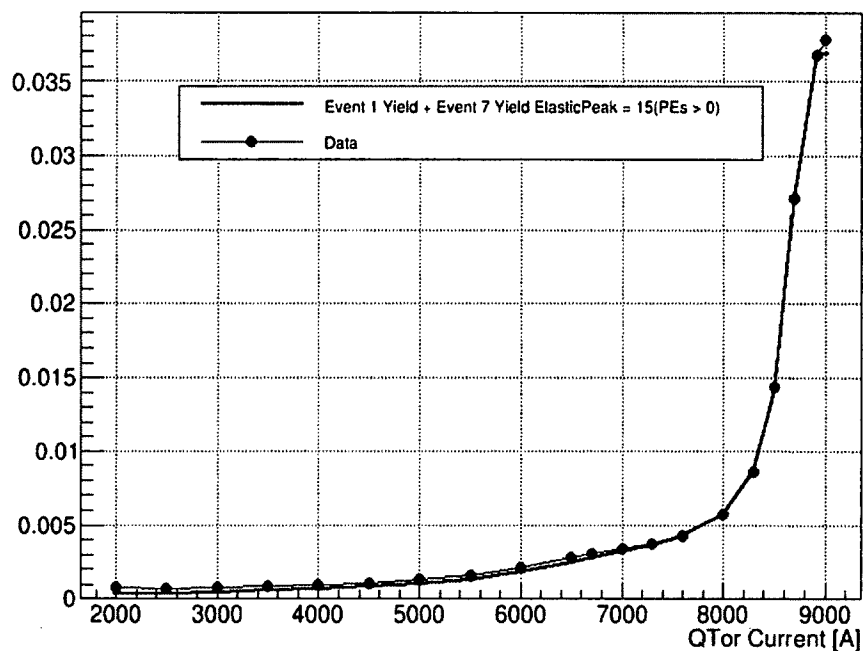


Figure 3.33: Variation of yield as a function of QTor current (A) from generator 1 rate with the cut on elastic energy < 15 MeV, generator 7 EL and DIS simulations, compared with data.

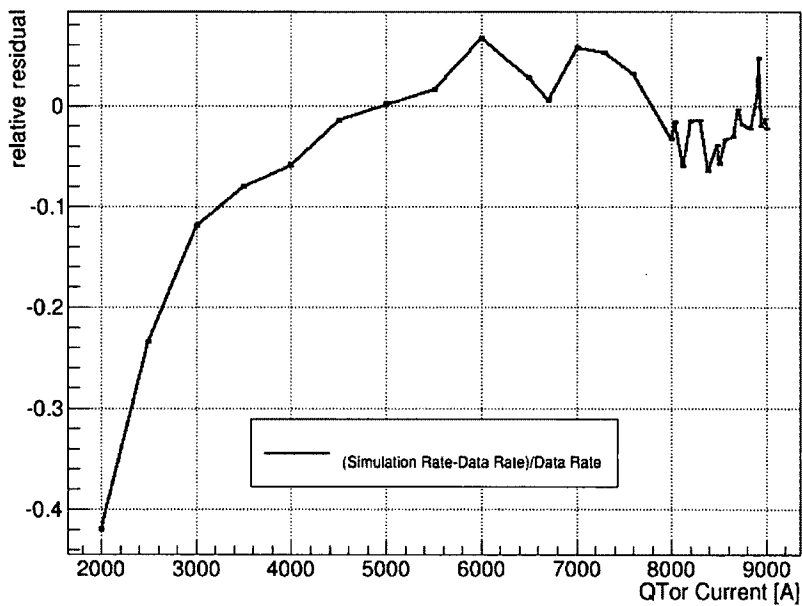


Figure 3.34: Rate relative residual.

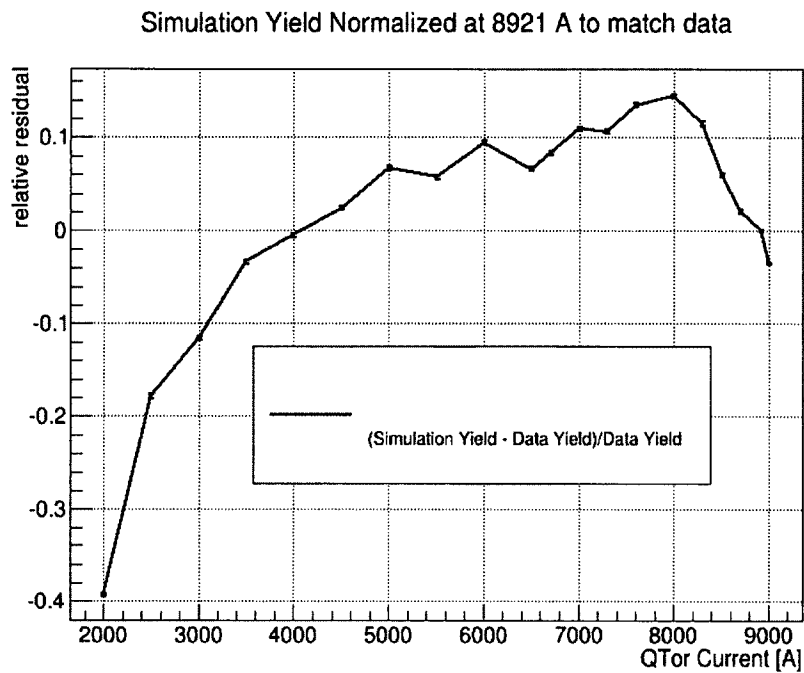


Figure 3.35: Yield relative residual.

The aluminum end caps were then included. These caps are part of the hydrogen target in the physical experiment (for more information review Section 3.5.3). Aluminum end caps are added to the simulation by event generator 2. It has little impact on the overall results, but we include those events in simulation because they are known to be present in the rate and yield in the physical experiment.

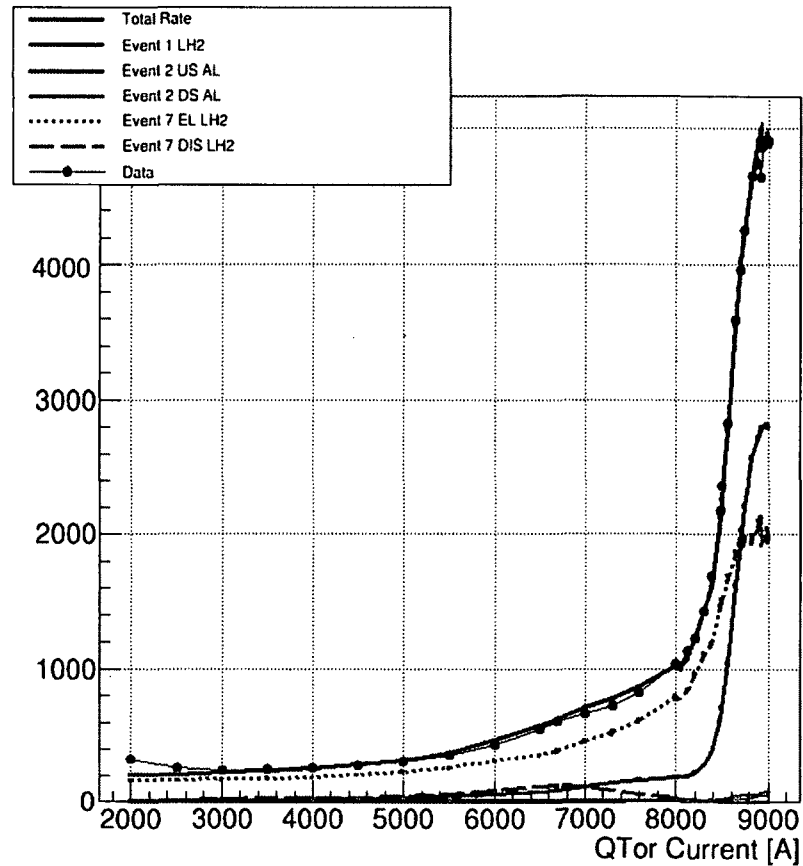


Figure 3.36: Variation of rate (in kHz/uA) as a function of QTor current (A) from generator 1 rate with the cut on elastic energy < 15 MeV, generator 2, generator 7 EL and DIS simulations, compared with data.

The total rate that includes all three event generators is shown in Figure 3.36. Since the aluminum end caps curves are small, Figure 3.37 shows the rate but on a log scale to make the aluminum curves clear.

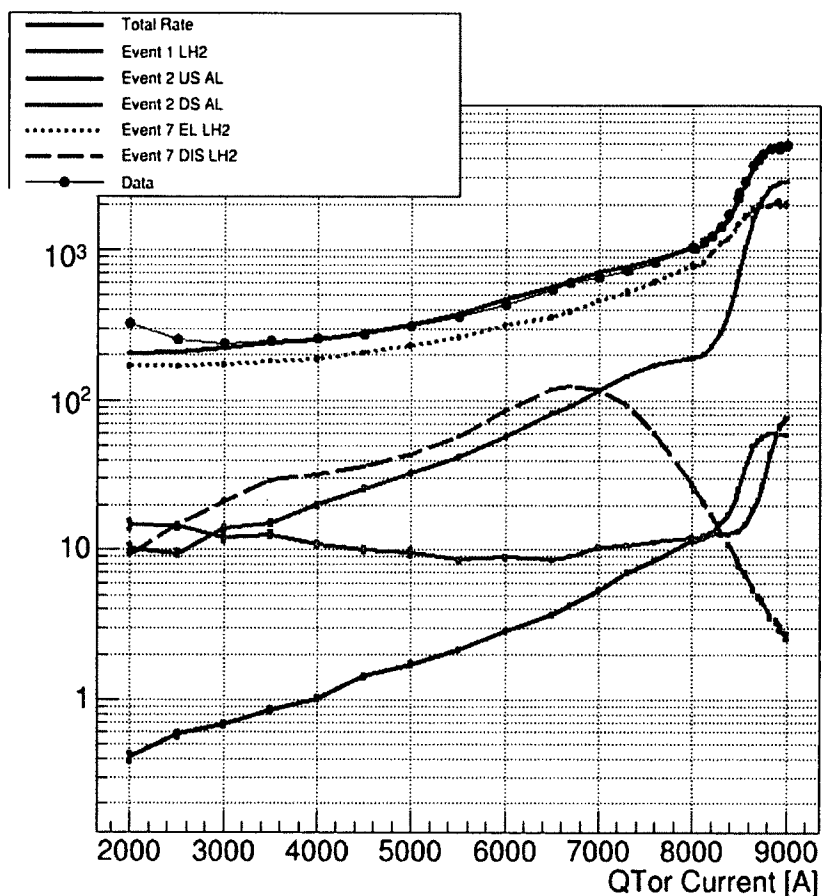


Figure 3.37: Variation of rate (in kHz/uA) as a function of QTor current (A) from generator 1 rate with the cut on elastic energy < 15 MeV, generator 2, generator 7 EL and DIS simulations, compared with data. The low QTor discrepancy is due to the Möller scattered electrons. This study didn't include a Möller generator.

The total yields including the hydrogen target and aluminum end caps are presented in Figure 3.38. Total simulation yield is normalized to match the experimental data at the elastic peak, $Q_{\text{Tor}} = 8921$ A. The Figure shows that the simulation yield curve is matching the shape of the data yield.

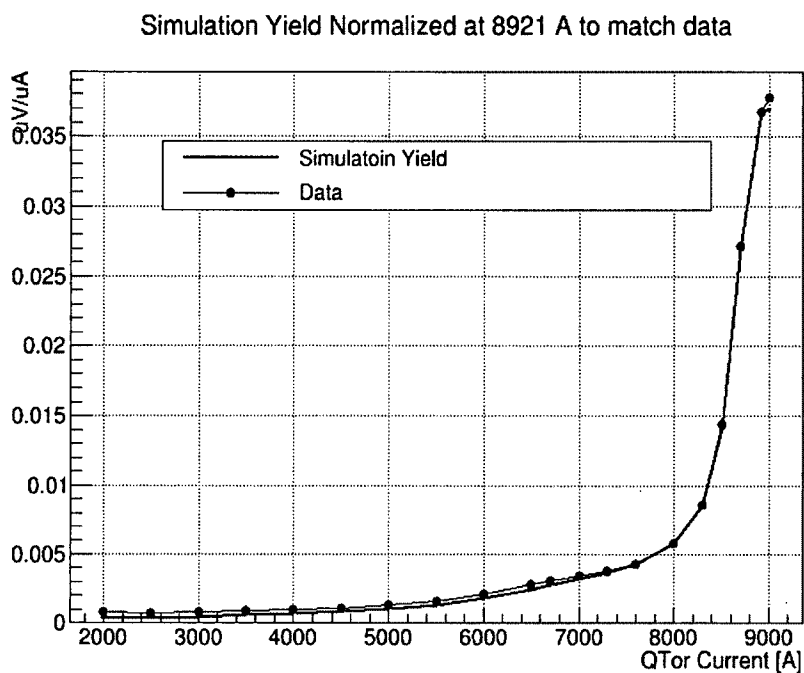


Figure 3.38: Variation of yield as a function of QTor current (A) from generator 1 rate with the cut on elastic energy <15 MeV, generator 2, generator 7 EL and DIS simulations, compared with data.

Figures 3.39 and 3.40 represent the relative residual for rate and yield, respectively. Relative residual is calculated by Equation 3.10. Those two Figures help understand the relationship between the physical experimental data and the simulation data. As shown, the physical experimental data and the simulation data almost match. That means that the simulation is performing well.

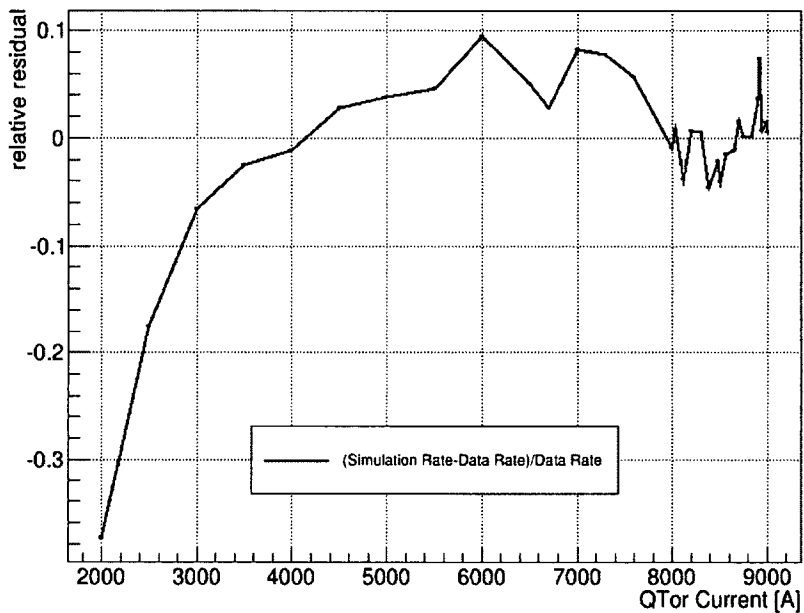


Figure 3.39: Rate relative residual.

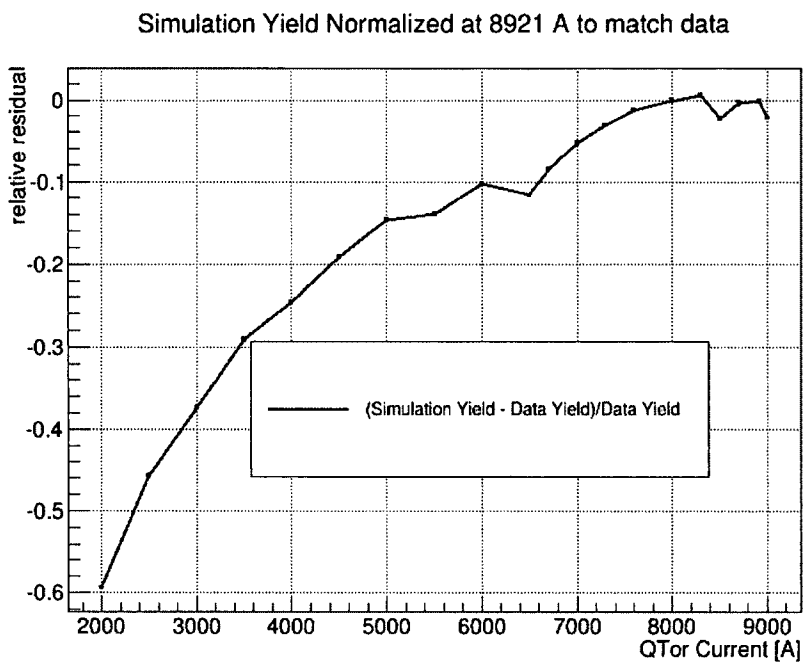


Figure 3.40: Yield relative residual.

Since the elastic peak QTor current point is an important point, it gets tested to measure the agreement between the simulation and physical data. As shown in

Figure 3.41, simulation and data at octant 7 are almost equal. That is more evidence that the code of the simulation is accurate.

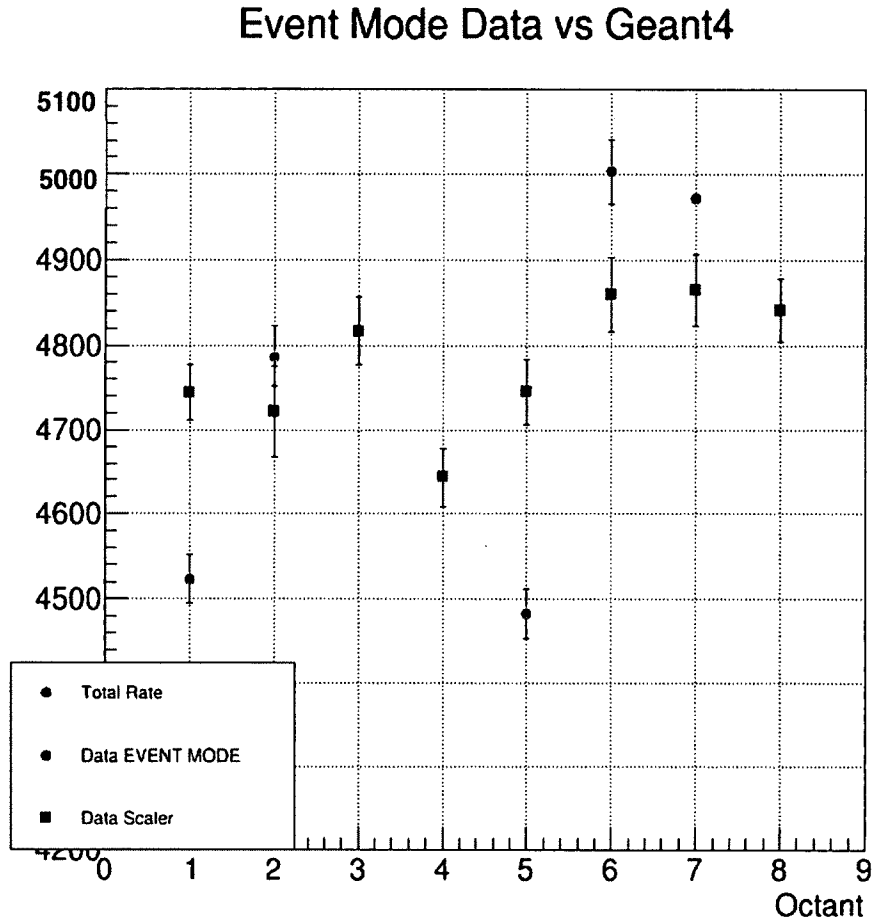


Figure 3.41: Rate (in kHz/uA) at 8921 A in data and simulation.

Finally, the dilution factor was calculated as the last step to check the accuracy of the Geant4 simulations. The elastic dilution factor near the Δ peak is presented by Figure 3.42 and calculated by this Equation

$$f = \frac{Y_{el}}{Y_{tot}}, \quad (3.11)$$

where f is the elastic fraction, Y_{el} is the elastic yield from event generators 1 and 7, and Y_{tot} is the total yield.

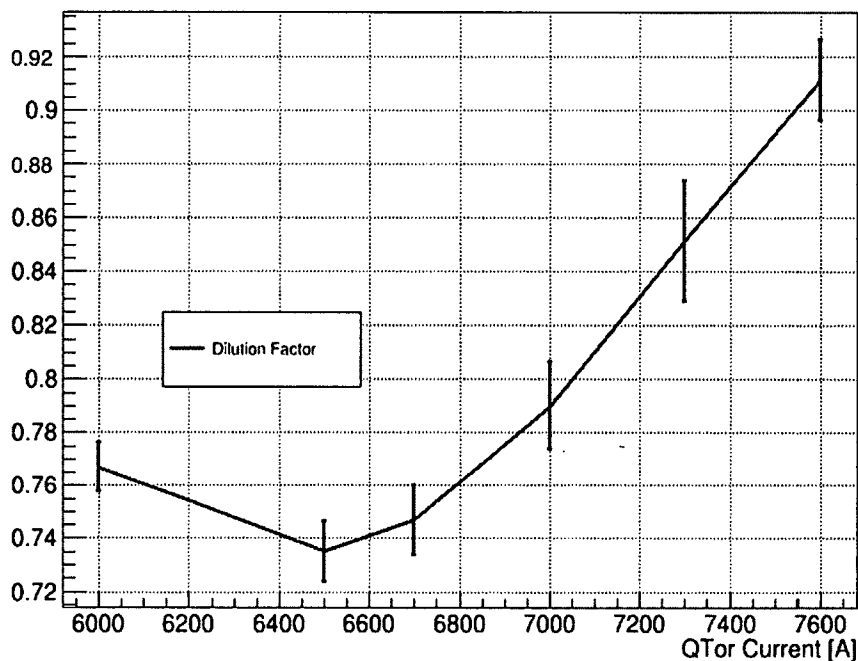


Figure 3.42: Yield dilution factor around the Δ peak.

The last step to complete the simulation is to add the pions. A full description of pions is in Section 3.5.4. Pions were added in three reaction regions: hydrogen, upstream aluminum, and downstream aluminum. Pions have a very small affect on the simulation, however, it is added to make the simulation complete and comparable to the data. Moreover, at this point event generator 2 in both rate and yield is weighted the same way as event generator 1, which is by photoelectrons greater than zero and that it has to be cut at 15 MeV below the elastic peak.

Figure 3.43 shows the total simulation including all the effects. All the processes are included in this Figure. The physical experimental data and the total simulation rate match with no normalization. This leads us to calculate the rate for all the octants.

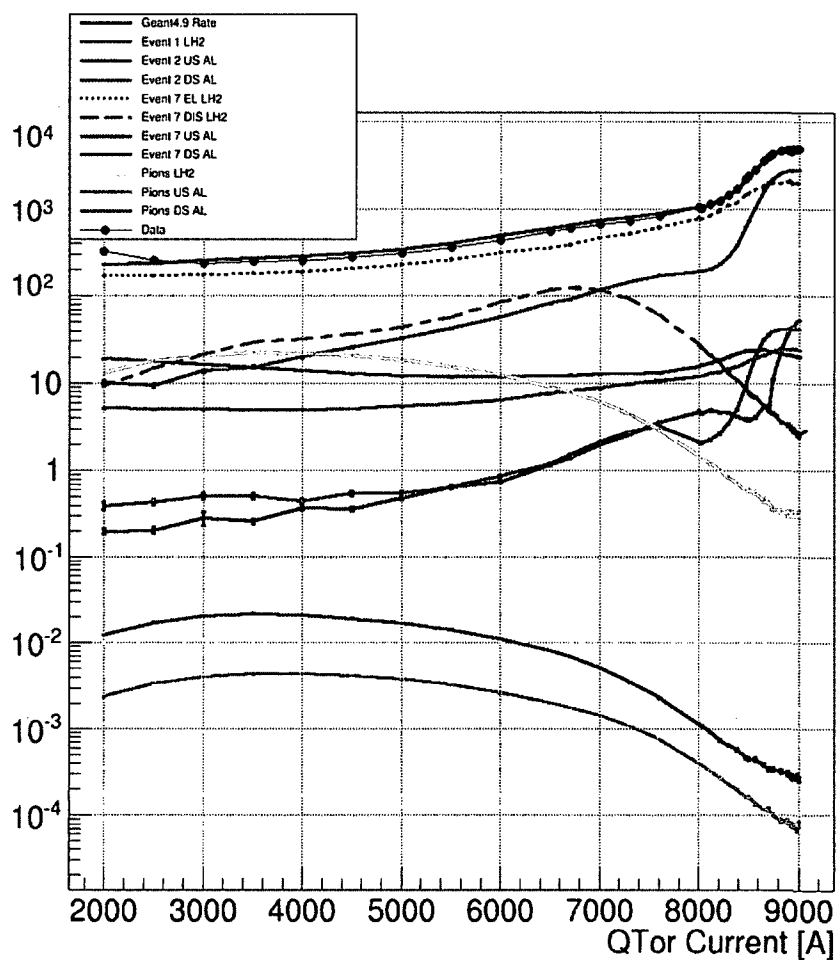


Figure 3.43: Variation of rate (in kHz/uA) as a function of QTor current (A) from simulations, compared with data

Figure 3.44 shows the total yield after including all the processes. Total yield is normalized at the elastic peak, $Q_{\text{Tor}} = 8921$ A, to match the data. The curves match. Therefore, the yield extraction needs to go to the next level, which is for all the octants.

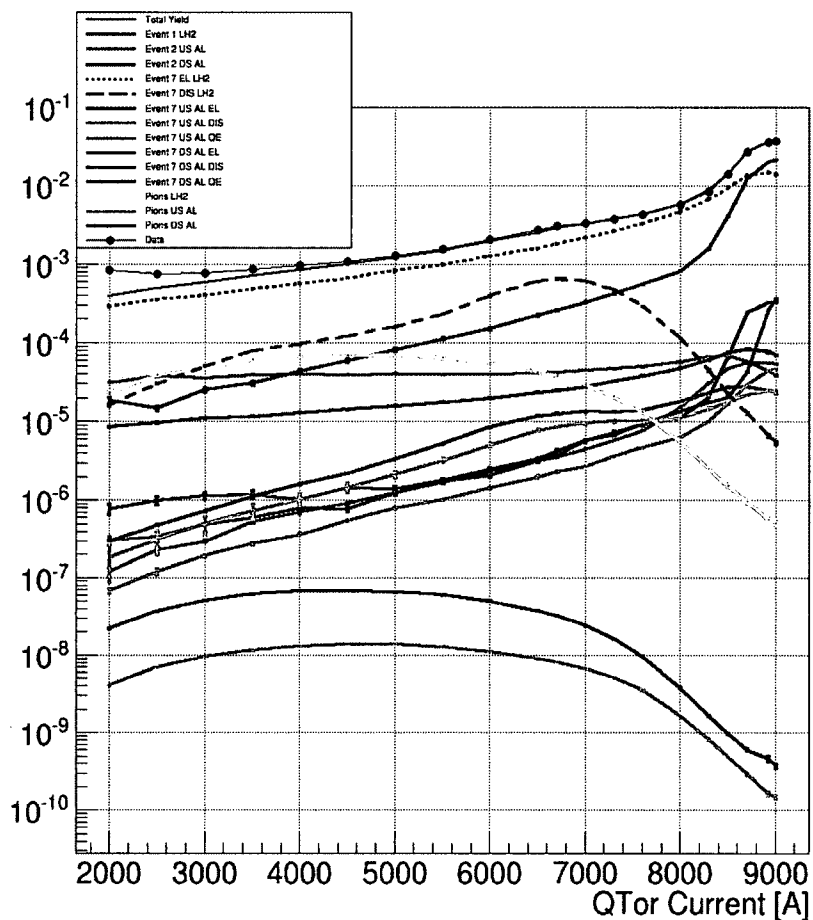


Figure 3.44: Variation of yield as a function of QTor current (A) from simulations, compared with data in log scale.

As stated before, relative residuals are needed to clarify the small differences between the physical experimental data and simulation data. Figures 3.45 and 3.46 represent the relative residual for rate and yield, respectively. Relative residual is calculated by Equation 3.10. Both Figures show that simulation data nearly matched the real data near the Δ peak and the elastic peak.

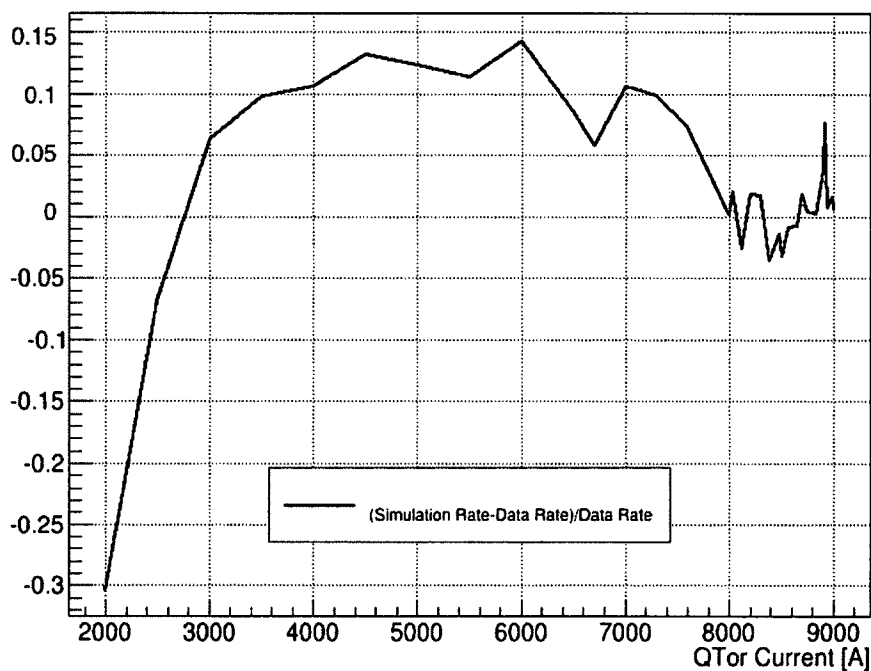


Figure 3.45: Rate relative residual.

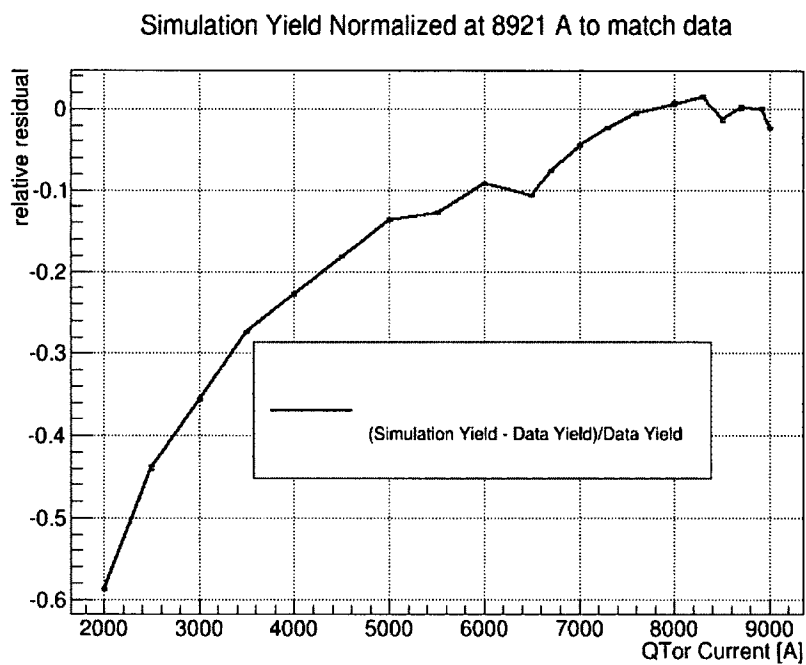


Figure 3.46: Yield relative residual.

Table 3.2 presents the dilution factors for the octant 7 simulation yield. The elastic dilution factor was calculated by Equation 3.11, while the dilution factor was

calculated by Equation 3.16. The fraction f_4 at $Q_{\text{tor}} = 6700 \text{ A}$ is the elastic dilution factor, while f_4 at $Q_{\text{tor}} = 8921 \text{ A}$ is the inelastic dilution factor. The fraction f_1 at $Q_{\text{tor}} = 6700 \text{ A}$ is the aluminum dilution factor at the Δ peak and f_1 at $Q_{\text{tor}} = 8921 \text{ A}$ is the aluminum dilution factor at the elastic peak. The fraction f_5 at $Q_{\text{tor}} = 6700 \text{ A}$ is the pion dilution factor at the Δ peak and f_5 at $Q_{\text{tor}} = 8921 \text{ A}$ is the pion dilution factor at the elastic peak. These dilution yield fractions are needed to extract the $N \rightarrow \Delta$ asymmetry. After the dilution factor was calculated, the one octant simulation was concluded.

Table 3.2: Aluminum, elastic, and pion fractions for elastic and Δ peaks.

Qtor	6700A	8921A
f_1	0.0358	0.023600
Error	0.00001	0.000004
f_4	0.7242	0.000200
Error	0.0026	0.000008
f_5	0.0110	0.00001700
Error	0.0007	0.00000124

3.8.2 0.877 GeV

The second beam energy is 0.877 GeV. Most of the testing and implementation was done for beam energy 1.16 GeV described in Section 3.8.1. Both beam energies share the same characteristics, therefore the same criteria that was applied to beam energy 1.16 GeV simulation will be applied to beam energy 0.877 GeV simulation. The purpose of this section is to confirm that the rate and yield from at least one octant will match the data for two different energies.

The rate (Section 3.6) was compared to the real experimental rate and plotted in Figure 3.47. Figure 3.48 shows the rate on a log scale to emphasize each process. There are two different techniques used in the physical experiment to measure the rate; scaler and TDC. Each technique gives a different rate. Therefore, the yield is

compared to the simulation. The simulation data is closer to the scaler data. It does not match the exact curves, but it is close.

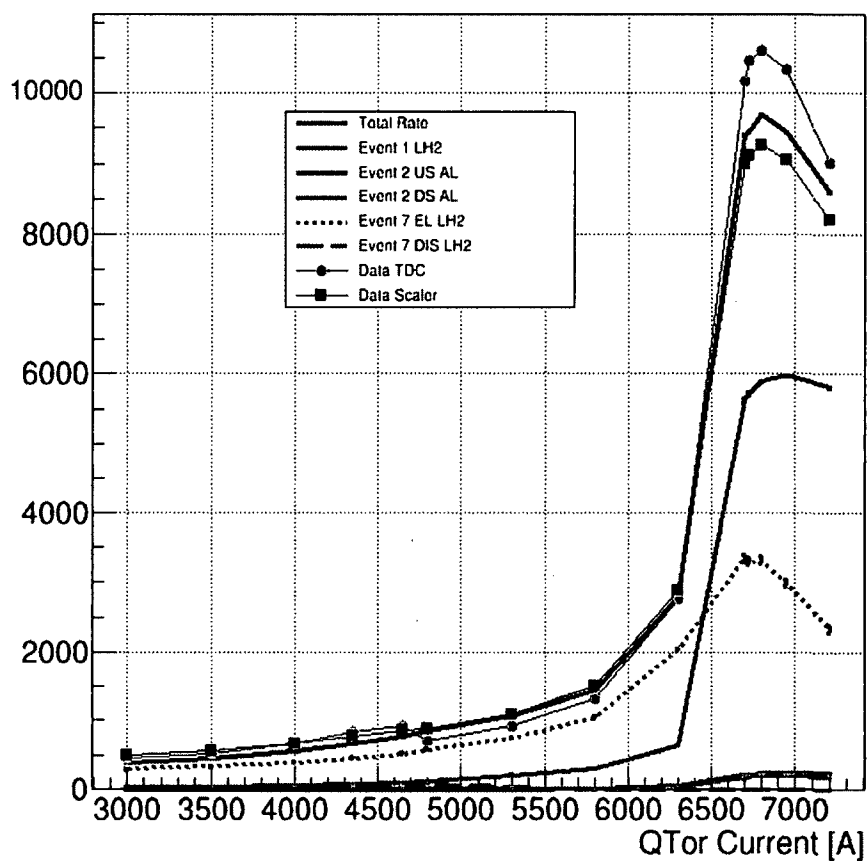


Figure 3.47: Variation of rate (in kHz/uA) as a function of QTor current (A) from simulations, compared with data.

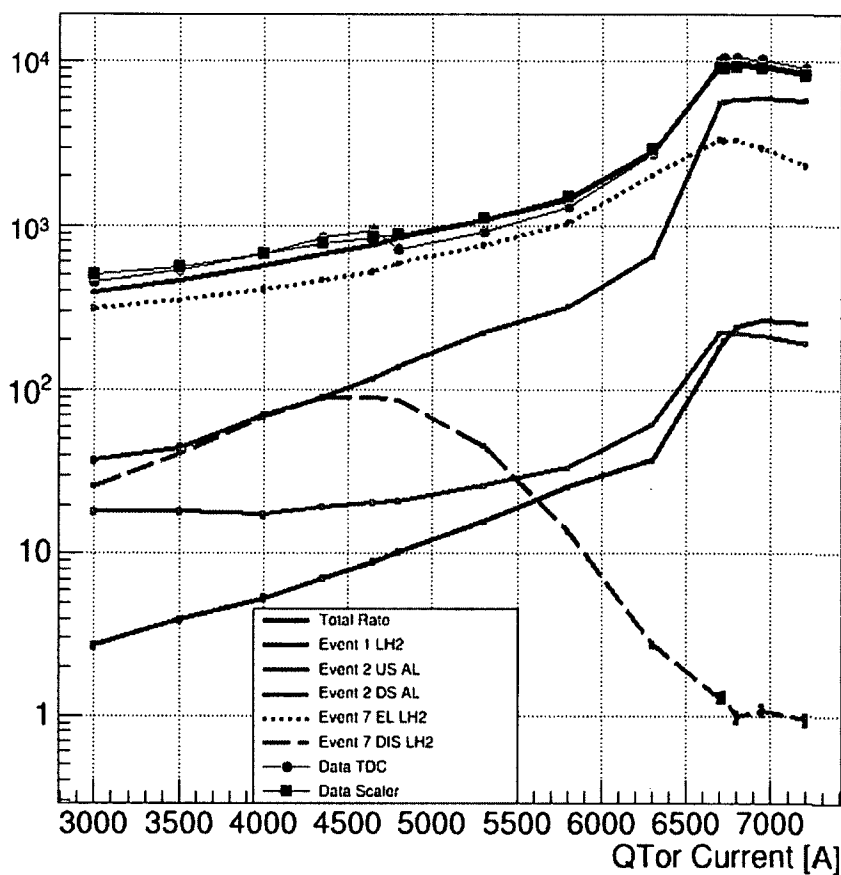


Figure 3.48: Variation of rate (in kHz/uA) as a function of QTor current (A) from simulations, compared with data in log-scale.

On the other hand, Figures 3.49 and 3.50 are for the yield. The elastic peak is at $Q_{\text{Tor}} = 6800$ A where the elastic yield is maximum at this energy. Therefore, the yield simulation is normalized at that point to match the data. The simulation yield matches the curve of the real data.

Simulation Yield Normalized at 6800 A to match data

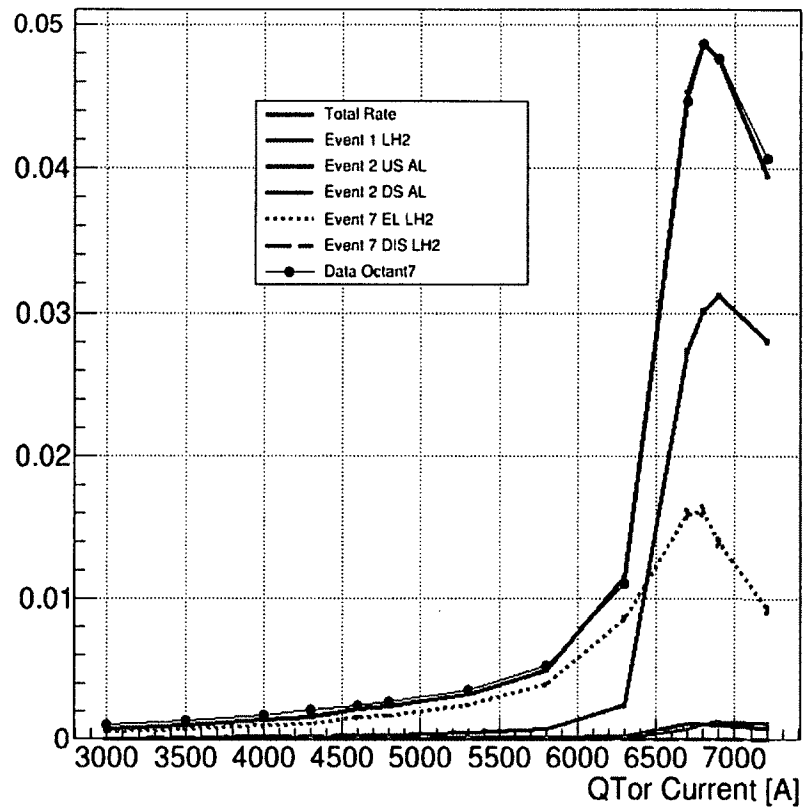


Figure 3.49: Variation of yield as a function of QTor current (A) from simulations, compared with data.

Simulation Yield Normalized at 6800 A to match data

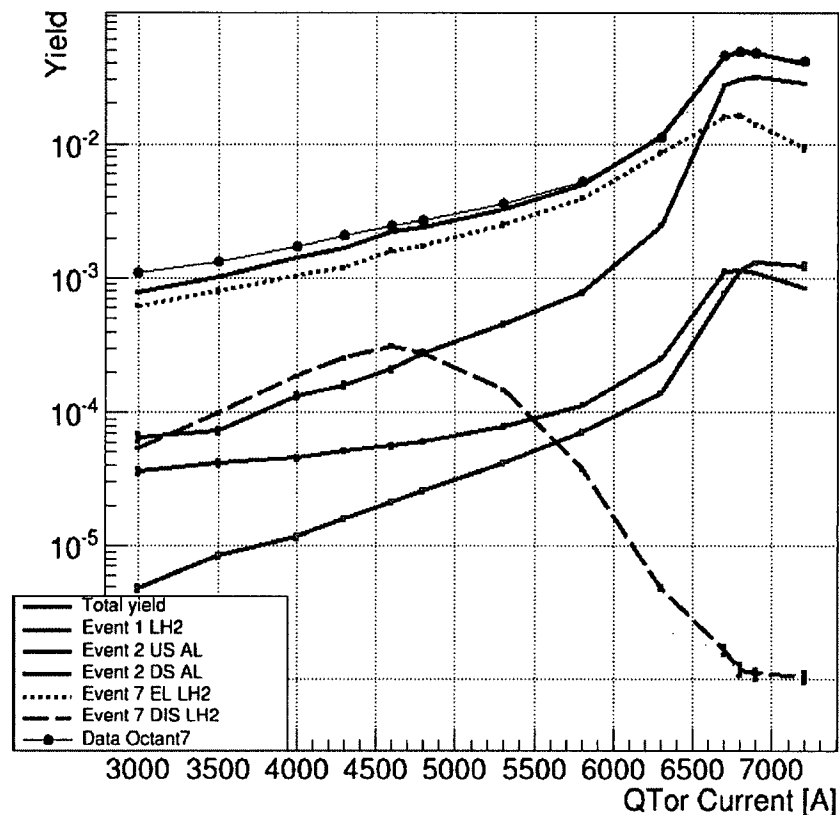


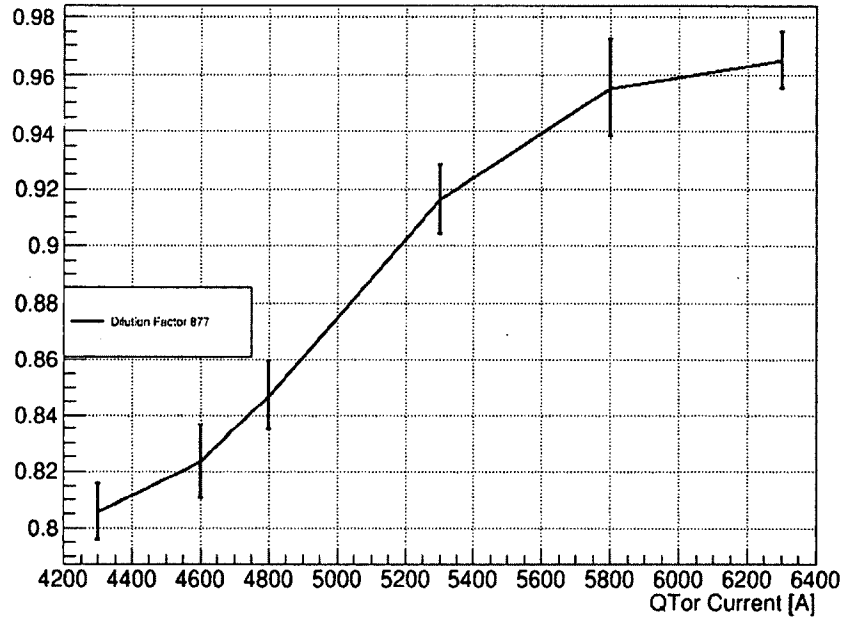
Figure 3.50: Variation of yield as a function of QTor current (A) from simulations, compared with data on a log scale.

Table 3.3 presents the dilution factors at the Δ peak for the octant 7 simulation yield. The elastic dilution factor was calculated by Equation 3.11, while the dilution factor was calculated by Equation 3.16. f_4 is the elastic dilution factor, f_1 is the aluminum dilution factor, and f_5 is the pion dilution factor. These dilution yield fractions are needed to extract the $N \rightarrow \Delta$ asymmetry at 0.877 GeV. After the dilution factors were calculated, the one octant simulation at 0.877 GeV was concluded.

To conclude the one octant beam energy 0.877 GeV simulation, the dilution factor was calculated. Figure 3.51 presents the yield dilution factor near the Δ peak. The dilution factor was calculated by Equation 3.16.

Table 3.3: Aluminum, elastic, and pion fractions at $Q_{\text{tor}} = 4650 \text{ A}$.

Q_{tor}	4650A
f_1	0.069
Error	0.001
f_4	0.790
Error	0.013
f_5	0.0097
Error	0.0001

Figure 3.51: Yield dilution factor near the Δ peak.

3.9 All Detector Simulation for 1.16 GeV

After all the simulation successfully matched the data, the next step was to apply the same simulation parameters to all the octants. In the simulation kit there were 8 different octants. The number of events was raised to 4 million events so the data can be extracted accurately from all octants (with half million events per octant).

The total rate/yield for each octant is the sum of the nine processes for that octant, as described in Section 3.4. The error was calculated by the quadric Equation 3.12. Each octant rate/yield is unique, however they are very close to the other octants.

$$\text{Total Error} = \sqrt{\frac{1}{(\text{1st Simulation Error})^2} + \dots + \frac{1}{(\text{Last Simulation Error})^2}} \quad (3.12)$$

Figure 3.52 shows that all octants simulation rate and data rate. This plot shows that all detectors generate almost identical results. The spread between the octants' rates are shown for the Δ peak and elastic peak in Figure 3.53 and Figure 3.54, respectively. Also, the relative residual is calculated for all the octants much respect to the real data in Figure 3.55.

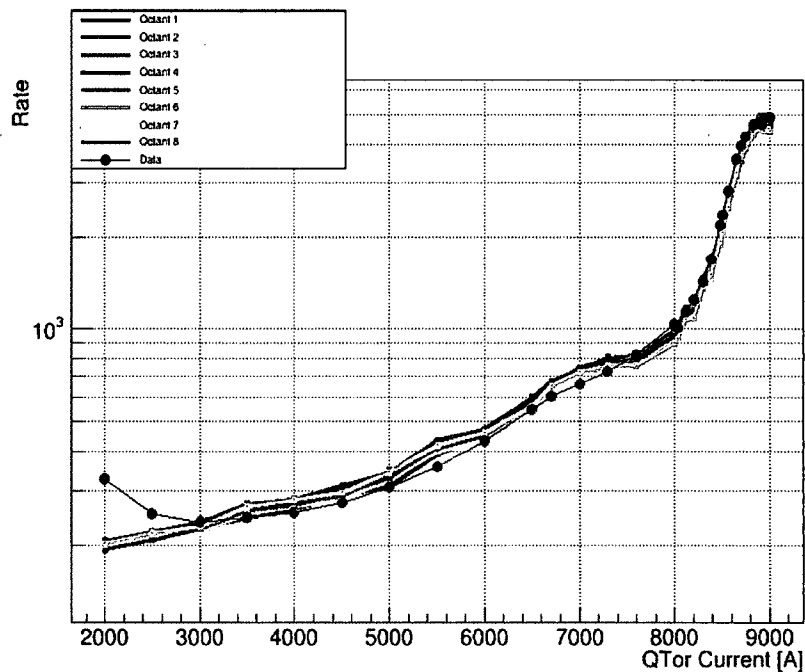


Figure 3.52: Variation of rate (in kHz/uA) as a function of QTor current (A) from all octants simulations, compared with data.

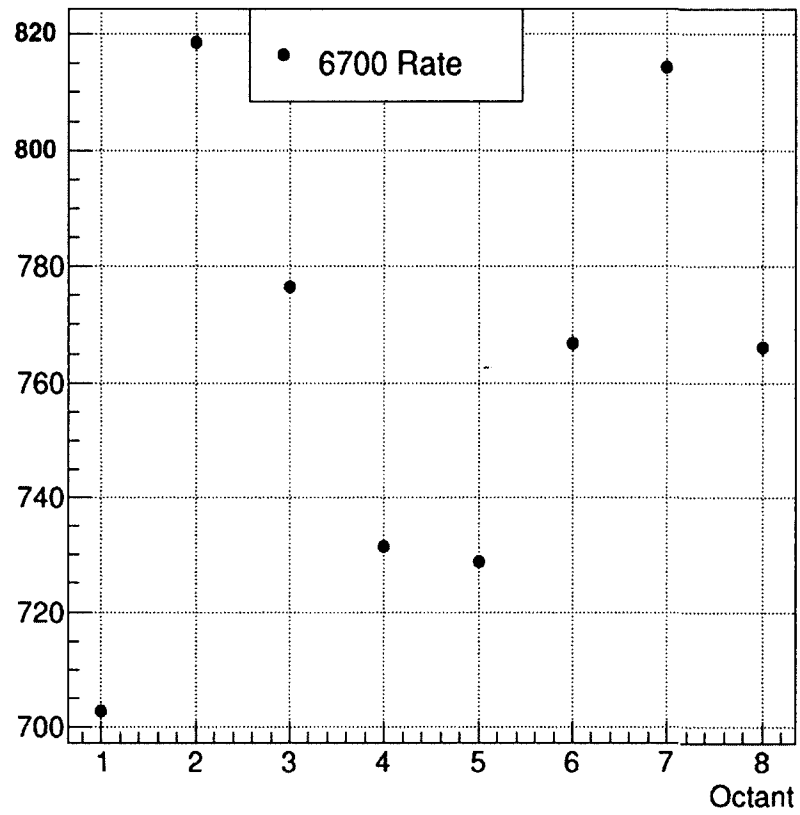


Figure 3.53: Difference between octants rate (in kHz/uA) at $Q_{\text{Tor}} = 6700$ A.

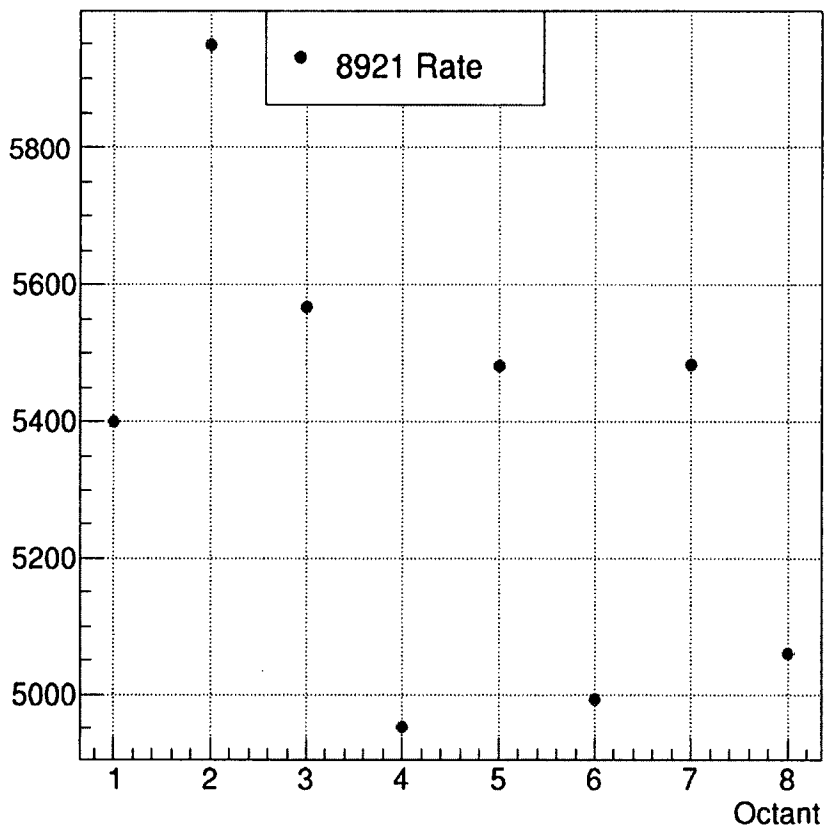


Figure 3.54: Difference between octants rate (in kHz/uA) at $Q_{Tor} = 8921$ A.

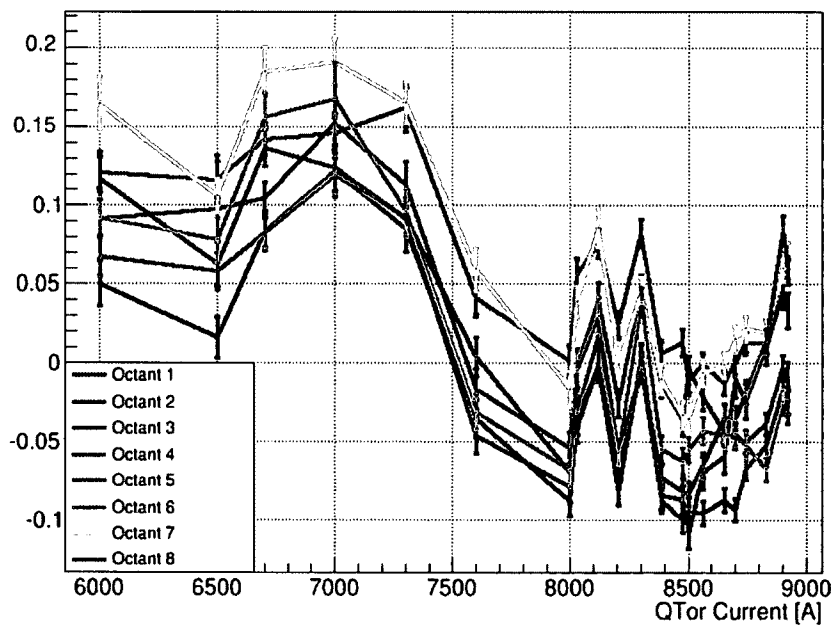


Figure 3.55: Rate relative residual.

To make sure that the correct processes were used, event 5, Section 3.5.2, was brought back to the simulation. It replaced the event generator 7 inelastic part. As shown in Figure 3.56 the simulation curves were lower than the data curve. Furthermore, the relative residual, Figure 3.57, proves that event generator 5 is not the right generator for this simulation.

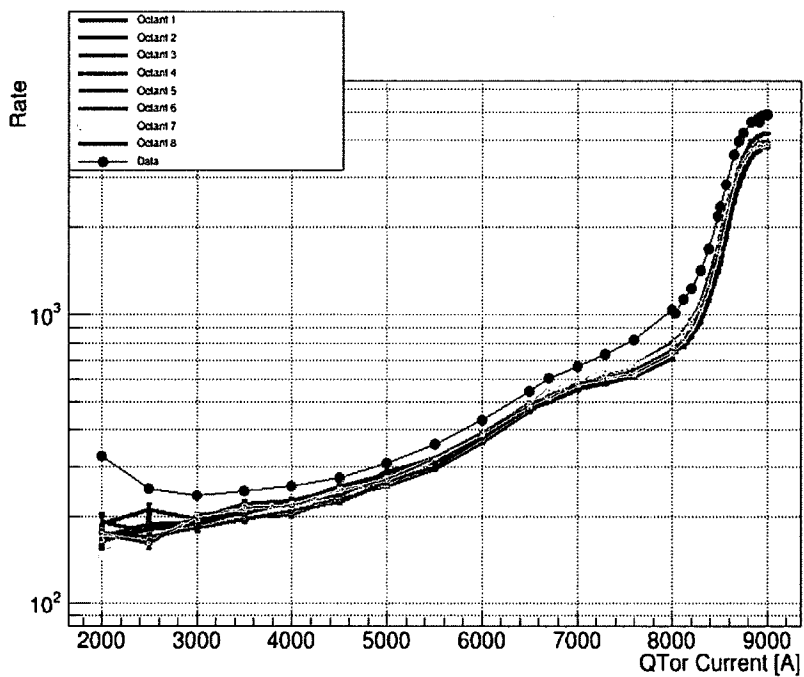


Figure 3.56: Rate simulation for all octants using event 5.

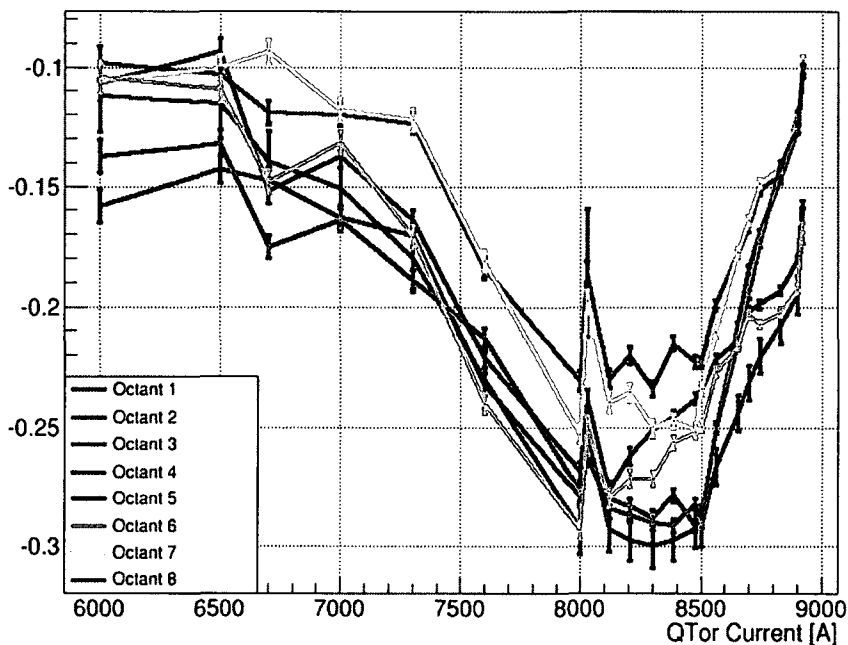


Figure 3.57: Rate relative residual when using event 5.

The yield of all octants compared to the data is plotted in Figure 3.58. The simulation yield was calculated via the Equations below. First, all octant yields were averaged using Equation 3.13. Then, a normalization variable was generated via Equation 3.14. Finally, each total octant yield was normalized such as in Equation 3.15.

$$\bar{Y}_{all} = \frac{Y_1 + .. + Y_8}{8} \quad (3.13)$$

$$n = \frac{Y_{data}}{\bar{Y}_{all}} \quad (3.14)$$

$$Y_{normalized} = n(Y_i) \quad (3.15)$$

where \bar{Y}_{all} is the all octant average yield, $Y_1...Y_8$ are the individual octant yields, $Y_{normalized}$ is the normalized yield, and the Y_i are the different octants' yields.

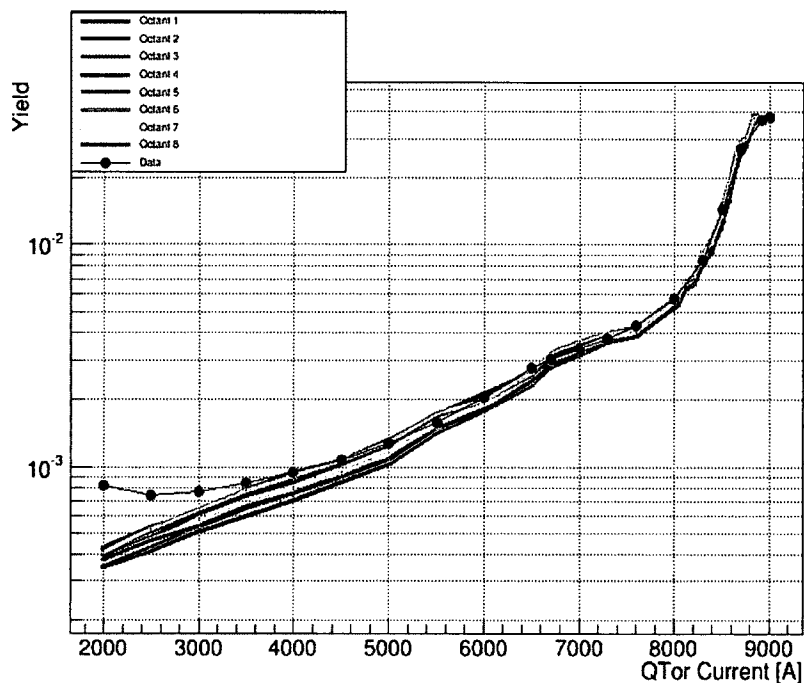


Figure 3.58: Variation of yield as a function of QTor current (A) from all octants simulations, compared with data.

The data and simulation yield agree near both the elastic and Δ peaks. Furthermore, to see the agreement between the octants, their octants' relationship yield is shown in Figure 3.59. Finally, the yield relative residual for all the octants relative to the real data is plotted in Figure 3.60. This plot shows the relationship between all the octants and the real data. This yield relative residual plot includes both simulation and data errors, all will ultimately be used to estimate the systematic error on the elastic dilution factor of the elastic radiative tail contribution to the inelastic yield at 1.16 GeV.

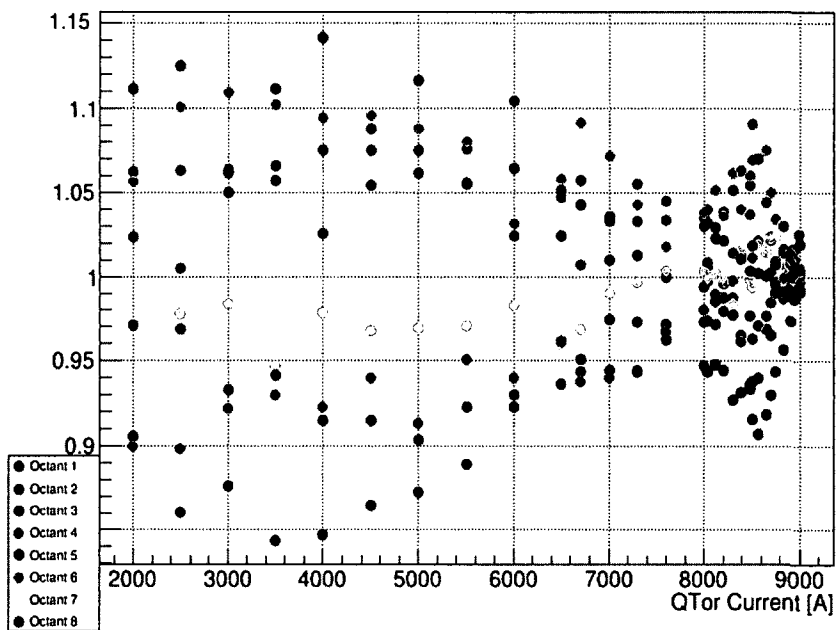


Figure 3.59: Yield average for all octants.

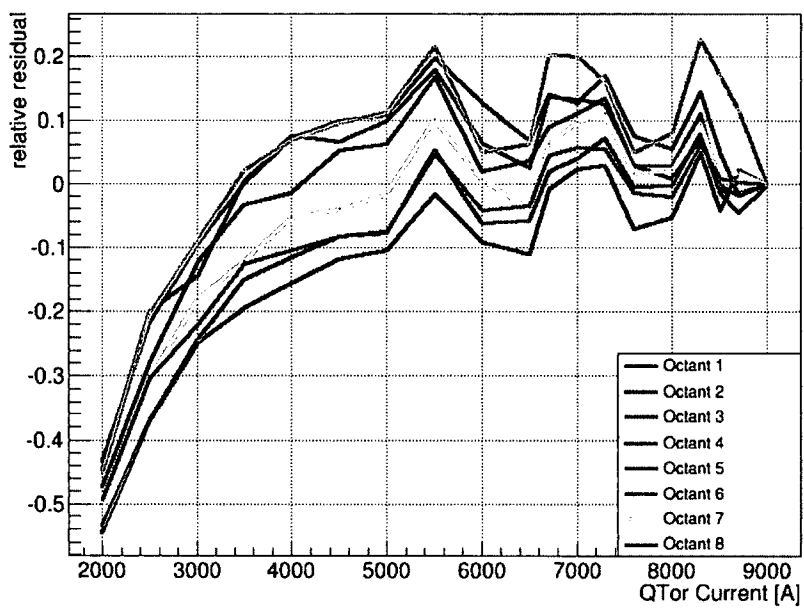


Figure 3.60: Yield relative residual.

3.10 All Octant Simulation for 0.877 GeV

Section 3.8.2 describes and shows the 0.877 GeV simulation for one octant. The results of the simulation for all octants for beam energy 0.877 GeV are shown in this section.

The rate for all octants compared to the data is shown in Figure 3.61. All octants' rates are almost equal and match the data. The jump seen in Figure 3.61 near $Q_{\text{Tor}} = 4700\text{A}$ is due to a hardware configuration change in the physical experiment, in which a pre-scale factor was changed for the TDC used in our measurement technique to extract the rates. Figure 3.62 is plotted to show closely the relationship between the octants.

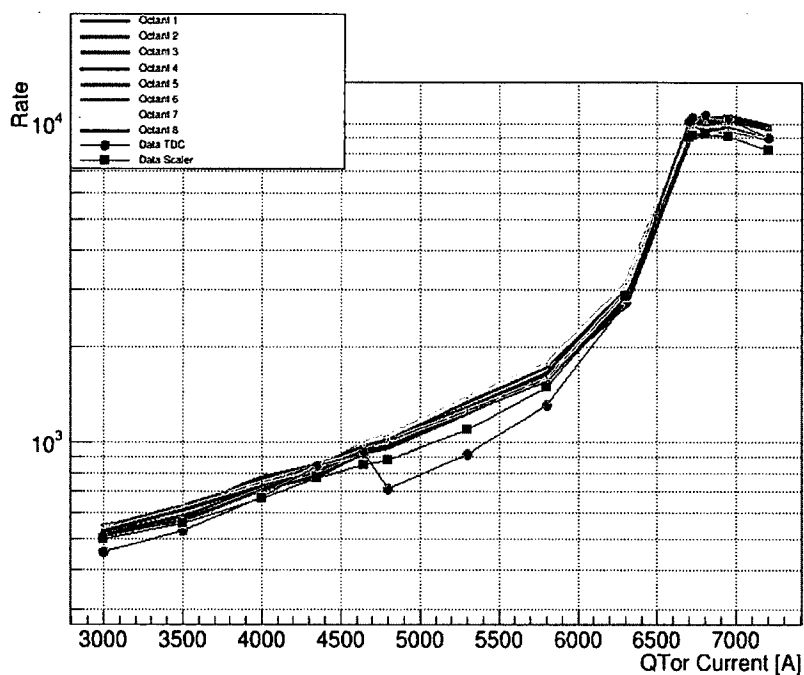


Figure 3.61: Variation of rate (in kHz/uA) as a function of Q_{Tor} current (A) from all octants simulations, compared with data.

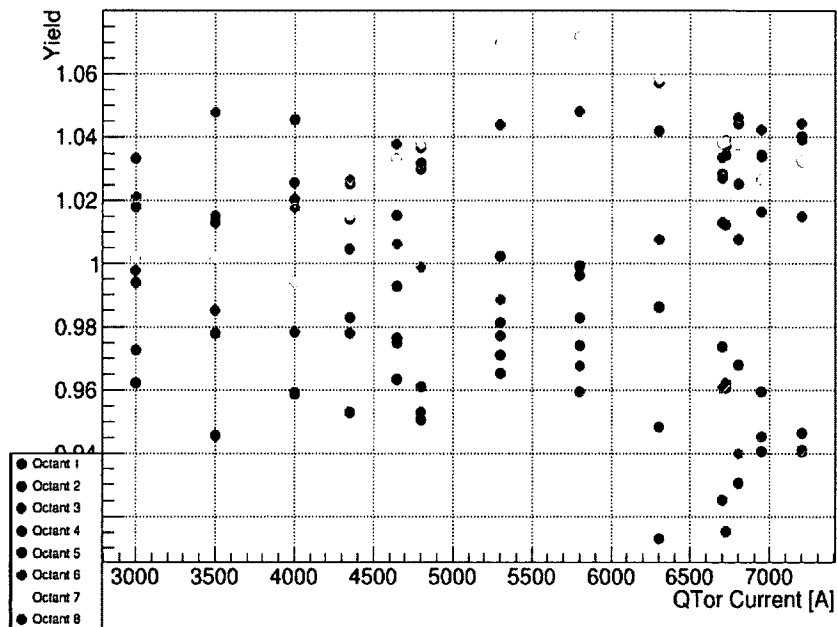


Figure 3.62: 0.877 comparison between rates (in kHz/uA) in different octants.

On the other hand, the 0.877 GeV yields are plotted with the experimental values in Figure 3.63. This plot shows that the yields for all octants are similar. Then, to check the similarity between the data and simulation, the simulation yield has to be normalized to the data. For this beam energy the simulation was normalized to match the data for each octant at the elastic peak, $Q_{\text{Tor}} = 6800$ A.

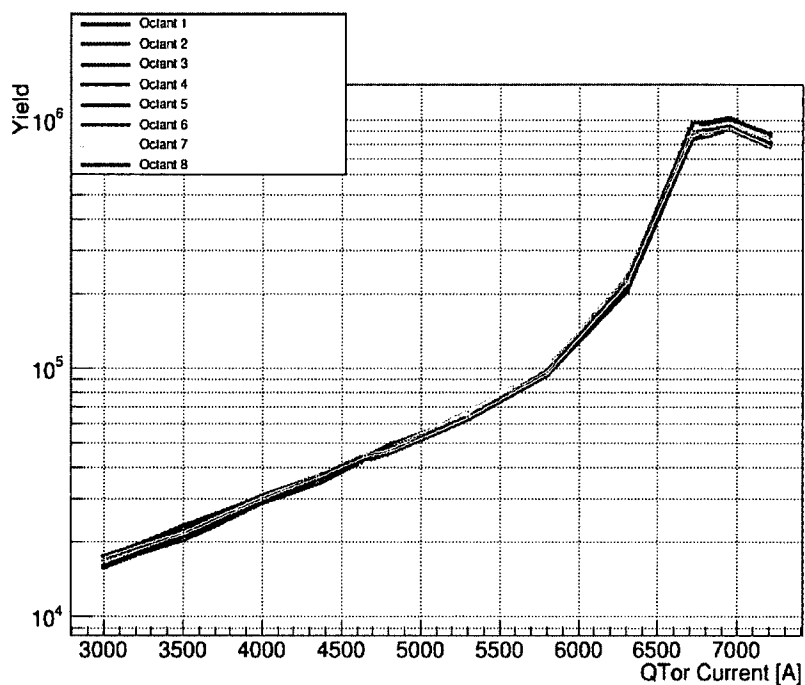


Figure 3.63: Variation of yield (in kHz/uA) as a function of QTor current (A) from all octants simulations.

Figure 3.64 shows the yield after normalization to the data. The plot shows that the each octant yield data from the real experiment matches the simulation yield. The all octants relative residual is shown in Figure 3.65.

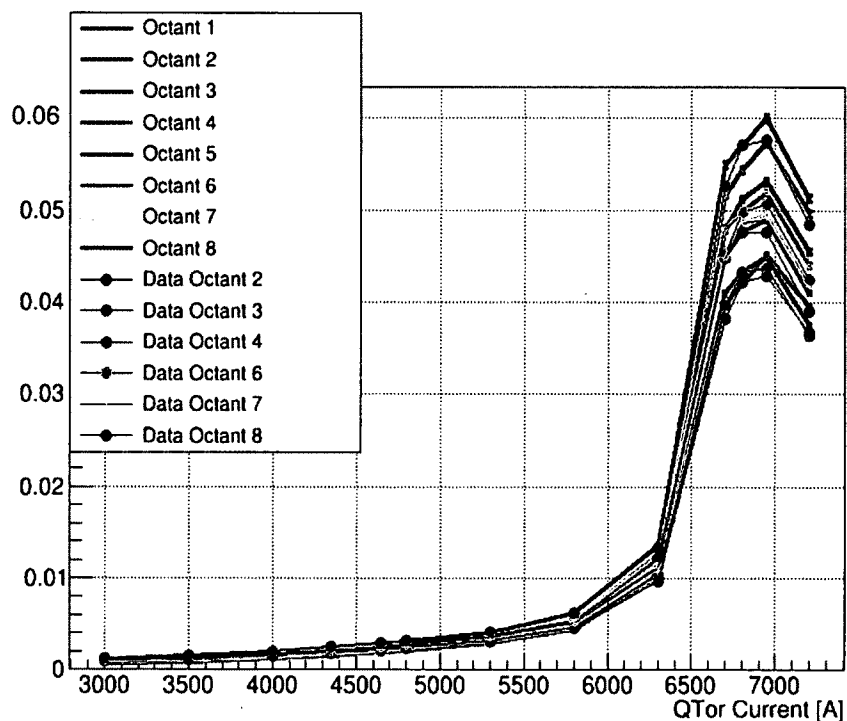


Figure 3.64: Variation of yield as a function of QTor current (A) from all octants simulations, compared with data.

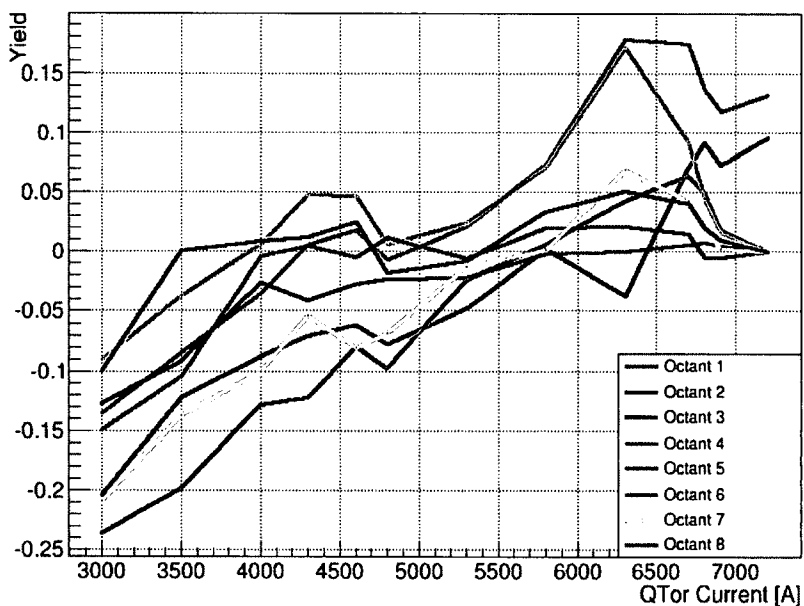


Figure 3.65: All octant 0.877 GeV yield relative residual, octant 1 and octant 5 have odd shape because the physical experimental data don't include these two octants.

3.10.1 Inelastic Fraction

In the physical and simulation experiments, yield and rate had different units. Also, they have different width of the electron acceptance window. At the end, however, they both need to produce similar results. Similar results does not mean exact value and data. It means that the ratio between the data is the same, such as the ratio between simulation data and physical data or the ratio between any of the processes data. Photoelectrons are important for uncertainty on the inelastic fraction. Inelastic fraction is the a critical part of systematic error when extracting the $N \rightarrow \Delta$ asymmetry.

To study this futher, the inelastic fraction of the yield and rate was tested. They were supposed to be equal. The inelastic fraction was calculated by the Equation

$$f = \frac{Y_{\Delta}}{Y_{tot}} \quad (3.16)$$

where f is the inelastic fraction, Y_{Δ} is the Δ peak yield, and Y_{tot} is the total yield.

For the one octant simulation, beam energy 1.16 GeV, the yield and rate inelastic fraction is shown in Figure 3.66. There is a big difference between them, which means that they are not equal. The same process was applied to the all octant simulation. Figure 3.67 shows that each octant has the same difference between the yield and rate's inelastic fraction. Moreover, even for beam energy 0.877 GeV the same problem is present. That is clear in Figure 3.68.

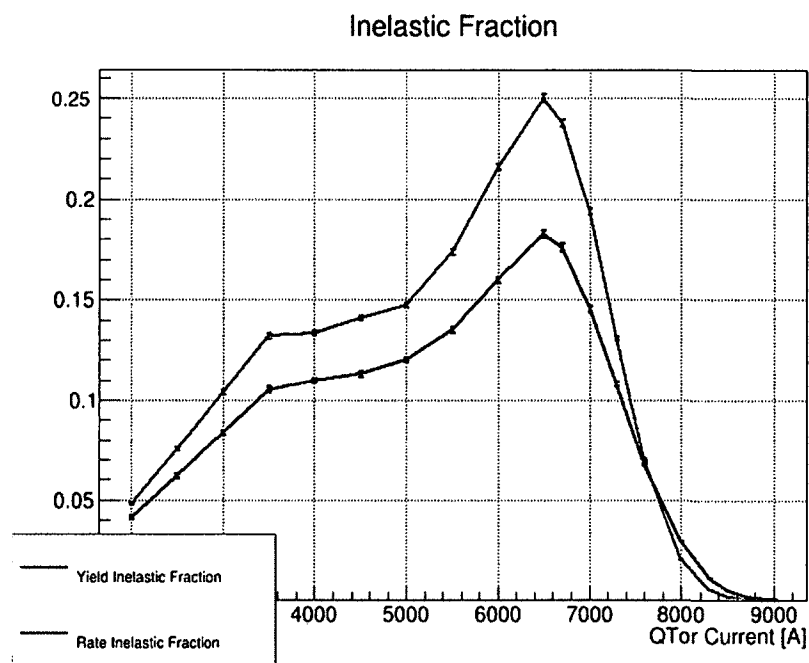


Figure 3.66: One octant rate and yield inelastic fraction for 1.16 GeV.

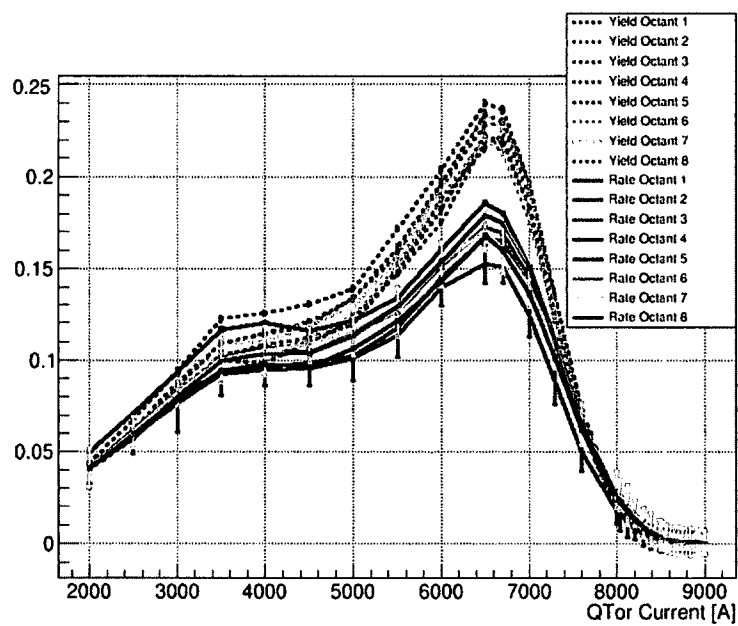


Figure 3.67: All octants rate and yield inelastic fraction for 1.16 GeV.

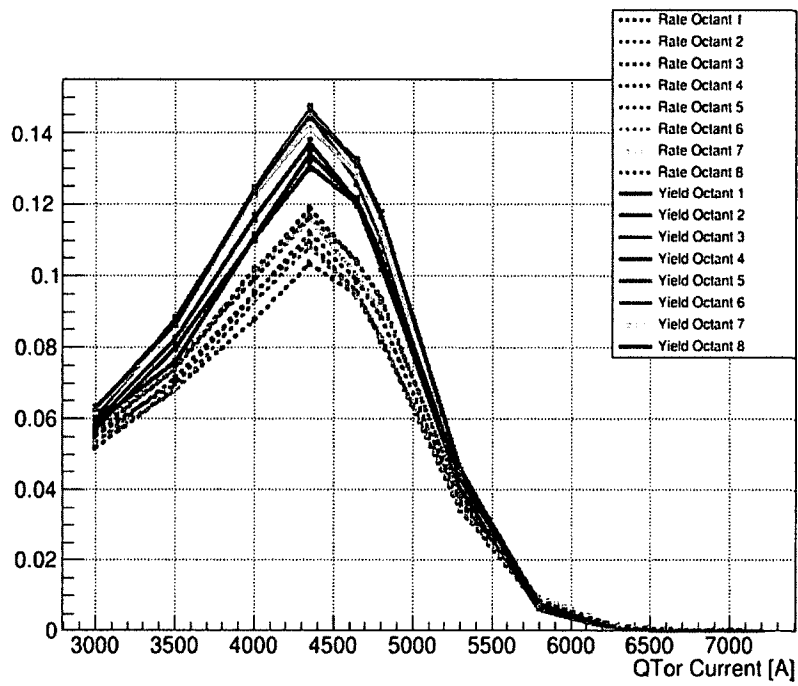


Figure 3.68: All octants rate and yield inelastic fraction for 0.877 GeV.

The first step to diagnose the problem was to plot the number of photoelectrons vs energy. That is to see the amount of light that gets generated from those elastic and inelastic events. Figure 3.69 and Figure 3.70 represent the two dimensional plots for the number of photoelectrons vs energy for event 1 and event 7, respectively.

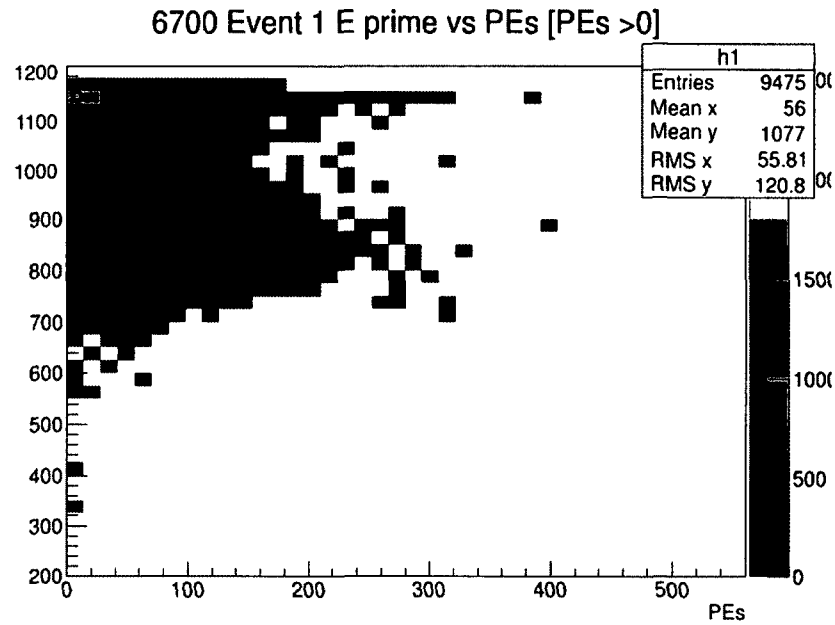


Figure 3.69: Event 1 vertex energy vs number of PEs for octant 7 with cut on PEs > 0 at Qtor 6700.

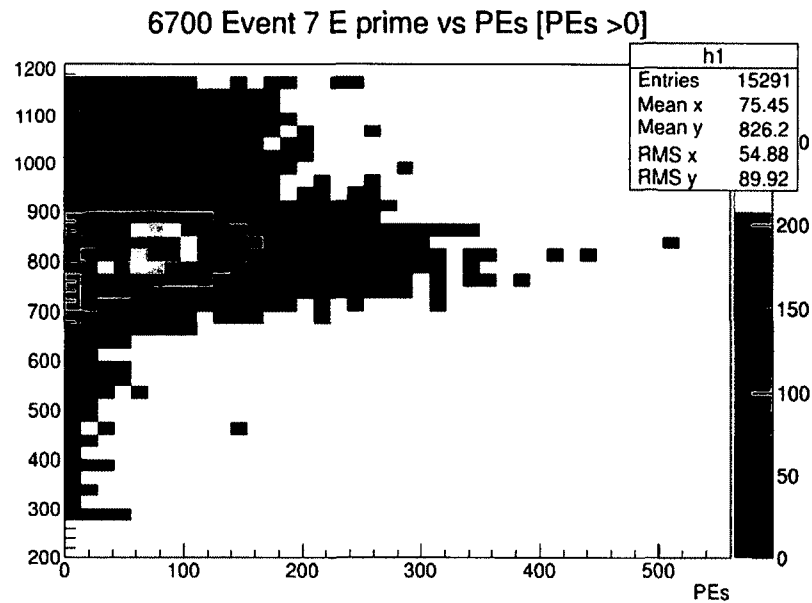


Figure 3.70: Event 7 vertex energy vs number of PEs for octant 7 with cut on PEs > 0 at Qtor 6700.

These plots were not clear to read, so one dimensional plots were created. Figure 3.71 and Figure 3.72 represent the one dimensional plots for the number of photoelectron

vs energy for event 1 and event 7, respectively, at $Q_{\text{Tor}} = 6700\text{A}$, the peak of the Δ rate and yield. Rates count only events that hit the detector, while yield represents the amount of light that is collected by the detector.

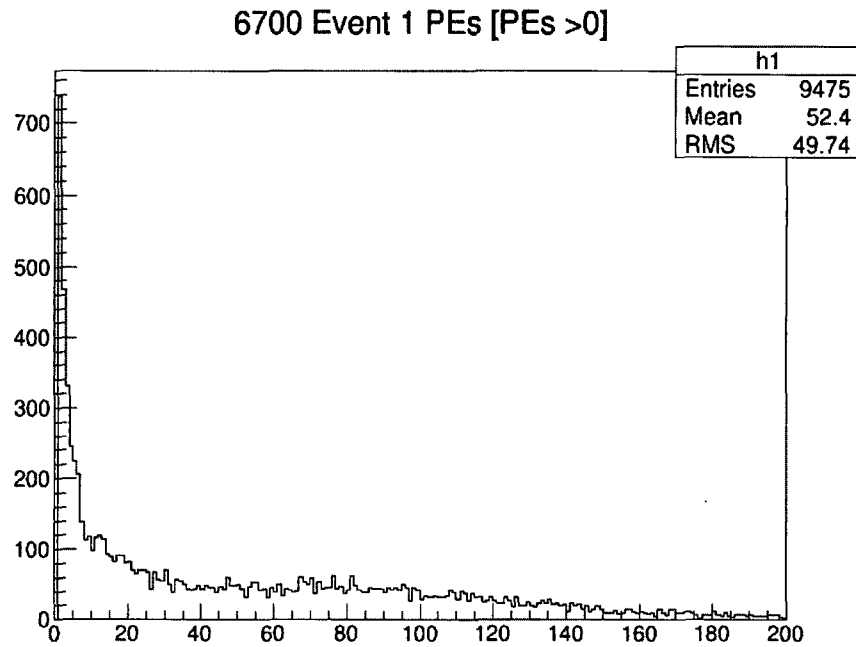


Figure 3.71: Event 1 PE's for $Q_{\text{tor}} = 6700\text{ A}$, with $\text{PEs} > 0$.

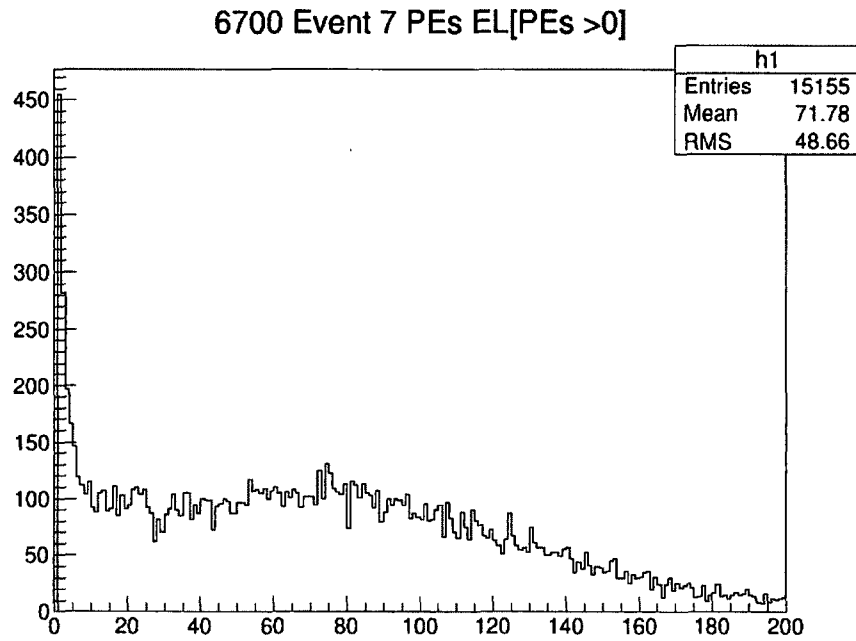


Figure 3.72: Event 7 PE's for $Q_{\text{tor}} = 6700\text{ A}$, with $\text{PEs} > 0$.

Therefore, a new cut was formed on the rate simulation. That cut ensured that low light photoelectron events were included. To extract the yield, it allowed the photomultiplier tubes, which are the tubes that generate the photoelectrons, to be open to all events that have greater than 0 PEs. On the other hand, for the rate extraction, the PMTs had their PE window gradually decreased to allow events with photoelectrons greater than 0, 1, 2, 5, 10 and finally 20 to be counted. The result is displayed in Figure 3.73. The bottom line is that the inelastic fraction for the yield and rate match only when the rate counts the photoelectrons that are greater than 20. Thus, the very low PE events were affecting the rate inelastic fraction but not the yield inelastic fraction. This effect explains the discrepancy between the rate and yield inelastic fractions shown on the in Figures 3.66, 3.67, and 3.68.

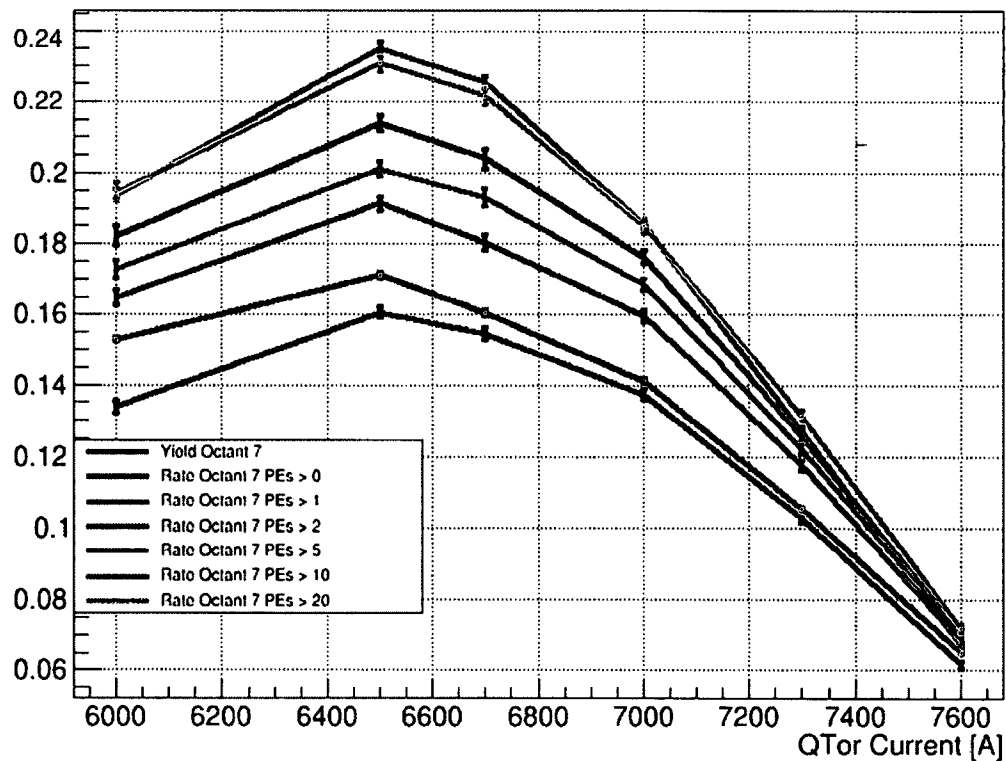


Figure 3.73: Rate and yield inelastic fraction with photoelectron cut.

Elastic, aluminum, and pion fractions were calculated to see the relationship between these processes and the total yield. The elastic fraction was calculated via

Equation 3.11. It is shown in Figure 3.74. All the points were measured at $Q_{Tor} = 6700$ A. However, for more visible view, the points were offset relative to $Q_{Tor} = 6700$ A. Aluminum and pion fractions were calculated by Equations 3.17 and 3.18, respectively. They are presented in Figures 3.75 and 3.76, respectively, as well. Pion and aluminum fractions plots are like the elastic plot in the point of the data taken at $Q_{Tor} = 6700$ A.

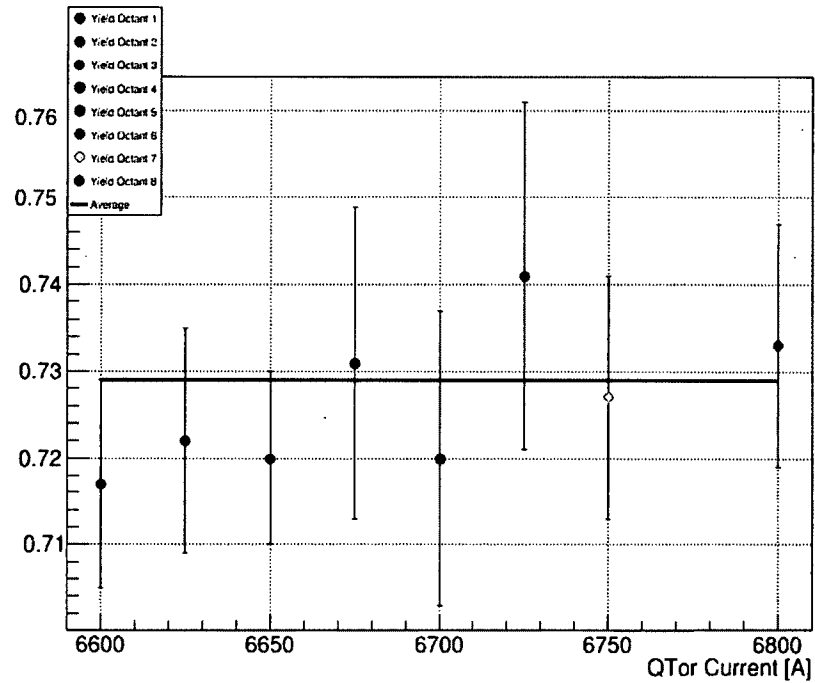


Figure 3.74: Yield elastic fraction at Δ peak.

$$f = \frac{Y_{AL}}{Y_{tot}} \quad (3.17)$$

$$f = \frac{Y_{Pion}}{Y_{tot}} \quad (3.18)$$

where f is the inelastic fraction, Y_{pion} is the pion yield, Y_{AL} is the aluminum yield, and Y_{tot} is the total yield.

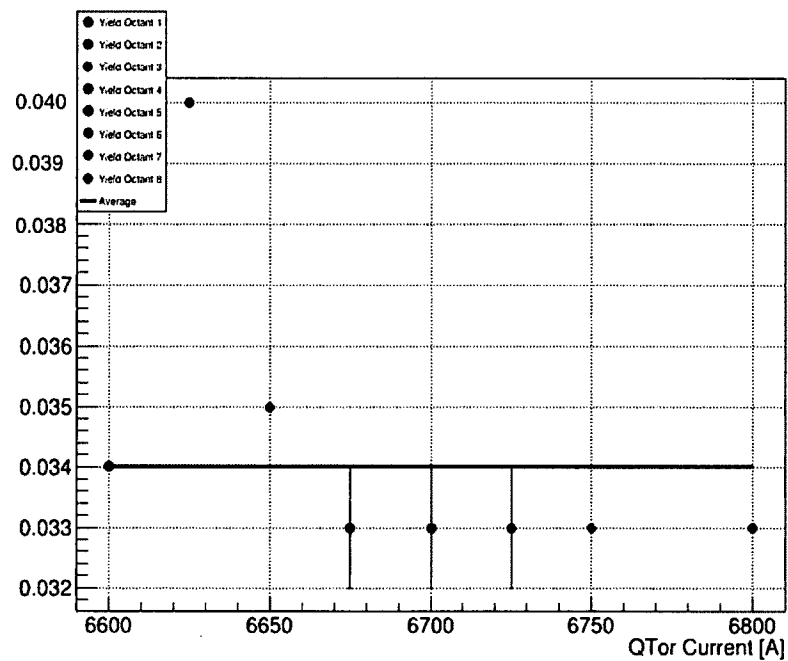


Figure 3.75: Aluminum elastic fraction at Δ peak.

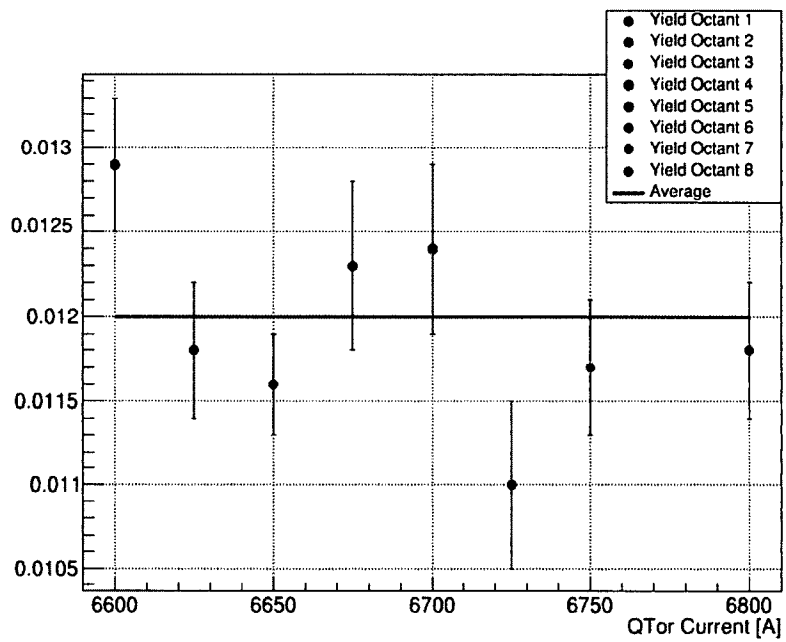


Figure 3.76: Pion elastic fraction at Δ peak.

3.11 Bn Model

Another indication of the accuracy of the inelastic fraction was the Qtor dependency of the inelastic fraction relative to a measured quantity the transverse asymmetry in the $N \rightarrow \Delta$ region known as B_n . The purpose of this section is to outline a model to understand the Qtor dependence of the beam normal single spin asymmetry in the $N \rightarrow \Delta$ region across the Δ peak. The goal was to see if the measured asymmetry at the lowest Qtor point (6000 A) could be reconciled with those measured at the two higher Qtor points (6700 A and 7300 A) with a simple model.

The model is a two component model: the asymmetry of the elastic tail across the Δ peak and at the $N \rightarrow \Delta$ peak, which is assumed to be one constant value across the Δ peak. To that end, the model can be summarized as follows:

The measured asymmetry can be written

$$A_{meas} = \frac{Y_{el}A_{el} + Y_{\Delta}A_{\Delta}}{Y_{el} + Y_{\Delta}} \quad (3.19)$$

where only the elastic and inelastic yields have been taken into account.

In terms of yield fractions, this can be written:

$$A_{meas} = f_{el}A_{el} + f_{\Delta}A_{\Delta} = (1 - f_{\Delta})A_{el} + f_{\Delta}A_{\Delta}. \quad (3.20)$$

To find the best value of A_{Δ} (or in this case B_n) using the four measured values of the asymmetry at the three inelastic points around the Δ peak and including the measured value at the elastic peak (Qtor = 9000 A), we define

$$\chi^2 = \frac{1}{n - N} \sum_i \frac{(A_{model,i} - A_{meas,i})^2}{\delta A_{meas,i}^2} \quad (3.21)$$

where n is the number of data points ($n = 4$ for this case), N is the number of degrees of freedom ($N = 1$ here, the value of B_n), $A_{model,i}$ is the value of the model

given in the second Equation above evaluated at each Qtor value, $A_{meas,i}$ are the measured transverse asymmetries at each Qtor, $\delta A_{meas,i}$ are the statistical errors of those measured values, and the sum runs over the 4 Qtor points. χ^2 then becomes

$$\chi^2 = \frac{1}{3} \sum_i \frac{[(1 - f_{\Delta,i})A_{el,i} + f_{\Delta,i}B_n - A_{meas,i}]^2}{\delta A_{meas,i}^2}. \quad (3.22)$$

The values of $f_{\Delta,i}$ are determined using the simulated values for Y_{el} and Y_{Δ} at each Qtor point. In addition, because we expect the beam normal single spin asymmetry to scale with Q (and not Q^2), the values of $A_{el,i}$ will be taken to be the value measured at the elastic peak (Qtor = 9000 A) multiplied by (Qtor_{*i*}/9000 A). To determine the best value of B_n , we minimize χ^2 with respect to B_n via

$$\frac{d\chi^2}{dB_n} = \frac{2}{3} \sum_i \frac{f_{\Delta,i}[(1 - f_{\Delta,i})A_{el,i} + f_{\Delta,i}B_n - A_{meas,i}]}{\delta A_{meas,i}^2} = 0 \quad (3.23)$$

Solving analytically for B_n yields

$$B_n = -\frac{\sum_i f_{\Delta,i}[(1 - f_{\Delta,i})A_{el,i} - A_{meas,i}]/\delta A_{meas,i}^2}{\sum_i f_{\Delta,i}^2/\delta A_{meas,i}^2}. \quad (3.24)$$

In order to calculate B_n , a choice had to be made for $f_{\Delta,i}$ so we chose Octant 7 elastic and inelastic yields for this calculation. With this choice, we find a value of B_n of

$$B_n = 34.7 \text{ ppm} \quad (3.25)$$

with a resulting $\chi^2/d.o.f.$ of 1.66. Shown in Figure 3.77 is a plot of the inelastic fraction in this model for all Qtor values assuming the value of B_n above using the Octant 7 elastic and inelastic yields from the simulations. In order to estimate an uncertainty on B_n , we varied B_n around the value which minimized χ^2 to see how much χ^2 increased as B_n strayed to values both below and above the value which

minimized χ^2 . The result of this study is plotted in Figure 3.78, where $\chi^2/d.o.f.$ is plotted vs. B_n around the B_n value which minimized χ^2 .

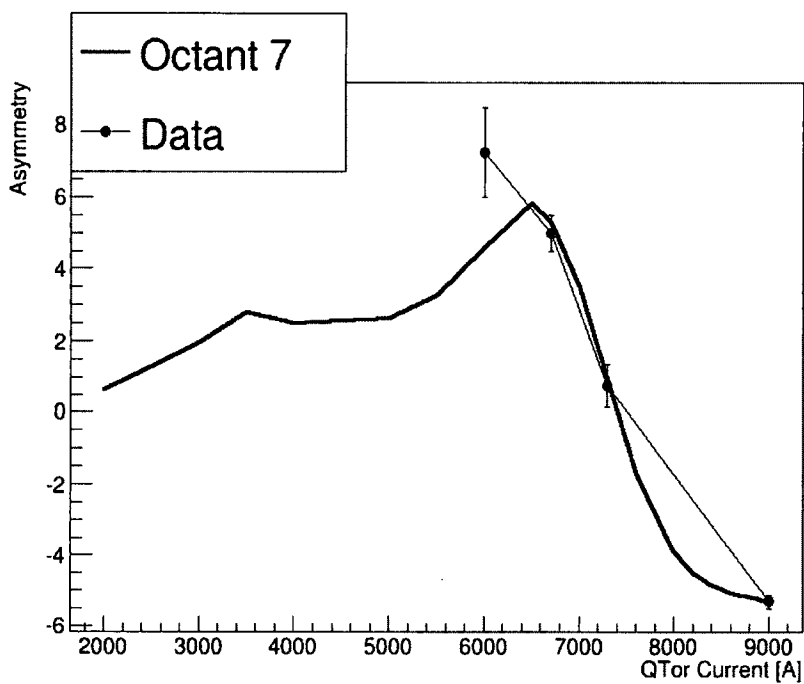


Figure 3.77: The inelastic fraction in B_n model.

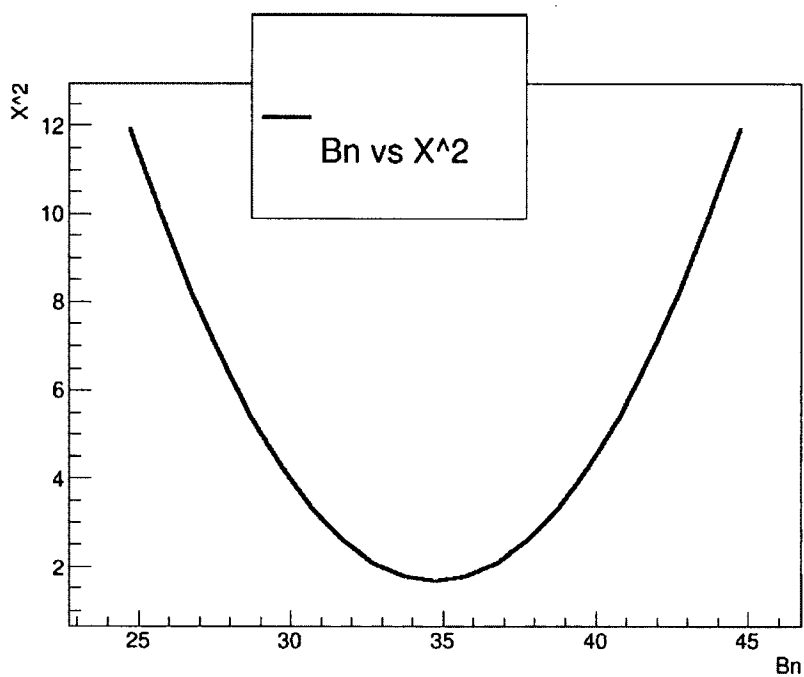


Figure 3.78: $\chi^2/d.o.f.$ vs. B_n around the B_n value which minimized χ^2 .

We propose that an estimate of the uncertainty on B_n can be obtained by identifying by how much B_n can differ from the value which minimized χ^2 until $\chi^2/d.o.f.$ reaches one unit above its minimum value, consistent with the treatment proposed in the Particle Data Group writeup. Based on this assumption, we believe the model error estimate of the uncertainty on B_n is ± 3.0 ppm.

Finally, to estimate the simulation contribution to the uncertainty on B_n , we plot the inelastic fraction for each octant using the value of B_n which minimized χ^2 to see the spread in the values of the inelastic fraction at $Q_{\text{tor}} = 6700$ A, and this plot is shown in Figure 3.79. From these values at $Q_{\text{tor}} = 6700$ A, we estimate a simulation uncertainty of ± 2.9 ppm. To arrive at this value, we took the full spread of values for all octants of ± 4.1 ppm, and multiplied by $\frac{1}{\sqrt{8}}$ to take into account of the statistical deviation in the simulations.

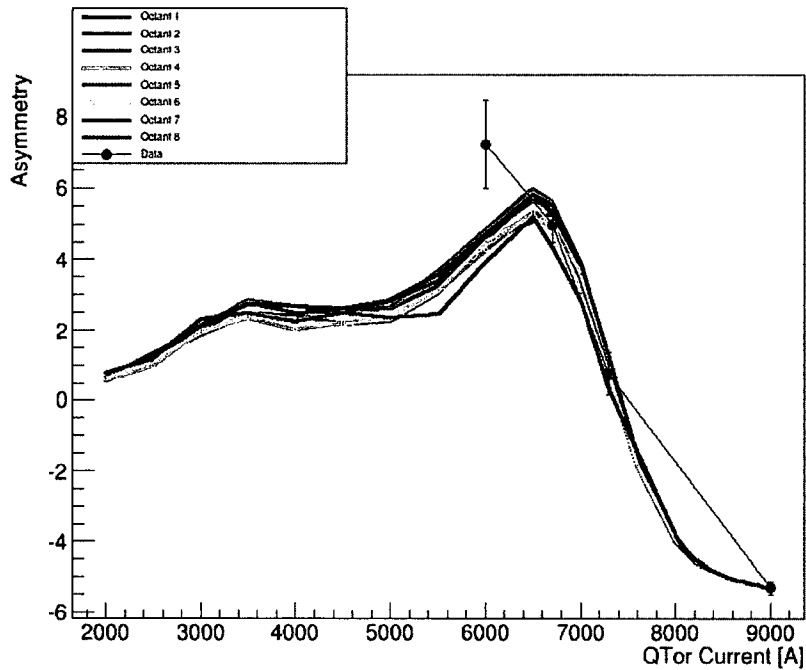


Figure 3.79: The inelastic fraction in B_n model for all Q_{tor} .

Thus, we find a final answer for B_n in this model of

$$B_n = 34.7 \pm 3.0_{\text{model}} \pm 2.9_{\text{simulation}} \text{ ppm.} \quad (3.26)$$

While the model does well for the inelastic Q_{tor} values of 6700 A and 7300 A, it still cannot resolve the discrepancy of the model for $Q_{\text{tor}} = 6000$ A. Considering that the model misses the datum at 6700 A by about two standard deviations (one standard deviation at the smallest value possible including the error), it is possible that the data point simply misses, or there could be an incorrect assumption in the model. Two possibilities come to mind for the latter situation: one is that the assumption that the inelastic asymmetry is constant over the width of the Δ peak, or that there is a component to the model such as a large unaccounted for asymmetry (such as a large single or two pion production asymmetry) that is not included [8].

3.12 Summary

To conclude the rate and yield simulation, below there are plots to show the full simulation for all octants. All octants full simulation rate for 1.16 GeV with all its processes is shown in Figure 3.80. Figure 3.81 shows all octants full simulation rate for 0.877 GeV with all its processes. All octants full simulation yield for 1.16 GeV with all its processes is shown in Figure 3.82. Figure 3.83 shows all octants full simulation yield for 0.877 GeV with all its processes.

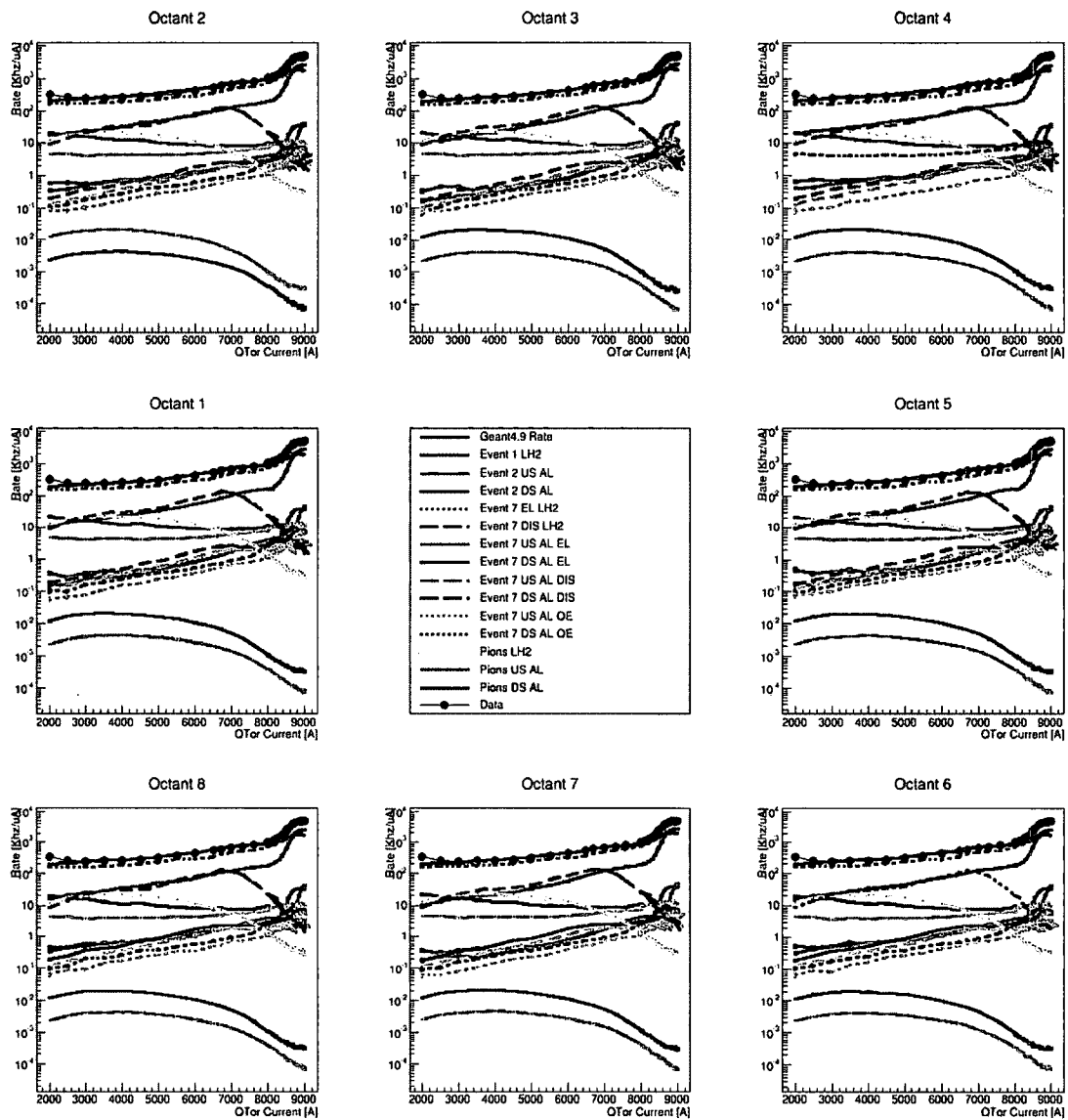


Figure 3.80: 1.16 GeV all actant rate.

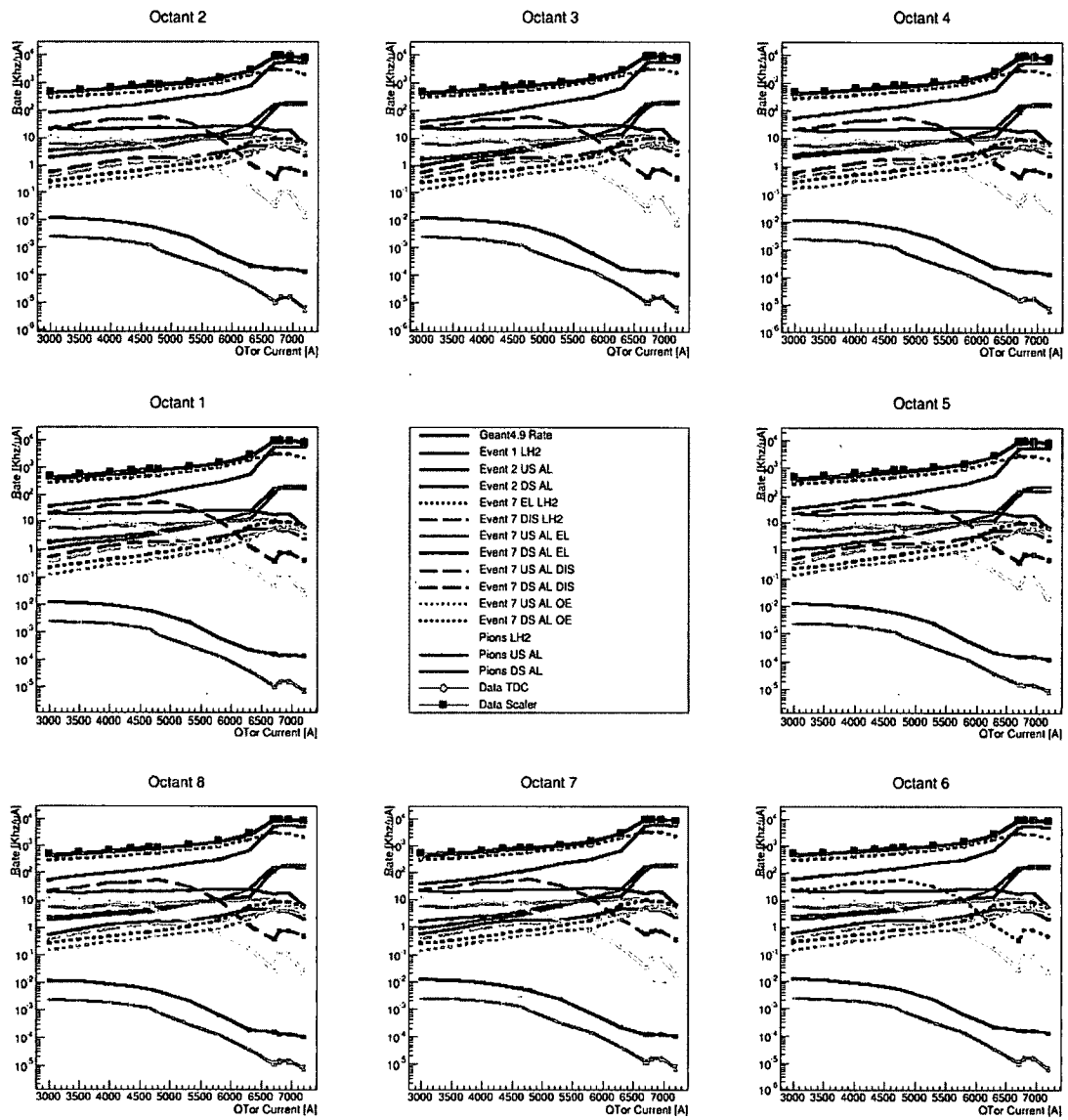


Figure 3.81: 0.877 GeV all octant rate.

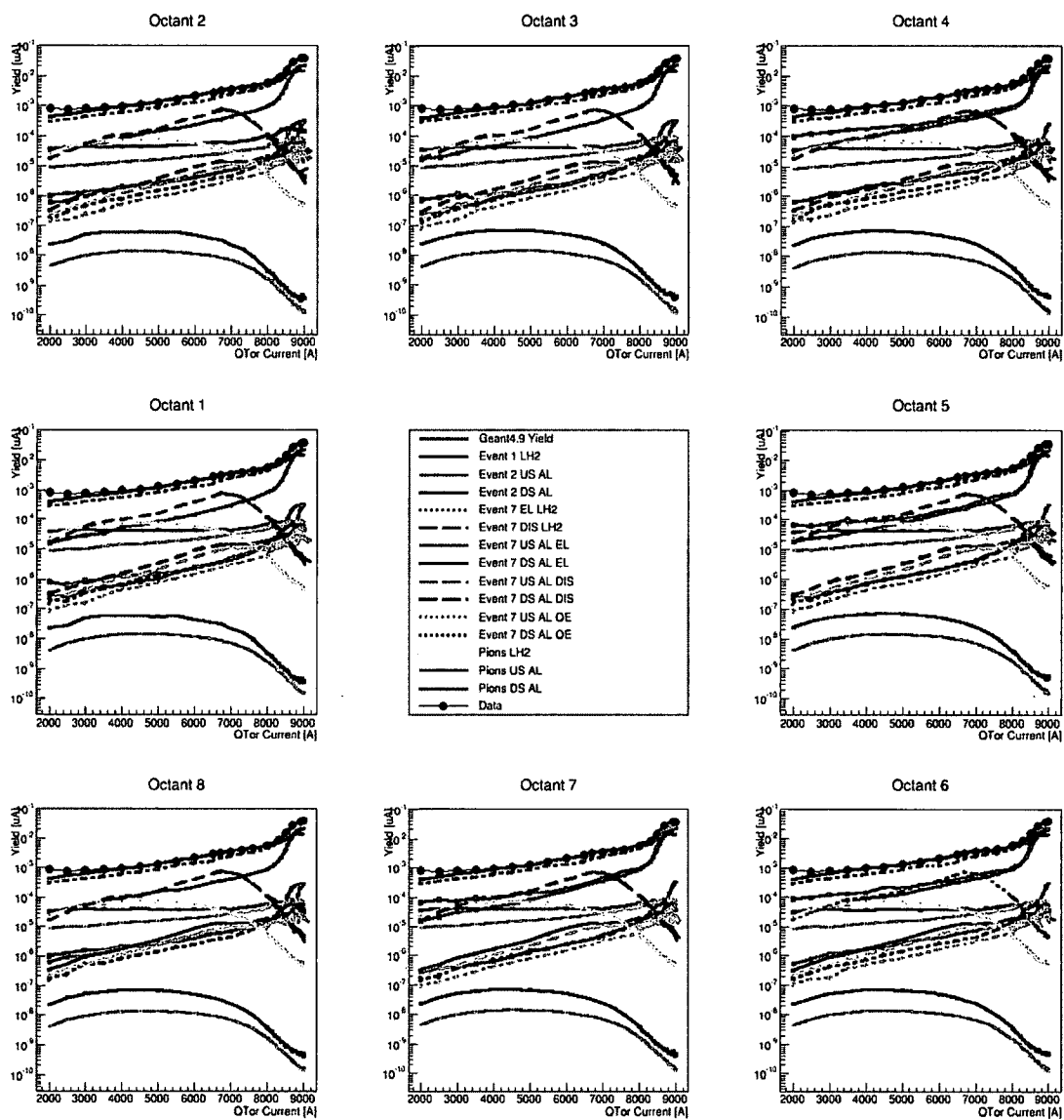


Figure 3.82: 1.16 GeV all octant yield.

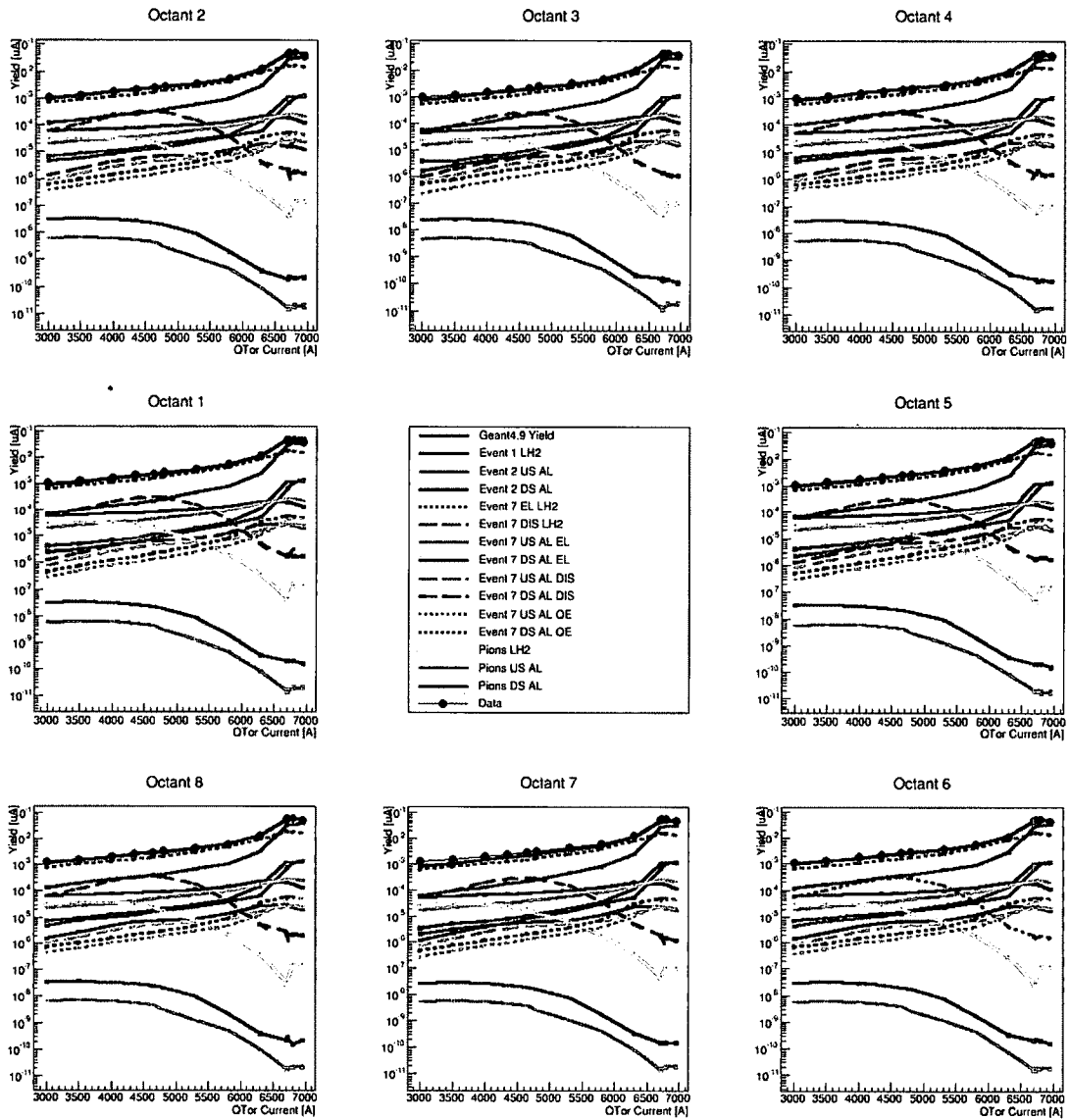


Figure 3.83: 0.877 GeV all octant yield.

In addition, the yield fractions have been calculated for elastic, aluminum and pions at the Δ peak, $Q_{\text{Tor}} = 6700\text{A}$ for 1.16 GeV, and $Q_{\text{Tor}} = 4650\text{A}$ at 0.877 GeV, given in Tables 3.2 and 3.3, respectively. These are required to determine the uncertainty in extracting the $N \rightarrow \Delta$ asymmetry for those two beam energies. In the next chapter we outline the impact of these yield fractions on extracting these asymmetries.

Chapter 4

IMPACT OF SIMULATION ON EXTRACTION OF $N \rightarrow \Delta$ ASYMMETRIES

Simulation is important to the Qweak experiment because it plays a dominant part in extracting the $N \rightarrow \Delta$ asymmetries. To extract the asymmetry, first A_{raw} is measured in the data then it is corrected. A_{raw} , which is the raw asymmetry taken directly from the data stream, is necessary to determine A_{msr} which will ultimately be used in extracting the $N \rightarrow \Delta$ asymmetry. The formalization for calculating A_{msr} from A_{raw} is

$$A_{msr} = A_{raw} + A_{BCM} + A_{beam} + A_{BB} + A_L + A_T + A_{bias} - A_{blind} \quad (4.1)$$

where A_{BCM} which is the residual charge asymmetry, A_{beam} which is the residual helicity correlated beam asymmetry, A_{BB} which is the beam-line background asymmetry, A_L which is the non linearity induced asymmetry, A_T which is transverse asymmetry, A_{bias} is a detector related false asymmetry, and A_{blind} is simply a constant added to A_{msr} before any analysis to avoid bias during analysis. Also, another variable R_{tot} is needed to be calculated to extract the $N \rightarrow \Delta$ asymmetries. It is a combination of various experimental radiative correction due primarily to kinematic variations, and is calculated as

$$R_{tot} = R_{det} R_{rc} R_{acc} R_Q^2. \quad (4.2)$$

Finally, the $N \rightarrow \Delta$ asymmetry is extracted via

$$A_{N \rightarrow \Delta} = R_{tot} \left\{ \frac{\frac{A_{msr}}{P} - \sum_{i=1,3,4,5} f_i A_i}{1 - \sum_{i=1}^5 f_i A_i} \right\} \quad (4.3)$$

where $f_{1,4,5}$ are obtained from the simulation. f_1 is the aluminum fraction at $Q_{Tor} = 6700$ A, f_4 is the elastic fraction at $Q_{Tor} = 6700$ A, f_5 is the pion fraction at $Q_{Tor} = 6700$ A, while f_2 is the beam-line background fraction, and f_3 is the neutral particle fraction. Table 4.1 shows the values of $f_{1,4,5}$ for 1.16 GeV.

Table 4.1: Aluminum, Elastic, and Pion fractions at $Q_{tor} = 6700$ A.

Qtor	6700
f_1	0.03580
Error	0.00001
f_4	0.7242
Error	0.0026
f_5	0.0110
Error	0.0007

Table 4.2 shows the values of $f_{1,4,5}$ for 0.877 GeV. f_1 is the aluminum fraction at $Q_{Tor} = 4650$ A, f_4 is the elastic fraction at $Q_{Tor} = 4650$ A, and f_5 is the pion fraction at $Q_{Tor} = 4650$ A.

Table 4.2: Aluminum, Elastic, and Pion fractions at $Q_{tor} = 4650$ A.

Qtor	4650A
f_1	0.069
Error	0.001
f_4	.790
Error	0.013
f_5	0.0097
Error	0.0001

The correction for A_{bcm} , A_{beam} , A_{BB} , A_L , A_T , and A_{bias} will be obtained via measurements in the physical experiment and will be done in a later work.

Chapter 5

SUMMARY

This work accomplished a complete simulation of the Qweak experiment using Geant4 tools. This simulation was much improved over the last simulation, which was performed under Geant3. The simulation included three reaction regions which represent the experimental target. These reaction regions are the liquid hydrogen target (LH_2), front entrance, and back exit aluminum windows. The simulation also used four reaction types: electron proton elastic scattering, electron aluminum elastic scattering, electron proton radiative scattering, and electron pion electro-production. Electron proton elastic scattering reaction and electron aluminum scattering types were modified to include a radiative correction formula.

The simulation was fully done for both beam energies 1.16 GeV and 0.877 GeV. The rate and yield of both beam energies were extracted and compared to the physical experimental data. The simulation yield was normalized to match the physical experiment at the elastic peak. The rate simulation agreed with the physical data without normalization, while the yield simulation curve agreed with the physical data curve. Furthermore, this work simulated the whole experiment through all eight detectors.

From these simulation, the yield fractions from elastic electron proton, electron aluminum, and pions at the Δ peak have been determined, and are necessary to extract the PV asymmetries in the $N \rightarrow \Delta$ asymmetry for 1.16 and 0.877 GeV. In

the process of verifying the validity of these background fractions, we determined the best value of a quantity measured during the Qweak experiment: the beam normal asymmetry, B_n in the $N \rightarrow \Delta$ transition. Finally, elastic, aluminum, and pion yield fractions have been extracted from the background process to get simulation corrections in extracting parity violating $N \rightarrow \Delta$ asymmetries.

APPENDIX

This code is event generator 1 function. It is part of the simulation package.

```

G4double QweakSimEPEvent::Elastic_Cross_Section_Proton
(G4double E_in ,
G4double Theta ,
G4double &fWeightN ,
G4double &Q2,
G4double &E_out)
{
G4double Lamda_2 = 0.710;
G4double M_p = 938.2796 * MeV; // proton mass in MeV
G4double mu = 2.793;
G4double Z = 1.0;
G4double A = 1.0;
G4double M = M_p*A;
G4double myhbarc = hbarc / MeV / fermi;
G4double alpha = 1.0/137.035999074;
G4double CC = myhbarc*alpha/2.0;
G4double Electron_Mass = 0.511 * MeV;

//   E_in units is MeV

const G4double theta_min = 0.01 * degree;
if (Theta < theta_min) {
Theta = theta_min;
G4cout<<" Warning: ~Elastic_Cross_Section_Proton:
~~~~theta_less_than"
<<theta_min<<G4endl;

```

```

G4cout<< "Warning: Elastic_Cross_Section_Proton:
      theta_was_set_to"
      << theta_min<<G4endl;
}

G4double CTH = cos(Theta/2.);
G4double STH = sin(Theta/2.);
G4double T2THE = STH*STH/CTH/CTH;
G4double ETA = 1.0+2.0*E_in*STH*STH/M;
E_out = E_in/ETA;
Q2 = 4.0*E_in*E_out*STH*STH;
G4double tau = Q2/4.0/M/M;
//Mott scattering cross-section,
//including recoil correction
G4double CrossSection = (Z*CC/E_in*CTH/STH/STH)
      *(Z*CC/E_in*CTH/STH/STH)/ETA;
//Units: ub/sr
G4double Mott = CrossSection*10000.0;
//Cross section
G4double GEP_DIPOLE =
1.0/(1.0+Q2/1.E6/Lamda_2)/(1.0+Q2/1.E6/Lamda_2);
G4double GMP_DIPOLE = GEP_DIPOLE*mu;
G4double FAC = 1.0/(1.0+tau);

//The next two line is to add schwinger
G4double FunctionofTheta =
      log (STH*STH) * log (CTH*CTH);

```

```

G4double delta_Schwinger =
    (-2.0*alpha/pi) * ((log(E_in/15.0)
    - 13.0/12.0)
    * (log(Q2/(Electron_Mass*Electron_Mass)) - 1.0)
    + 17.0/36.0 + FunctionofTheta/2.0);
//G4double omega_Sch = E_in - 15;
G4double Sigma_Dipole;
Sigma_Dipole = Mott*
    (GEP_DIPOLE*GEP_DIPOLE*FAC+tau*GMP_DIPOLE*GMP_DIPOLE
    *(FAC+2.*T2THE));
Sigma_Dipole *= (1.0 + delta_Schwinger);
fWeightN = Sigma_Dipole*sin(Theta);
return Sigma_Dipole;
}

```

This code is to to send the parameters to the simulation package to perform the simulation experiment.

```
#=====
# Macro file when runing in batch mode
#      (no graphical output)
#
# usage:
# Macro file for 3-pass running
#=====

# This turns off processes for all particles
#/process/inactivate msc
#/process/inactivate eBrem
#/process/inactivate compt
#/process/inactivate eIoni
#/process/inactivate phot
#/process/inactivate Cerenkov

# or you can turn it off only for electrons
#/particle/select e-
#/particle/process/dump
#/particle/process/inactivate 3

# load/execute this macro:
/control/execute myQweakConfiguration.mac
```

```
# Select the tracking flag
# 0: Allow primaries only (default)
# 1: Allow primaries and optical photons only
# 2: track all primaries and their secondaries
#except optical photons
# 3: track all primaries and their secondaries
#
#/TrackingAction/TrackingFlag 0
#/TrackingAction/TrackingFlag 1
#/TrackingAction/TrackingFlag 2
/TrackingAction/TrackingFlag 3

#/Analysis/RootFileName QweakSimNew.root
/Analysis/RootFileStem QwSim3pass

/EventGen/SelectOctant 7

#####
# 3-pass beam settings
/EventGen/SetBeamEnergy 3.35 GeV
/MagneticField/SetActualCurrent 9000 A
/EventGen/SetThetaMin 5.5 degree
/EventGen/SetThetaMax 12 degree
/EventGen/SetEPrimeMin 0.95 GeV
/EventGen/SetEPrimeMax 1.25 GeV
/EventGen/SelectReactionType 7
```

/Trigger/Disable cer

/Trigger/Enable all

#/run/verbose 2

#/tracking/verbose 2

/run/beamOn 100

This code is to extract the rate, or any other kinematics, from Root. To get the information of any kinematics, just change the command inside the draw command.

```
{
#include<math.h>

    TCanvas *canvas[20];
    TChain *tree = new TChain("QweakSimG4_Tree");
    TChain *tree2 = new TChain("QweakSimG4_Tree");

    TChain *tree3 = new TChain("QweakSimG4_Tree");
    TChain *tree4 = new TChain("QweakSimG4_Tree");
    TChain *tree5 = new TChain("QweakSimG4_Tree");
    TChain *tree6 = new TChain("QweakSimG4_Tree");
    TChain *tree7 = new TChain("QweakSimG4_Tree");
    TChain *tree8 = new TChain("QweakSimG4_Tree");
    TChain *tree9 = new TChain("QweakSimG4_Tree");
    TChain *tree10 = new TChain("QweakSimG4_Tree");

tree->Add("my1160QtorScanAllOcE7LH2_2000*.root");
tree2->Add("my1160QtorScanAllOcE7LH2_2500*.root");
tree3->Add("my1160QtorScanAllOcE7LH2_3000*.root");
tree4->Add("my1160QtorScanAllOcE7LH2_3500*.root");
tree5->Add("my1160QtorScanAllOcE7LH2_4000*.root");
tree6->Add("my1160QtorScanAllOcE7LH2_4500*.root");
tree7->Add("my1160QtorScanAllOcE7LH2_5000*.root");
tree8->Add("my1160QtorScanAllOcE7LH2_5500*.root");
tree9->Add("my1160QtorScanAllOcE7LH2_6000*.root");
tree10->Add("my1160QtorScanAllOcE7LH2_6500*.root");
```

```

ofstream myfile , myfile , myfile , myfilePeak ,
        myfileerror , myfileerror , myfilePeakerror ;
myfile.open ("RatePionR1g15O7.txt");
myfileerror.open ("RatePionR1g15O7error.txt");

for (Int_t i = 1; i <=1 /*var_count*/; i++) {
if (i==1)
{
canvas[i] = new TCanvas(Form("Rate%d" , i) ,
                        Form("Rate-%d" , i) ,600,600);
canvas[i]->Divide(8,6);
for (Int_t pad = 1; pad <= 10; pad++) {
canvas[i]->cd(pad);

if (pad == 1){
tree->Draw("Cerenkov.PMT.PMTTotalRate[7] <->y" ,
          "Cerenkov.PMT.PMTTotalNbOfPEs[7]>20");
Double_t y_Rate=y->GetMean()*y->GetEntries();
Double_t y_error=y->GetMeanError()*y->GetEntries();
        }
if (pad==2){
tree2->Draw("Cerenkov.PMT.PMTTotalRate[7] <->y2" ,
          "Cerenkov.PMT.PMTTotalNbOfPEs[7]>20");
Double_t y_Rate2=y2->GetMean()*y2->GetEntries();
Double_t y_error2=y2->GetMeanError()*y2->GetEntries();
        }
}
}
}

```

```

if (pad==3){
tree3->Draw("Cerenkov.PMT.PMTTotalRate[7]└>>y3" ,
           "Cerenkov.PMT.PMTTotalNbOfPEs[7]>20");
Double_t y_Rate3=y3->GetMean()*y3->GetEntries();
Double_t y_error3=y3->GetMeanError()*y3->GetEntries();
}
if (pad==4){
tree4->Draw("Cerenkov.PMT.PMTTotalRate[7]└>>y4" ,
           "Cerenkov.PMT.PMTTotalNbOfPEs[7]>20");
Double_t y_Rate4=y4->GetMean()*y4->GetEntries();
Double_t y_error4=y4->GetMeanError()*y4->GetEntries();
}
if (pad ==5){
tree5->Draw("Cerenkov.PMT.PMTTotalRate[7]└>>y5" ,
           "Cerenkov.PMT.PMTTotalNbOfPEs[7]>20");
Double_t y_Rate5=y5->GetMean()*y5->GetEntries();
Double_t y_error5=y5->GetMeanError()*y5->GetEntries();
}
if (pad == 6){
tree6->Draw("Cerenkov.PMT.PMTTotalRate[7]└>>y6" ,
           "Cerenkov.PMT.PMTTotalNbOfPEs[7]>20");
Double_t y_Rate6=y6->GetMean()*y6->GetEntries();
Double_t y_error6=y6->GetMeanError()*y6->GetEntries();
}
if (pad == 7){
tree7->Draw("Cerenkov.PMT.PMTTotalRate[7]└>>y7" ,
           "Cerenkov.PMT.PMTTotalNbOfPEs[7]>20");

```

```

Double_t y_Rate7=y7->GetMean()*y7->GetEntries();
Double_t y_error7=y7->GetMeanError()*y7->GetEntries();
    }
if (pad == 8){
tree8->Draw("Cerenkov.PMT.PMTTotalRate[7]_>>y8" ,
           "Cerenkov.PMT.PMTTotalNbOfPEs[7]>20");
Double_t y_Rate8 =y8->GetMean()*y8->GetEntries();
Double_t y_error8=y8->GetMeanError()*y8->GetEntries();
    }
if (pad == 9){
tree9->Draw("Cerenkov.PMT.PMTTotalRate[7]_>>y9" ,
           "Cerenkov.PMT.PMTTotalNbOfPEs[7]>20");
Double_t y_Rate9 =y9->GetMean()*y9->GetEntries();
Double_t y_error9=y9->GetMeanError()*y9->GetEntries();
    }
if (pad == 10){
tree10->Draw("Cerenkov.PMT.PMTTotalRate[7]_>>y10" ,
            "Cerenkov.PMT.PMTTotalNbOfPEs[7]>20");
Double_t y_Rate10=y10->GetMean()*y10->GetEntries();
Double_t y_error10=y10->GetMeanError()*y10->GetEntries();
    }}}}

```

```

myfile << y_Rate << "\n" << y_Rate2 << "\n"
<< y_Rate3 << "\n" << y_Rate4 << "\n"<< y_Rate5
<< "\n"<< y_Rate6 << "\n"<< y_Rate7 << "\n"<< y_Rate8
<< "\n"<< y_Rate9 << "\n"<< y_Rate10 << "\n";

```

```
myfileerror << y_error << "\n"<< y_error2 << "\n"  
.. << y_error3 << "\n"<< y_error4 << "\n"<< y_error5  
<< "\n"<< y_error6 << "\n"<< y_error7 << "\n"<< y_error8  
<< "\n"<< y_error9 << "\n"<< y_error10 << "\n";  
}
```

BIBLIOGRAPHY

- [1] L. W. MO and Y. S. TSAI, *Radiative Corrections to Elastic and Inelastic ep and up Scattering* Rev. Mod. Phys. 41, 205. Published 1 January 1969.
- [2] McMahon David, *quantum field theory* McGraw Hill, 2008.
- [3] Geant4, <http://geant4.web.cern.ch/geant4/> (accessed June 30, 2013).
- [4] ROOT, <https://root.cern.ch/> (accessed April 15, 2015).
- [5] J. Leacock, *Measuring the Weak Charge of the Proton and the Hadronic Parity Violation of the $N \rightarrow \Delta$ Transition*. PhD thesis, Virginia Tech University, 2012.
- [6] D.S. Armstrong, A. Asaturyan, T. Averett, J. Benesch, J. Birchall7, P. Bosted9, A. Bruell9,... C. Zorn, *The Q_{weak} Experiment: A Search for New Physics at the TeV Scale via a Measurement of the Proton's Weak Charge*. Jefferson Lab, Published 10 December 2007.
- [7] Mark Dalton *Private Conversation with Mark Dalton* (July 13, 2013).
- [8] Steven Wells *Private Conversation with Dr. Steven Wells* (April 10, 2017).
- [9] *CERN Accelerating Science*, <https://home.cern/about/physics/standard-model> (accessed January 20, 2017).
- [10] H. A. Bethe and W. Heitler, *The Time Needed to Compute the Elastic Radiative Tails* Proc. Roy. Soc. (London), A146, 83 (1934).
- [11] H. A. Bethe and J. Ashkin, E. Segre, *Experimental Nuclear Physics*, Ed. (John Wiley Sons, Inc., New York, 1953), p. 265.A146, 83 (1934).
- [12] D.R. Yennie and H. Suura, *Phys. Rev.* 105, 1378 (1957)
- [13] D.R. Yennie, S. Frautschi, and H. Suura, *Ann. Phys. (N.Y.)* 13, 379 (1961).
- [14] N. T. Meister and D. R. Yennie, *Phys.* 130, 1210 (1963).
- [15] K. E. Erickson, *Nuovo Cimento* 19, 1029 (1961).
- [16] J.W. Lightbody, Jr. and J.S. O'Connell *Computers in Physics* 1997, 57-64.